Evolution of Clumpy Galaxies in the COSMOS Field

(COSMOS 領域におけるクランピー銀河の進化)

BY

Katsuhiro Murata

Department of Physics, Nagoya University,
e-mail: murata@cosmos.phys.sci.ehime-u.ac.jp

A Thesis presented for the degree of
Doctor of Science

Department of Physics
Nagoya University
Japan

December, 2013

Evolution of Clumpy Galaxies in the COSMOS Field[*1]

Katsuhiro Murata

Submitted for the degree of Doctor of Science
December 2013

Abstract

Using the *Hubble Space Telescope*/Advanced Camera for Surveys data in the COSMOS 2 deg^2 field, we systematically searched clumpy galaxies at $0.2 < z < 1.0$ and investigated the fraction of clumpy galaxies and its evolution as a function of stellar mass, star formation rate (SFR), and specific SFR (SSFR). The fraction of clumpy galaxies in star-forming galaxies with $M_{\rm star} > 10^{9.5} M_\odot$ decreases with time from ~ 0.3 at $0.8 < z < 1.0$ to ~ 0.05 at $0.2 < z < 0.4$ irrespective of the stellar mass. On the other

---

[*1] Based on observations with the NASA/ESA Hubble Space Telescope, obtained at the Space Telescope Science Institute, which is operated by AURA Inc, under NASA contract NAS 5-26555. Also based on observations made with the Spitzer Space Telescope, which is operated by the Jet Propulsion Laboratory, California Institute of Technology, under NASA contract 1407. Also based on data collected at; the Sub- aru Telescope, which is operated by the National Astronomical Observatory of Japan; the XMM-Newton, an ESA science mission with instruments and contributions directly funded by ESA Member States and NASA; the European Southern Observatory under Large Program 175.A-0839, Chile; Kitt Peak National Observatory, Cerro Tololo Inter-American Observatory and the National Optical Astronomy Observatory, which are operated by the Association of Universities for Research in Astronomy, Inc. (AURA) under co- operative agreement with the National Science Foundation; and the Canada-France-Hawaii Telescope with MegaPrime/MegaCam operated as a joint project by the CFHT Corporation, CEA/DAPNIA, the NRC and CADC of Canada, the CNRS of France, TERAPIX and the Univ. of Hawaii.

hand, the fraction of clumpy galaxies increases with increasing both SFR and SSFR in all the redshift ranges we investigated. In particular, we found that the SSFR dependences of the fractions are similar among galaxies with different stellar masses, and the fraction at a given SSFR does not depend on the stellar mass in each redshift bin. The evolution of the fraction of clumpy galaxies from $z \sim 0.9$ to $z \sim 0.3$ seems to be explained by such SSFR dependence of the fraction and the evolution of SSFRs of star-forming galaxies. The fraction at a given SSFR also appears to decrease with time, but this can be due to the effect of the morphological K-correction. We suggest that these results are understood by the gravitational fragmentation model for the formation of giant clumps in disk galaxies, where the gas mass fraction is a crucial parameter.

Contents

List of Figures

List of Tables

ACKNOWLEDGEMENT

I owe my gratitude to Prof. Taniguchi for a lot of helpful suggestions and stimulating discussions during my stay at Ehime university. I would like to thank my supervisor Prof. Takeuchi for his continous support and encouragement during my graduate course.

All the members of astrophysics group of Nagoya university and Research Center for Space and Cosmic Evolutionwere (RCSCE) of Ehime university have given me useful advices in a number of ways. Especiaaly, I would like to thank Prof. Sugiyama, Prof. Inutsuka, Prof. Nagao, Dr. Kajisawa, Dr. Shioya, Dr. Matsuoka and Dr. Malek, who give constructive comments. I would like to offer my special thanks to Dr. Kobayashi, who gives warm encouragement. Also, I would like to express a deep gratitude to Prof. Inoue, who was supporting me when I started to research galaxies at Nagoya unviersity.

The research presented in this thesis was carried out in collaboration with the COSMOS team. I would like to thank all the members of the COSMOS team. I am greateful to all the staff of the physics depertment of the Nagoya university and the GCOE members who skillfully maintain the high level of research environment in the institute. I acknowledge the financial support from the Research Fellowships of the Japan Society for the Promotion of Science for Young Scientists.

My friends in Nagoya university and in Ehime university gives me a lot of joy and support. Special thanks go to Ms. Fujiwara, Dr. Sakai and Dr. Sato.

I also appreciate many supports by my parents and my sister.

Chapter 1

OVERVIEW

1. Galaxies in the Universe

In 1924, Edwin, P. Hubble discovered that the Andromeda Nebula (M 31) is an independent galactic system far away form our Milky Way Galaxy. Soon after his discovery, we human being realized that there are numerous galaxies in our Universe.

Here, let us estimate how many galaxies in our Universe. First, we estimate the mass of our Universe as follows.

$$\begin{aligned} M_{\rm univ} &= 4\pi\, D_{\rm Hubble}^3\, \rho_{\rm crit}/3 \\ &= 8 \times 10^{55}\ {\rm g} \\ &= 4 \times 10^{22}\, M_\odot, \end{aligned} \tag{1.1}$$

$$\tag{1.2}$$

where $D_{\rm Hubble}$ is the Hubble diameter of our Universe, $\rho_{\rm crit}$ is the critical density of our Universe at present day, and $M_\odot$ is the solar mass, 2×10^{33} g. The critical density is

$$\rho = 3H_0^2/(8\pi G) = 9.47 \times 10^{-30}\ {\rm g\ cm^{-3}} \tag{1.3}$$

for $H_0 = 70$ km s^{-1} Mpc^{-1}. It is also noted that the Hubble radius is estimated as $R_{\rm Hubble} = T_{\rm Hubble}\, c \sim 4.1$ Gpc where $T_{\rm Hubble}$ is the Hubble time $1/H_0 \sim 133$ Gyr.

Since the matter density is only one third of the total energy in our universe (Fig. 1), the mass including both baryonic and dark matter is

$$M_{\rm univ,matter} \sim 10^{22}\, M_\odot, \tag{1.4}$$

Given the typical matter mass of a galaxy is $10^{11}\,M_{\odot}$, it is expected that there are $\sim 10^{11}$ galaxies in our Universe. Another estimate of the number of galaxies in our Universe is also made from observations. For example, the Hubble Ultra Deep Field (HUDF) found ~ 10000 galaxies in a sky area 11.96 arcmin^2. If we observe all the sky area (i.e., 4π steradian) at the depth of HUDF, an expected total number of galaxies is $\sim 10^{11}$ galaxies, that is nearly the same as the above theoretical estimate. In this way, we can realize that there are a huge number of galaxies is in our Universe. The age of our Universe is estimated as 13.8 billion years (e.g., Komatsu et al. 2011, Planck Collaboration 2013). Here a question arises as how such numerous galaxies were born and evolved during the cosmic time.

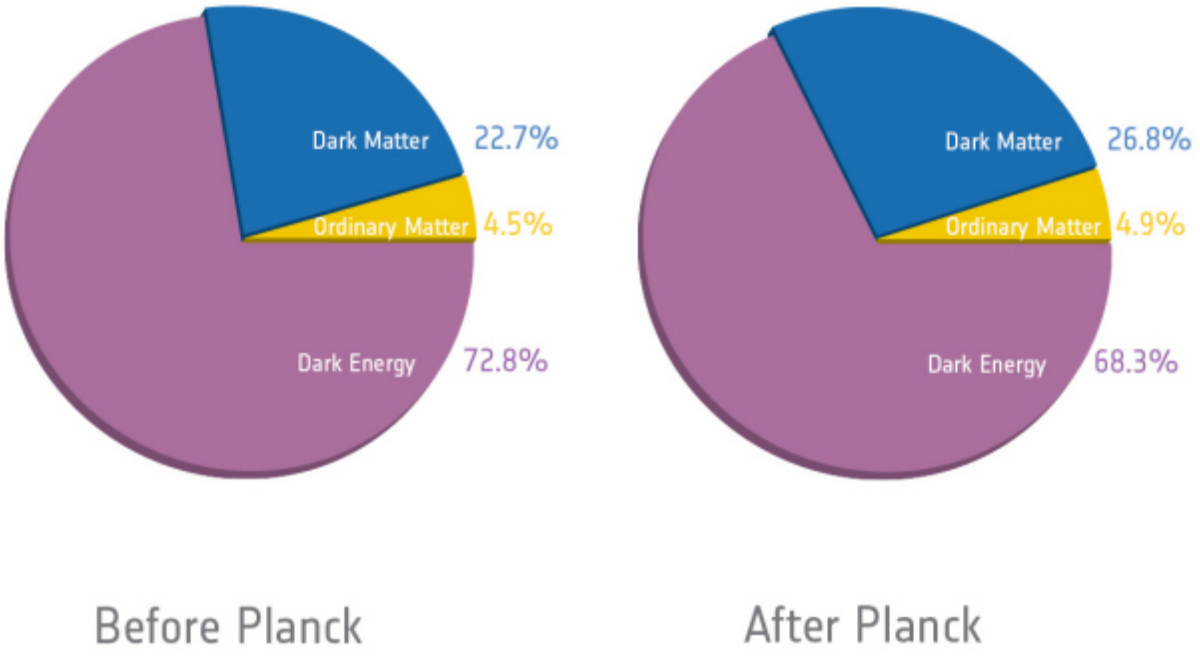

Fig. 1.— The cosmic recipe obtained by Planck. http://sci.esa.int/planck/51557-planck-new-cosmic-recipe/

2. The History of our Universe

Next, let us briefly summarize the history of our Universe (Fig. 2). Soon after the birth, our Universe experienced the so-called inflation and then the fireball created by the inflation caused the big bang. For first a few 100 million years, our Universe was too hot to form cold gas clouds in which stars are born. Namely, our Universe was overwhelmed by the complete darkness and thus the first a few million years is called as the dark age. After this dark age, first stars were born in high density regions that were led by the help of dark matter. It is noted that first dark matter halos have only several millions solar masses. Such small dark matter halos had been accumulated by their gravity and then evolved to a larger galaxy. Therefore, the growth of galaxies is considered to take a very long time from the birth of first stars to the present day (Fig. 2).

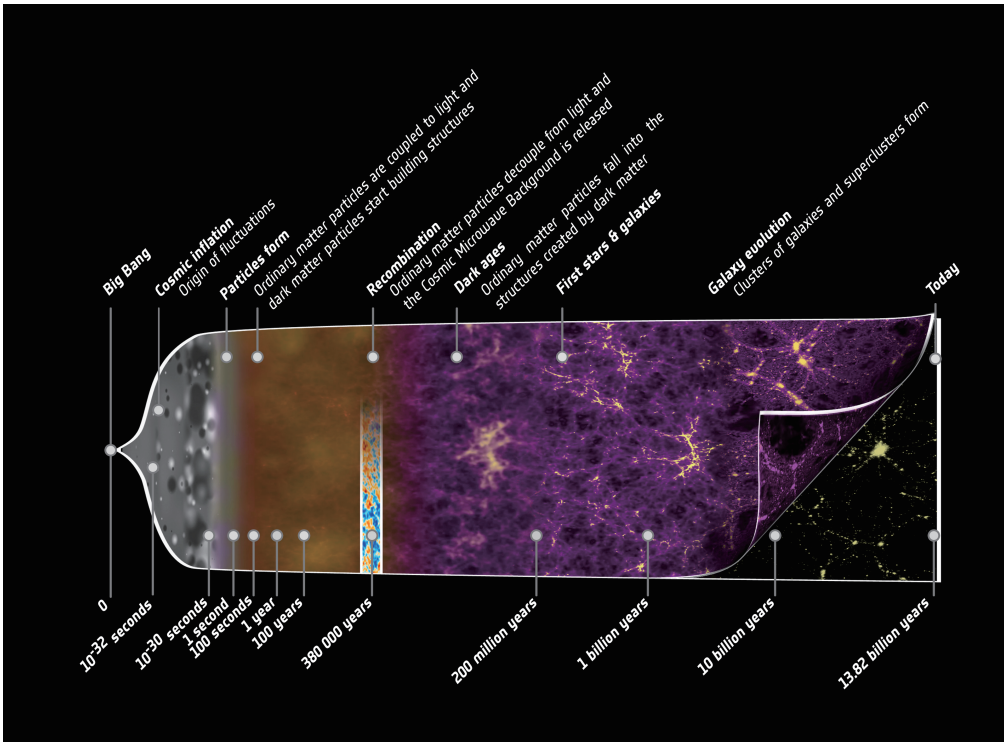

Fig. 2.— The history of the Universe. http://sci.esa.int/planck/51560-the-history-of-structure-formation-in-the-universe/

The evolution of galaxies basically means the transformation form gas to stars and their recycling processes during the course of evolution. The star formation history in galaxies also seems to be physically related to the mass assembly process in galaxies. Therefore, in order to understand the evolution of galaxies, it is crucially important to investigate rapidly evolving phases in galaxies.

In two decades, the cosmic star formation history has been investigated by several deep survey programs with use of both Hubble Space Telescope and ground-based 8-10 m class telescopes. These surveys have shown that the peak of the cosmic star formation rate is around redshift $z = 2$ (e.g., Madau et al. 1996; Bouwens et al. 2011); see Figure 3. Interestingly, the number density of quasars (luminous active galactic nuclei powered by gas accretion onto a super massive black hole) also peaks around $z = 2$ (Ueda et al. 2003). This suggests that the super massive black hole also rapidly evolves together with their host galaxies. Accordingly, a question arises as what happened around this redshift in the Universe (e.g., Kormendy & Ho 2013).

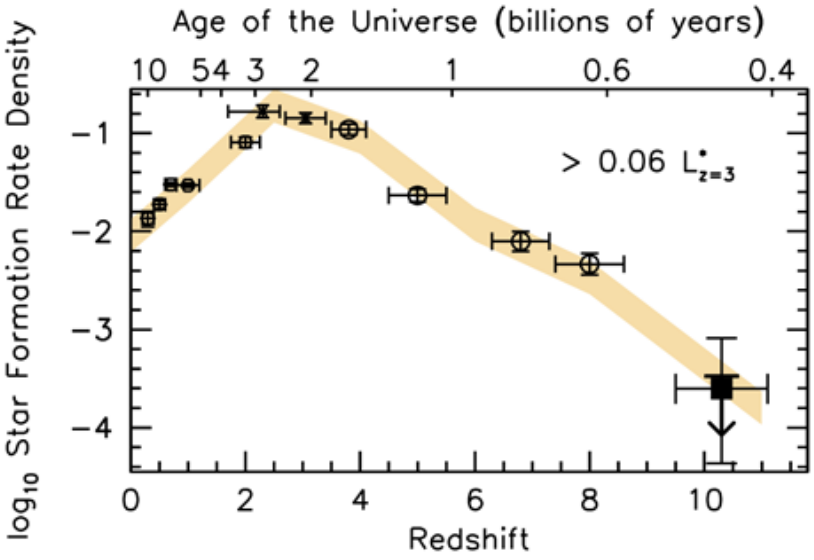

Fig. 3.— The cosmic star formation history as a function of redshift. http://www.firstgalaxies.org/the-latest-results

3. Galaxies in the Local Universe

Turning our attention to the present day, we observe regular-shaped massive galaxies such as elliptical and disk galaxies in the local Universe. The most well-known classification system for galaxy morphology is the Hubble classification system shown in Figure 4 (Hubble 1936). The Hubble classification of galaxy morphology consists of three

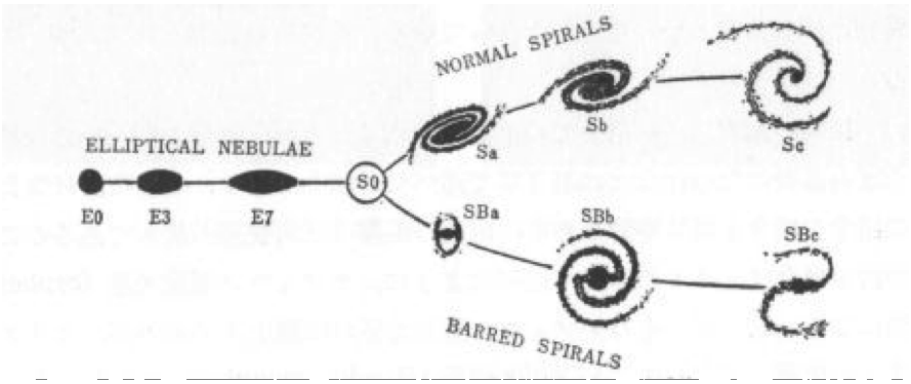

Fig. 4.— The Hubble classification of galaxies in the local universe.

sequences; 1) elliptical galaxies, 2) spiral galaxies, and 3) barred spiral galaxies. Their typical examples are shown in Figure 5, 6, and 7, respectively. Elliptical galaxies have no disk component while both spiral and barred spiral galaxies have a well-defined disk together with a bulge that shows the spheroidal shape centered at the nucleus. Therefore, both spiral and barred spiral galaxies are also called as disk galaxies (see Figure 8). Hubble (1936) introduced a hypothetical class of S0 galaxies between elliptical and disk galaxies. No S0 galaxy was found when Hubble proposed his classification scheme. However, later, many S0 galaxies have been found, in particular, in over density regions such as clusters of galaxies in nearby Universe. Typical examples are shown in Figure 9.

Here it is noted that galaxies are broadly classified into early- and late-type galaxies. Elliptical, S0, and Sa (SBa) galaxies are called as early-type galaxies while Sb (SBb) and Sc (SBc) are called as late-type galaxies. There is another convention for disk galaxies is early- and late-type disk galaxies. In this case, elliptical galaxies are excluded from the class of early-type disk galaxies (see Fig. 10). When Hubble proposed his classification scheme, he presumed that all galaxies were born in a spherical shape and then evolved to disk-like galaxies. This assumption led Hubble to use the above two types of conventions.

Elliptical galaxies are classified into eight subclasses from E0 to E7. The numerical

Fig. 5.— Images of elliptical galaxies. From top to bottom, M89 (E0), M32 (E2), and NGC3377 (E6). ©Palomar Observatorycourtesy of Caltech(M89), NOAO/AURA/NSF(M32), NASA(NGC3377)

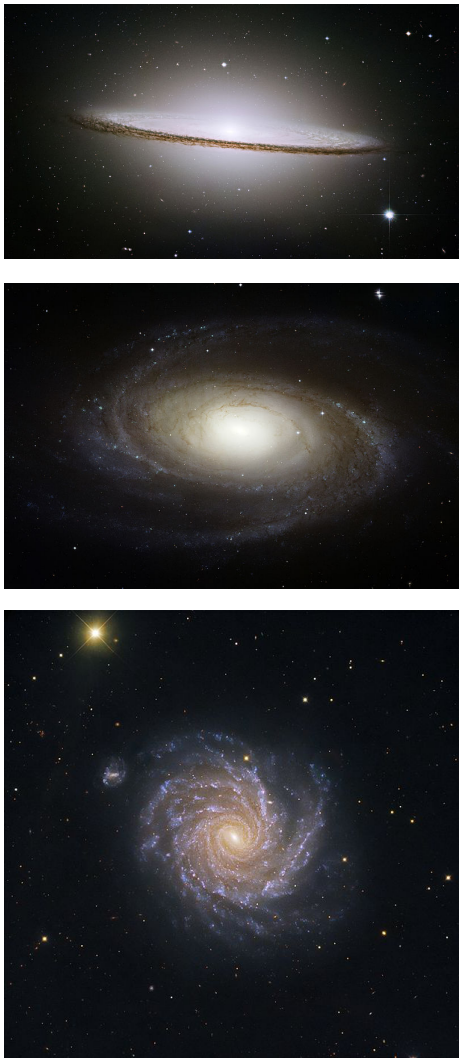

Fig. 6.— Images of spiral galaxies. From top to bottom, the images show Sombrero galaxy (Sa), M81 (Sb), and NGC1232 (Sc). ©NASA, STScI, and/or ESA(Sombrero galaxies), NASA, ESA and the Hubble Heritage Team STScI/AURA(M81), ESO/IDA/Danish 1.5 m/R.Gendler and A. Hornstrup (NGC1232).

code from 0 to 7 is the ellipticity of apparent shapes of elliptical galaxies. The ellipticity is defended as

$$e = (a - b)/a \tag{1.5}$$

where a and b are the major and minor axis, respectively.

Disk galaxies are also classified into three subclasses from a to c; Sa, Sb, and Sc for spiral galaxies and SBa, SBb, and SBc for barred spiral galaxies. Although not so many, there are galaxies that can be classified as a class between Sc and Irr. For these galaxies, other names are often used; e.g., Sd and Sm where "m" means Magellanic clouds type

Fig. 7.— Images of barred spiral galaxies. From top to bottom, the images show NGC4650 (SBa), NGC1300 (SBb), and NGC1073 (SBc). ©Faulkes Telescope South operated by Las Cumbres Observatory Global Telescope Network (NGC4650), HST/NASA/ESA (NGC1300), http://cseligman.com/text/atlas/ngc10a.htm (NGC1073)

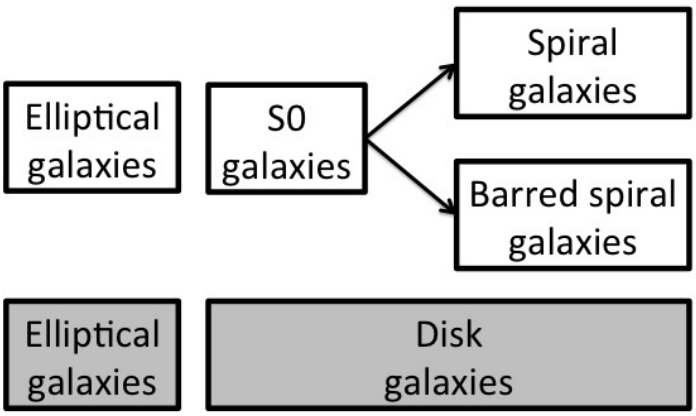

Fig. 8.— Schematic overview of classification of elliptical galaxies and disk galaxies.

morphology.

The Hubble sequence for disk galaxies is physically important because earlier-type disk galaxies tend have a larger bulge, more wound spiral arms, and lower star formation activity (Fig. 11). Therefore, it is important to investigate the origin of the Hubble classification of galaxies.

As shown in this classification system, most galaxies in the local Universe are classified into (1) ellipticals, (2) S0s, (3) spirals, and (4) barred spirals. In addition to these classes of galaxies, there are irregular galaxies that show no rotational asymmetry and have no galactic nucleus (Hubble 1926). However, the fraction of irregular galaxies is only 1% at most. Typical examples of irregular galaxies taken from Terao et al.(2013) are shown in Figure 12. It is also noted that interacting and merging galaxies also share 1% of galaxies in the local universe; see Figure 13. In the Local Universe, Fukugita et al. (2007) studied the g-band morphologies of galaxies using imaging data taken from Sloan Digital Sky Survey (SDSS: York et al. 2000). They showed that, for the galaxies with $r \leq 16$ mag in AB magnitude, the ratio of each Hubble class according to the g-band morphology is E : E/S0-S0 : S0a-Sab : Sb-Sc : Scd-Sdm : Im = 0.14 : 0.26 : 0.25 : 0.28 : 0.038 : 0.014.

Fig. 9.— Images of S0 galaxies (left:NGC4382, right:NGC3115). The right is edge-on S0 galaxy. ©Atlas Image [or Atlas Image mosaic] courtesy of 2MASS/UMass/IPAC-Caltech/NASA/NSF

One important goal is to understand the origin of galaxies observed today, including our own Galaxy. We thus have fundamental two questions. (1) When were they born ? (2) How did they evolve as a function of the cosmic time ?

Our nearby universe appears to be dominated regular-shaped galaxies such elliptical and disk galaxies. Therefore, the so-called Hubble sequence provides us a good guideline to investigate the formation and evolution of galaxies. Namely, one important goal is the understanding of the origin of Hubble sequence; when and how the Hubble sequence was established during the course of galaxy evolution from high redshift to the present day (e.g., Kajisawa & Yamada 2001; Conselice et al. 2005; Law et al. 2007).

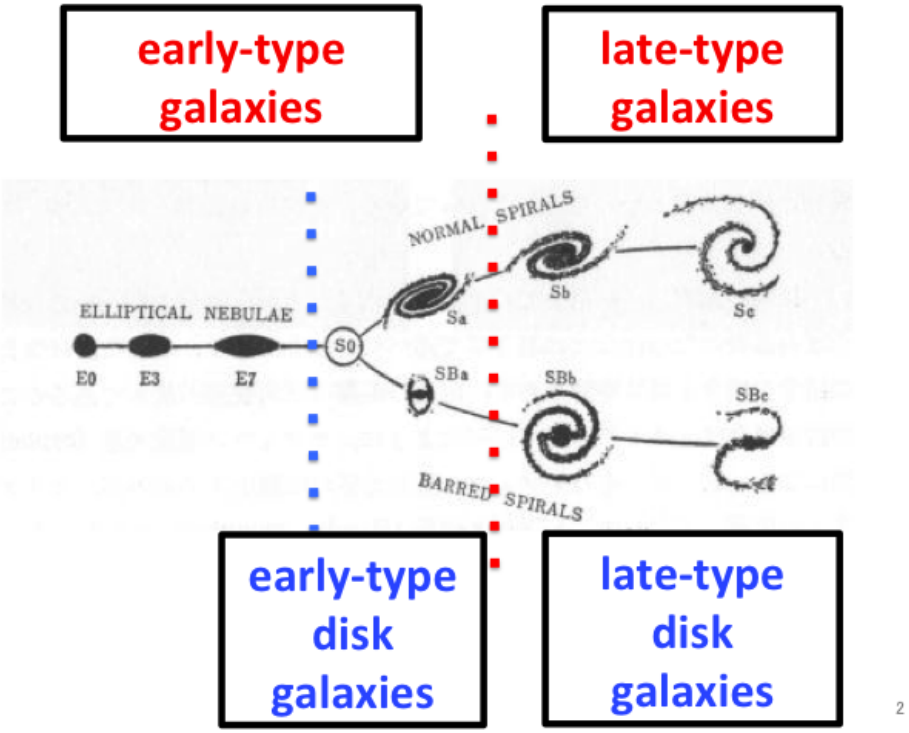

Fig. 10.— Schematic overview of classification of early type and late type galaxies.

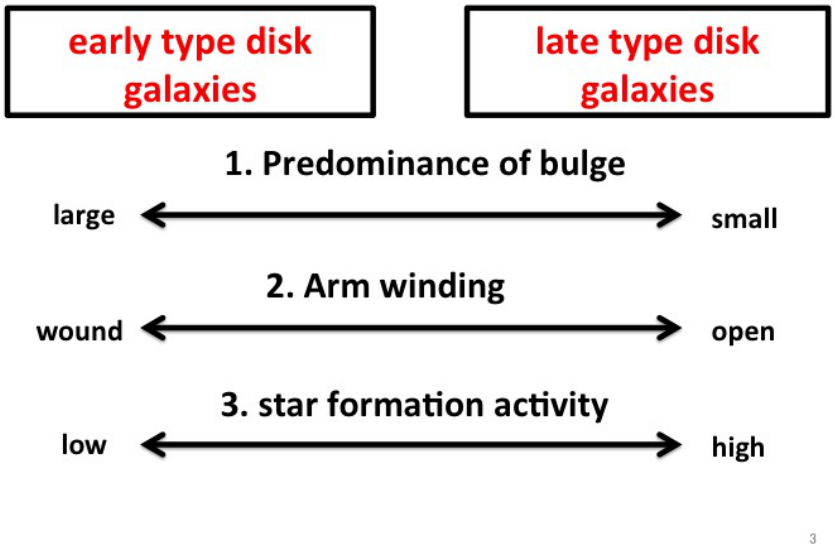

Fig. 11.— Schematic overview of relation between galaxy class and properties.

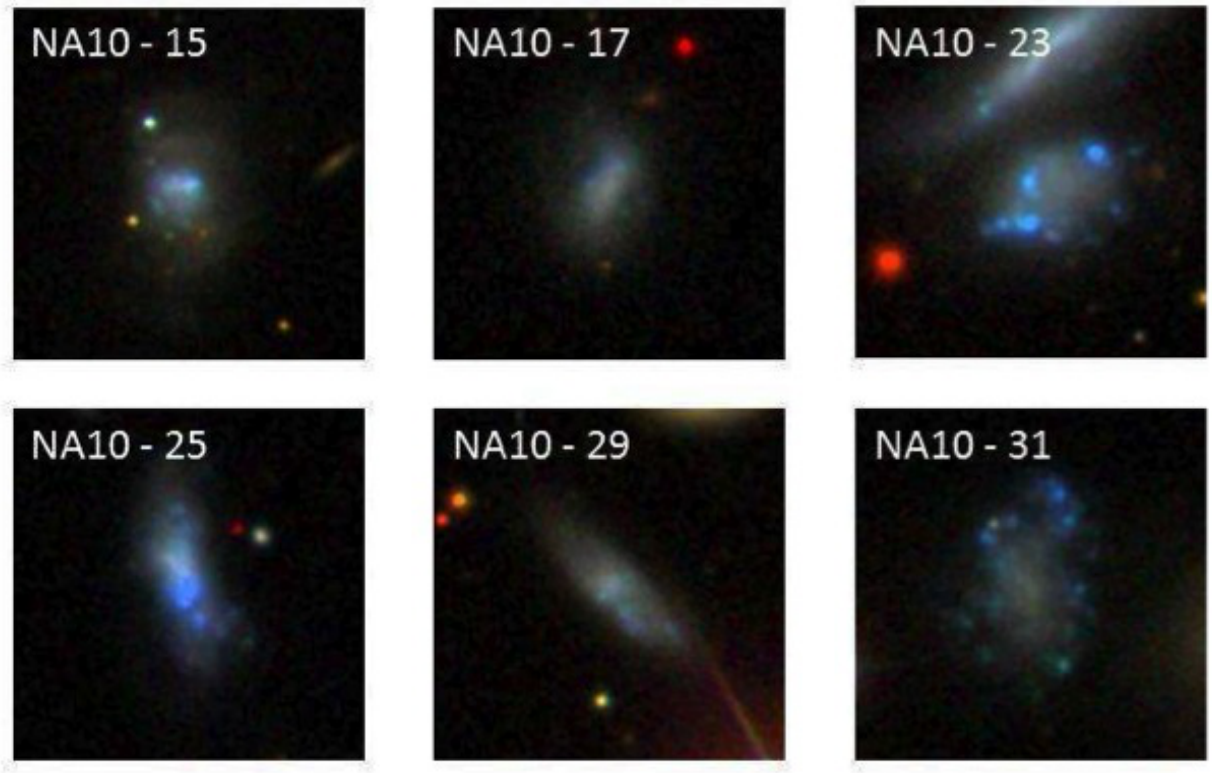

Fig. 12.— Images of genuine irregular galaxies in Terao et al. (2013).

4. Environment of galaxies

How are galaxies distributed in the Universe ? It had been believed that galaxies are distributed homogeneously in the Universe and thus there is no special direction (line of sight). This homogeneous and isotropic nature of the Universe is called as the cosmological principle. However, we human being already discerned in the 19th century that there are groups and clusters of galaxies in nearby Universe.

By the early 80s, the hierarchical structures in the Universe are classified into the categories given in Table 1.

However, it turned out that our Universe consists of filamentary structures traced by a number of galaxies and voids in which there are few galaxies. This great discovery was made by the CfA survey (de Lapparent et al. 1986; Geler & Huchra 1987; Huchra et al. 1990). Although the CfA survey investigated the distribution of galaxies in the Universe within 500 million light years, later large-scale sky surveys have confirmed the result of

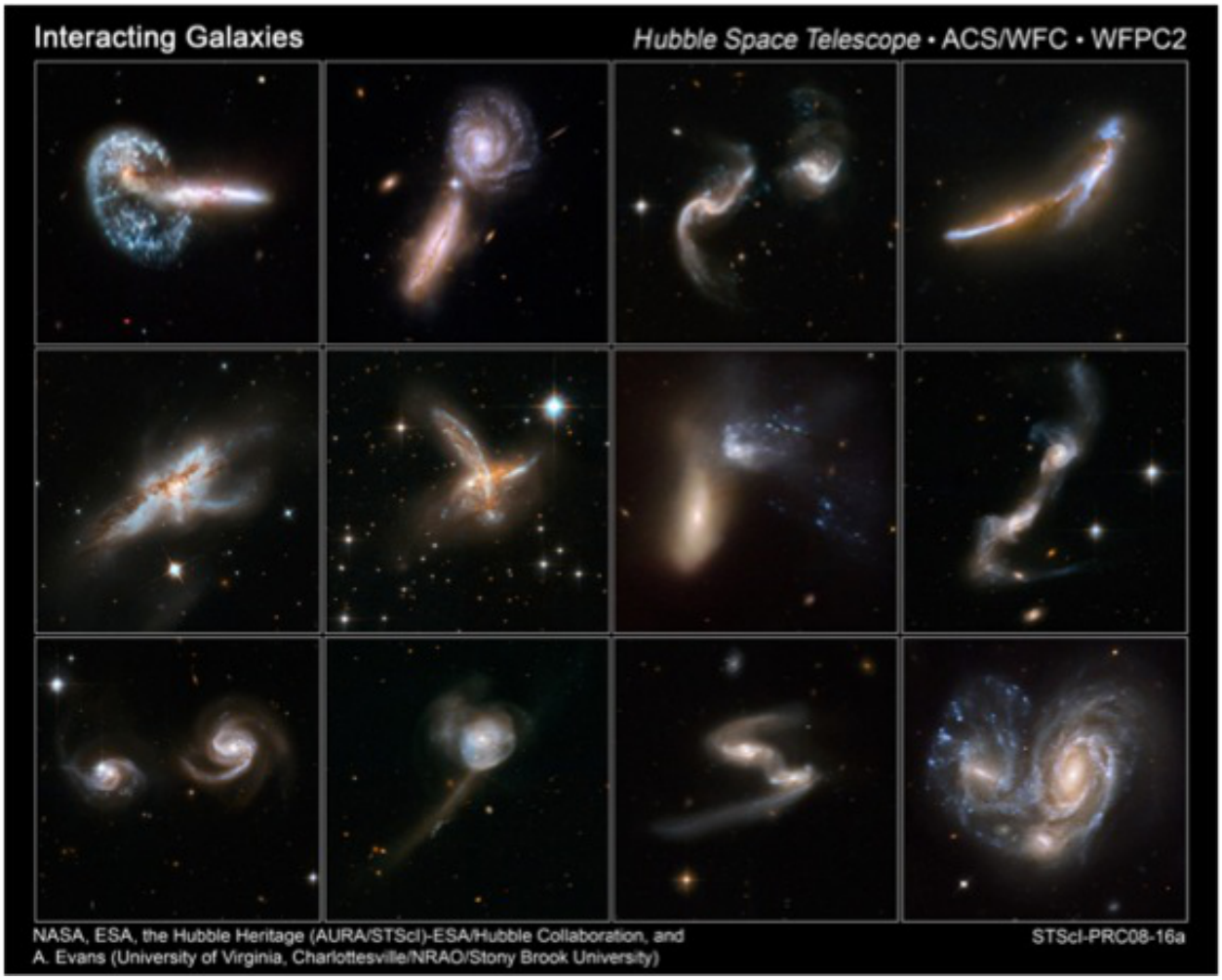

Fig. 13.— Images of interacting galaxies. ©A. Evans (University of Virginia, Charlottesville/NRAO/Stony Brook University), and the Hubble Heritage Team (STScI/AURA)-ESA/Hubble Collaboration.

Table 1: The category of hierarchical structures in the Universe.

Category	N_{galaxy}
isolated galaxies	1
binary galaxies	2
groups of galaxies	3 - several 10s
clusters of galaxies	several 10s - 1000

CfA surveys up to 2 billion light years; 2dF GRS (Colless et al. 2001), Las Campanas Redshift Survey (Shectman et al.1996), and Sloan Digital Sky Survey (SDSS; Blanton et al. 2003). The large scale structure stuided by SDSS is shown in Figure 14

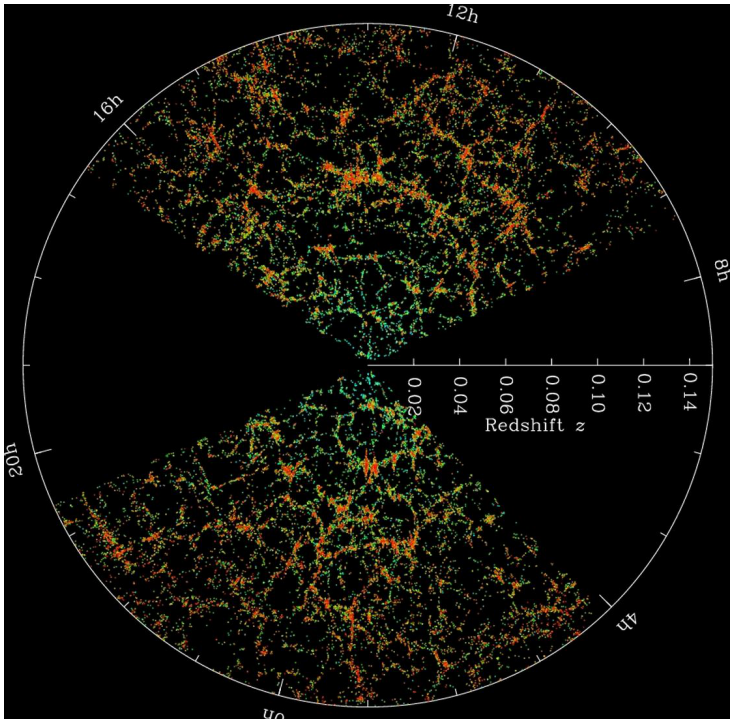

Fig. 14.— Large scale structures in the Universe studied by the Sloan Digital Sky Survey (SDSS) ©Blannton et al. (2003).

In this way, nowadays, clusters of galaxies are considered to be located in regions in which several filaments come together and groups of galaxies lie in filamentary structures. In lower density regions, there present isolated and binary galaxies. The mass and scale of important ingredients in the Universe are summarized in Table 2.

Table 2: The mass and scale of important ingredients in the Universe.

	mass ($M_\odot$)	size (kpc)
galaxies	$10^9 - 10^{12}$	1- 10
clusters of galaxies	$10^{13} - 10^{15}$	$1000 - 10^4$
voids	-	$10^4 - 10^5$

Environments of galaxies are different from galaxy to galaxy. Does the nature of galaxies depend on their environments ? It is now widely accepted that it strongly

depends on the environments. In Figure 15, we show the fraction of galaxy populations as a function of the surface number density of galaxies (Dressler 1980). It is clearly shown that the fractions of E and S0 galaxies increase with increasing surface density while that of spiral galaxies decreases significantly. This is the so-called morphology-density relation for galaxies.

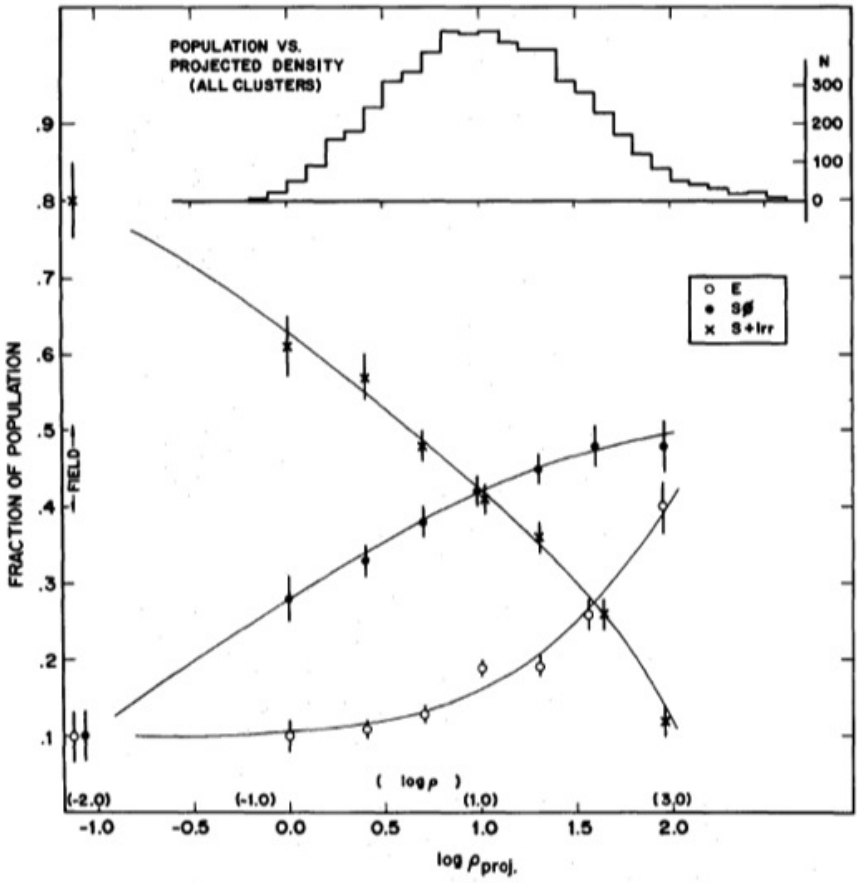

Fig. 15.— The Morphology-density relation of galaxies (Dressler 1980). The fraction of elliptical (open circle), S0 (filled circle), and spiral and irregular (cross) galaxies are shown as a function of logarithmic projected number density of galaxies $\rho_{\rm proj}$ [Mpc^{-2}]. The upper histogram is number of all galaxies. Sample consists of over 6000 galaxies in 55 rich galaxy clusters. The fraction of spiral and irregular galaxies decrease as projected number density increase, which compensate the increase of the fraction of elliptical and S0 galaxies.

The large scale structures found in nearby Universe are found in high redshift Universe up to $z = 1$ (Scoville et al. 2007) and proto clusters of galaxies are found up to $z \sim 6$ (Ouchi et al. 2005). Therefore, any galaxies have been evolving together with their environments intimately. In this context, we have to investigate the evolution of galaxies

in the evolving large scale structures in the Universe (see Fig. 16 and 17).

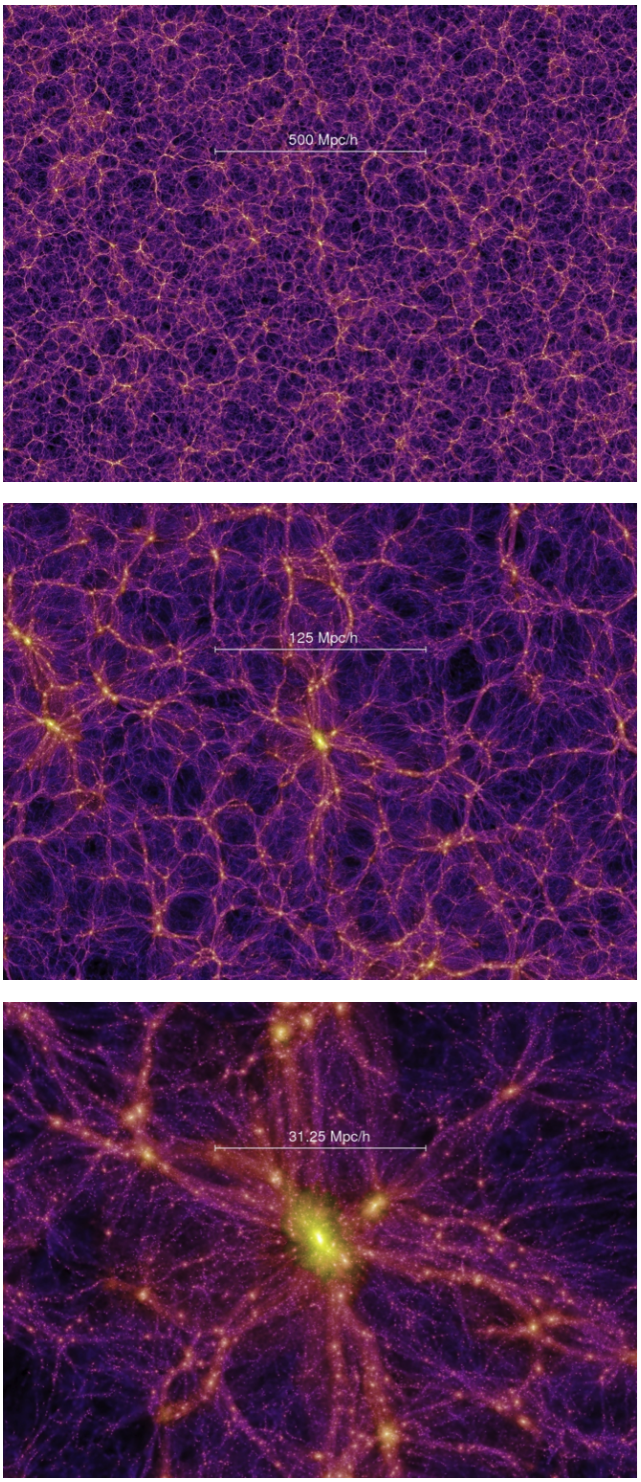

Fig. 16.— The formation and evolution of large scale structures. ©The VIRGO Millennium simulations

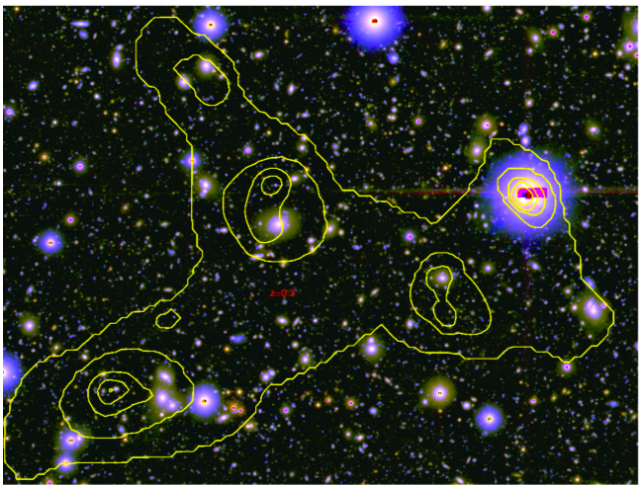

Fig. 17.— The observed large scale structure at $z \sim 0.3$ in the COSMOS field. This corresponds to the Virgo Millennium Simulation shown in the bottom panel of Figure 16. ©the HST COSMOS Project

5. Galaxies in Distant Universe

In the Universe at higher redshifts, the classification has been also studied with recent deep surveys. It has been reported that the classification becomes gradually meaningless toward higher redshifts. Delgado-Serrano et al. (2009) compared the variation of the morphology of galaxies between the the Local Universe and the universe at $z \sim 0.65$ using the SDSS and GOODS surveys. They found that the 10% of the galaxies with $J < -20.3$ mag in the AB system in the Local Universe are peculiar, while about a half are peculiar at $z \sim 0.65$ (Fig. 18). According to the review by Abraham & van den Bergh (2001), the description of the Hubble class applies in full detail at $z < 0.3$, the bar spirals are rare at $z \sim 0.5$, and peculiar galaxies rapidly increase at $z > 0.6$.

In short, the Hubble classification is rapidly formed since when the age of the current was nearly a half of the cosmic age toward the present. Although the formation of the Hubble classification is one of the hot topics in astronomy, the formation has not been understood yet. The key to the solution may be the physical properties along the Hubble class. In the Local Universe, it is strongly confirmed that galaxies of later type (the side of the peculiar or irregular galaxies in Hubble class; see Figure 18) are bluer than earlier

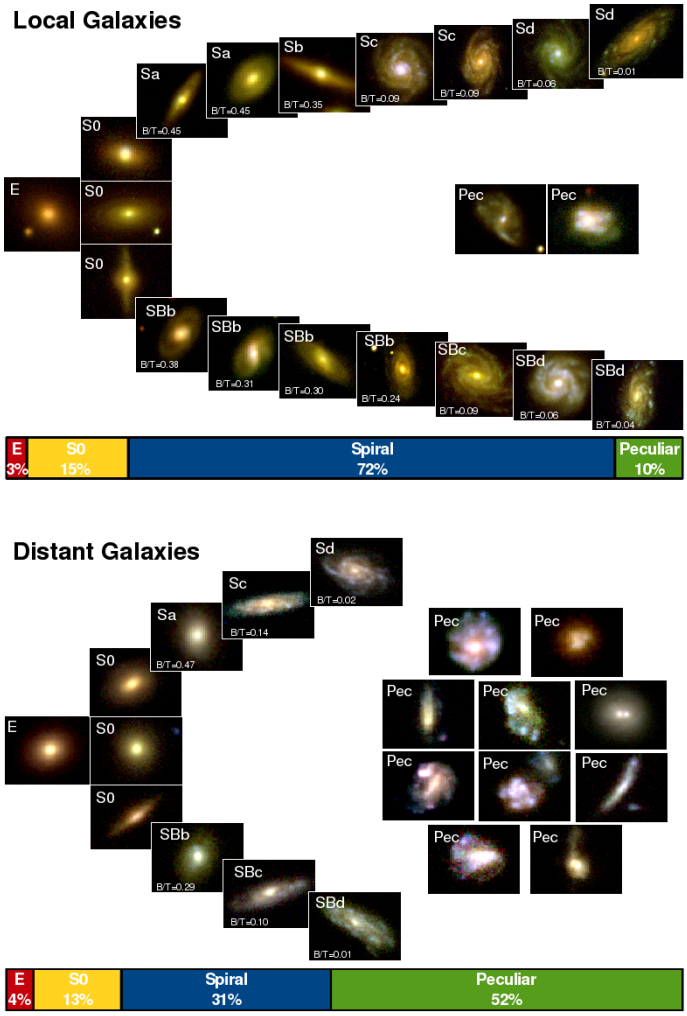

Fig. 18.— Hubble sequence in the Local Universe (upper panel) and the distant Universe (lower panel) from Delgado-Serrano et al. 2009.

type galaxies. The later type galaxies also have less stellar mass, more cold gas, more active star formation. However, in the distant Universe, the above relation between the Hubble type and the physical quantities does not apply. Ilbert et al. (2009) presented that the elliptical galaxies, most of which form few stars and have red colors in the Local Universe, experience star formations and have blue colors in distant Universe ($z \sim 1$). In addition, Bundy et al. (2006) showed that, the fraction of blue galaxies for large stellar mass increases toward the distant Universe ($z \sim 1.4$).

On the other hand, many star-forming galaxies at $z > 1$ show irregular and clumpy morphologies dominated by several giant star-forming clumps in the rest-frame UV and

optical wavelengths (e.g., Elmegreen et al. 2007; Forster-Schreiber et al. 2009), which is quite different from those of normal spiral galaxies in the present universe. Spatially resolved spectroscopic studies of relatively bright such clumpy galaxies at $z \sim 2$ found that many of these galaxies show a large-scale velocity gradient, which suggests that these are rotating disks (e.g., Genzel et al. 2008; Forster-Schreiber et al. 2009). Radio observations of CO emission lines suggest that the gas mass fractions of these high-z star-forming galaxies are large ($\sim$ 30–80%; e.g., Daddi et al. 2010; Tacconi et al. 2010). The formation of giant star-forming clumps is naturally expected for these galaxies, because gas-rich disks are unstable for the gravitational fragmentation (e.g., Immeli, et al. 2004). Such high gas mass fractions are explained as the result of the rapid and smooth cosmic infall of gas ("cold stream"; Dekel et al. 2009). Theoretical studies suggest that giant clumps migrate into the center to form a bulge component and the gas disk becomes stable as the gas fraction decreases, and then clumpy galaxies evolve into normal spiral galaxies (e.g., Dekel et al. 2009; Ceverino et al. 2010).

6. Star formation history of galaxies

Another important quantity related to the galaxy evolution is the cosmic star formation history. The cosmic star formation history is shown in Figure 19 and 20.

Approximately a half of stellar mass was rapidly formed in first 5 Gyrs ($z \gtrsim 1$) and then the rest formed up to now, though the difference among authors increase toward higher redshift. In the sight of star formation rate, the cosmic star formation rate decreases at $z \sim 1$. This may be linked to the formation of the Hubble classifications. In this context, the relation between stellar mass and star formation activity of each galaxy is important. Several studies have been made on stellar mass of galaxies, star formation rate and the relation between them. It has been recognized that, on average, star formation activities of galaxies have declined toward the present and the galaxies with lower stellar mass have more active star formation. However, it is controversial that how rapidly the activity declines star formation activity as a function of stellar mass of galaxies. Damen et al. (2009a) studied the evolution of the SSFR for $\sim$ 3400 galaxies with $M_{\rm star} \gtrsim 10^{10}{\rm M}_{\odot}$ in

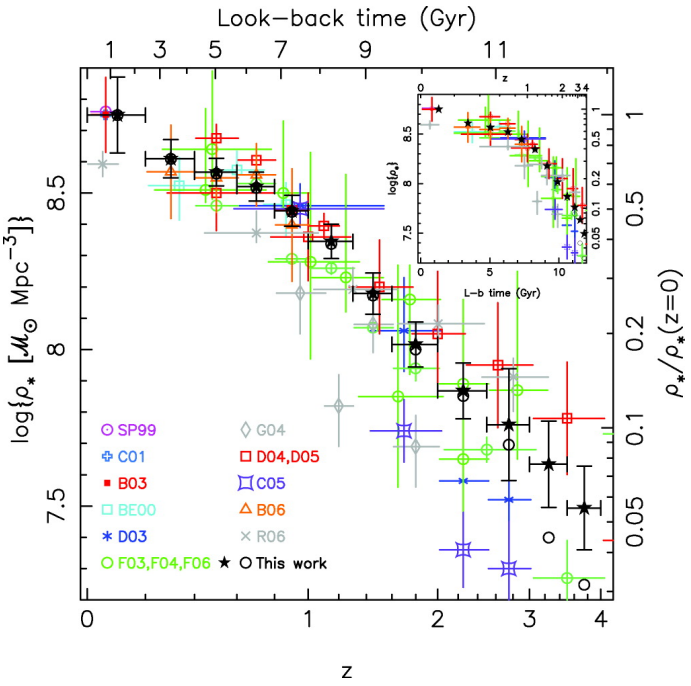

Fig. 19.— The evolution of stellar mass density in galaxies as a function of redshift from $z = 4$ to the present day ($z = 0$) (Perez-Gonzalez et al. 2008).

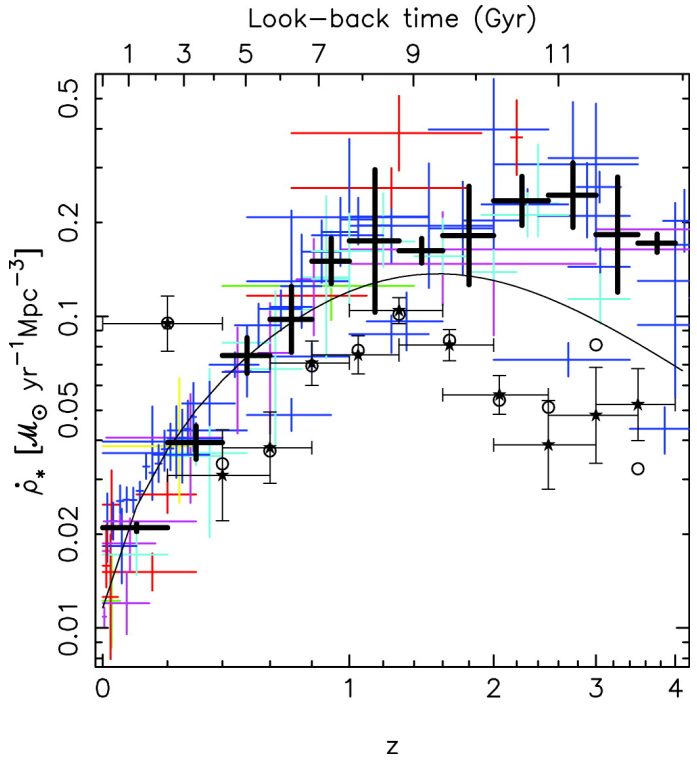

Fig. 20.— The evolution of cosmic star formation rate density in the Universe as a function of redshift from $z = 4$ to the present day ($z = 0$) (Perez-Gonzalez et al. 2008).

Extended CDFS. They reported that the evolution of the SSFR does not strongly depend on stellar mass and the SSFRs evolve as $\propto (1+z)^{5\pm0.4}$ from $z \sim 1.8$ to the present. They found that $19 \pm 9\%$ of the galaxies with $M_{\rm star} \gtrsim 10^{11}{\rm M}_{\odot}$ at $z \sim 1.8$ is quiescent galaxy, which is defined as those with the SSFR $< 1/t_{\rm Hubble}(z)$, while 65% is quiescent at $z \sim 0.5$. In contrast, Panter et al. (2008) reported that the evolution of the SSFR (or SFR) depend on stellar mass. Damen et al. (2009b) derived the SSFR for ~ 5300 galaxies selected with $K_{\rm s}$ band in CDFS, finding the SSFRs decrease from $z \sim 3$ to $z \sim 0$. Comparing their SSFRs with semi-analytic model (SAM; Guo & White 2008) based on the Millennium Simulation, they concluded the observed SSFRs decline more rapidly than the SAM result. Feulner et al. (2005) presented the variation of SSFR from $z \sim 0$ up to $z \sim 5$ for ~ 9000 galaxies selected with I-band in the FORS Deep Field and the CDFS. They found that, for galaxies with $M_{\rm star} \gtrsim 10^{8.5} M_{\odot}$, lower stellar mass galaxies have higher SSFRs and their SSFRs decrease toward the present. As discussed in the above paper, highly dust-obscured galaxies are missed in their SSFR estimation because their SFRs derived from the dust-corrected luminosity at FUV. Buat et al. (2008) found a shallow decrease in SSFR as increasing their stellar mass of UV selected galaxies and IR selected galaxies at $z \sim 0$ and $z \sim 0.7$ in CDFS.

7. This thesis

As stated in the previous sections, high-redshift galaxies have more irregular morphologies with higher star formation activities than local galaxies. Such high-redshift irregular galaxies are typically characterized by giant clumps which are not seen in local galaxies. Therefore they are thought to be ancestors of local galaxies. It is important to study high-redshift irregular galaxies for understanding of galaxy evolution.

The main goal of this thesis is to study the evolution of the fraction of clumpy galaxies at $0.2 < z < 1.0$. Also, we study the origin of tadpole galaxies and chain galaxies at high redshift universe.

In Chapter 2, we have studied the evolution of the fraction of clumpy galaxies in the COSMOS Field which is main study of this thesis. Also, we have studied tadpole galaxies

with a bright knot at one end together with a long tail structure in stellar continuum emission (Chapter 3), and chain galaxies with linearly-distributed more than two clumps (Chapter 4). In Chapter 5, we summarize the conlusions.

Throughout this thesis, magnitudes are given in the AB system. We adopt a flat universe with $\Omega_{\rm matter} = 0.3$, $\Omega_\Lambda = 0.7$, and $H_0 = 70$ km s^{-1} Mpc^{-1}.

Chapter 2

EVOLUTION OF CLUMPY GALAXIES IN THE COSMOS FIELD

1. Introduction

In the present universe, most bright galaxies have regular and symmetric morphologies, which can be classified in the framework of the Hubble sequence (Hubble, 1936). On the other hand, using the high-resolution imaging capability of the *Hubble Space Telescope* (*HST*), it has been found that many star-forming galaxies at $z > 1$ have irregular shapes with asymmetric structures, (e.g., Cowie et al., 1995; Steidel et al., 1996; Kajisawa & Yamada, 2001; Elmegreen et al., 2007; Cameron et al., 2011). Although these high-redshift irregular galaxies show a variety of morphologies, they commonly have giant (kpc scale) star-forming clumps (e.g. Förster Schreiber et al., 2011). Recent NIR integral field spectroscopy observations of star-forming clumpy galaxies at $z \sim 2$ revealed that a significant fraction of these galaxies show coherent rotation with a relatively large turbulent velocity in their ionized gas kinematics (e.g., Förster Schreiber et al., 2006; Wright et al., 2007; Genzel et al., 2008; Cresci et al., 2009; Förster Schreiber et al., 2009). Several studies of the radio CO line observations also found that actively star-forming galaxies at $1 \lesssim z \lesssim 3$ have large gas mass fractions of ~ 0.3 – 0.8 (Daddi et al., 2010; Tacconi et al., 2010; Tacconi et al., 2013). While some of these galaxies are galaxy mergers (e.g., Somerville et al., 2001; Lotz et al., 2004), these results can be explained

by theoretical models where gas-rich rotational disks are gravitationally unstable for the fragmentation and lead to the formation of giant star-forming clumps (e.g., Noguchi, 1998; Immeli et al., 2004; Bournaud et al., 2007; Dekel et al., 2009a). The high gas mass fraction of these galaxies is considered to be maintained by the rapid and smooth cosmic infall of gas along large-scale filaments. Since the accretion rate of gas is expected to decrease with time, especially at $z \lesssim 1$, the gas fraction of these clumpy galaxies declines at lower redshifts as the gas consumption by the star formation proceeds, which results in the stabilization of the gas disks (Cacciato et al., 2012). In this view, these high-redshift clumpy galaxies are considered to be progenitors of normal (disk) galaxies at low redshifts. Therefore, it is important to study the evolution of these clumpy galaxies in order to understand the formation process of normal galaxies in the present universe.

However, the number of systematic surveys for clumpy galaxies is very limited, because wide-field imaging data with high spatial resolution are required. While Elmegreen et al. (2007) claimed that clumpy galaxies are dominated at high redshift based on the morphological analysis of galaxies in the HUDF field, Tadaki et al. (2013) reported that ∼40% of 100 Hα emitters at $z \sim 2.2$ and $z \sim 2.5$ in the UKIDSS/UDS-CANDELS field show clumpy morphologies. Wuyts et al. (2012) measured the fraction of clumpy galaxies in star-forming galaxies with $M_{\rm star} > 10^{10} M_{\odot}$ at $z \sim 2$ in the GOODS-South field, and found that the fraction is 74% for clumps selected at the rest-frame 2800 Å and 42% for those selected at the rest-frame V band, which suggests that the morphological changing with different wavelength (the so-called morphological K-correction) can be important for the selection of clumpy galaxies. Although systematic surveys of clumpy galaxies at lower redshifts are also important for understanding the connection between clumpy galaxies at high redshifts and normal galaxies in the nearby universe, there is few survey for clumpy galaxies at $z \lesssim 1$. In this paper, we systematically search clumpy galaxies at $0.2 < z < 1.0$ in the COSMOS 2 deg^2 field (Scoville et al., 2007) and investigate their physical properties. The high spatial resolution images taken with *HST*/Advanced Camera for Surveys (ACS) over the very wide field allow us to construct a large sample of clumpy galaxies at $z < 1$ and to investigate the fraction of clumpy galaxies and its evolution as a function of physical properties such as stellar mass and star formation rate for the first time.

Section 2. describes our sample and details of the selection method for clumpy galaxies. We present the physical properties of clumpy galaxies and investigate the fraction of these galaxies and its evolution in Section 3.. Finally, we discuss our results in Section 4..

2. Sample and Analysis

Since our goal is to reveal how clumpy galaxies are related to their star formation activity, we need to make a sample of clumpy galaxies. In this chapter, we explain our methods of the source detection and the clumpy galaxy selection together with sample information.

2.1. Sample

In this study, we used a sample of galaxies with photometric redshifts of $0.2 < z < 1.0$ from the COSMOS photometric redshift catalog [*1] (Ilbert et al., 2009).

We basically analyzed galaxies with $I_{\rm F814W} < 22.5$ in order to securely select clumpy galaxies in the *HST*/ACS $I_{\rm F814W}$-band images (see the next section). The photometric redshift is estimated with more than 30 bands data from UV to MIR wavelength in the COSMOS field, and its uncertainty is very small ($\Delta z \lesssim 0.02$) for galaxies with $I_{\rm F814W} < 22.5$ at $z < 1$ (Ilbert et al., 2009), which is sufficiently accurate for our purpose.

In order to investigate the fraction of clumpy galaxies as a function of the physical properties of galaxies, we used the stellar mass ($\rm M_{star}$) and the star formation rate (SFR) of our sample galaxies estimated from the spectral energy distribution (SED) fitting technique (Ilbert et al., 2010; Ilbert et al., 2013). The multi-band photometric data from UV to MIR wavelength were fitted with the population synthesis model by Bruzual & Charlot (2003). The exponentially declining star formation histories and the Calzetti et al. (2000) extinction law were assumed, and the Chabrier (2003) IMF was adopted (see Ilbert et al., 2013 for details). The best-fit model was used to convert the luminosities to the stellar mass and the SFR. We excluded X-ray sources detected in the *Chandra* or

[*1] In Appendix A, we describe the COSMOS photometric redshift catalog.

XMM-Newton images (Hasinger et al., 2007; Elvis et al., 2009) and galactic stars classified in the SED fitting from our sample.

2.2. Selection for Clumpy Galaxies

Using the *HST*/ACS $I_{\rm F814W}$-band data of the COSMOS survey (Koekemoer et al., 2007), we examined the morphology of our sample galaxies and selected clumpy galaxies quantitatively. The clumpy galaxy is characterized by several relatively bright components (clumps) in a galaxy. We here consider galaxies with more than two such clumps ($N_{\rm clump} \geq 3$) as clumpy galaxies. In order to select clumpy galaxies, we first detected galaxies on the $I_{\rm F814W}$-band data, using the SExtractor software (Bertin & Arnouts, 1996). A detection threshold of 2.0 times the local background root mean square over 15 connected pixels was used. We adopted the *DEBREND_NTHRESH* parameter (number of deblending subthresholds) of 64 and the *DEBLEND_MINCONT* (minimum contrast parameter for deblending) parameter of 0.1 in the first SExtractor run (galaxy mode). We then searched counterparts of our sample galaxies mentioned above on the $I_{\rm F814W}$-band image, and found the counterparts for 24027 galaxies out of 24176 galaxies with $I_{\rm F814W} < 22.5$ at $0.2 < z < 1.0$. Next, we changed the *DEBLEND_MINCONT* parameter to 0.001 and rerun the SExtractor to more aggressively deblend each galaxy and detect relatively bright clumps in the galaxy (clump mode). The SExtractor parameters of galaxy mode and clump mode are listed in Table 1. The resulting catalog in this second SExtractor run was cross-matched with that in the first run. We then selected sample galaxies which are deblended into more than two components as clumpy galaxy candidates. In order to ensure that at least three clumps are comparatively bright, we set further criteria for clumpy galaxies as

$$f_1/f_2 \geq 0.3, \tag{2.1}$$

and

$$f_2/f_3 \geq 0.3, \tag{2.2}$$

where f_1, f_2, and f_3 are $I_{\rm F814W}$-band fluxes of the brightest, the second brightest, and the third brightest clumps, respectively, in the galaxy. In Figure 1, we show examples of

galaxies with more than two clumps as a function of these flux ratios among the brightest three clumps to demonstrate our classification. One can see that our selection enable to pick up sources with several significant clumps. On the other hand, galaxies with one dominant component, which corresponds to a bulge in some cases, lie at the right side in the figure, while those with only two bright components are located at the bottom right. In this paper, we refer to all galaxies which are not satisfied by the criteria for clumpy galaxies as "non-clumpy" galaxies.

Figures 2 and 3 show examples of clumpy and non-clumpy galaxies with $M_{\rm star} > 10^{9.5} M_{\odot}$ in each redshift bin, respectively. We selected total 2803 clumpy galaxies at $0.2 < z < 1.0$ with $I_{\rm F814W} < 22.5$. Our sample sizes are summarized in Table 2.

Table 1: The SExtractor parameters for source detections galaxy mode and clump mode

Parameter	Galaxy mode	Clump mode	Comment
DETECT_TYPE	CCD	CCD	Detect type
DETECT_MINAREA	15	15	Minimum number of pixels above threshold
DETECT_THRESH	2.0	2.0	Detection threshold in sigma
FILTER	N	N	Apply filter for detection
DEBLEND_NTHRESH	64	64	Number of deblending subthresholds
DEBLEND_MINCONT	0.1	0.001	Minimum contrast parameter for deblending

Table 2: Number of galaxies in our sample

Redshift	All ($M_{\rm star} > 10^{9.5} M_{\odot}$)	Clumpy ($M_{\rm star} > 10^{9.5} M_{\odot}$)
$0.2 \leq z \leq 0.4$	7392 (3826)	363 (106)
$0.4 \leq z \leq 0.6$	5742 (4221)	464 (304)
$0.6 \leq z \leq 0.8$	6297 (5597)	895 (781)
$0.8 \leq z \leq 1.0$	4596 (4500)	1081 (1055)
total	24027 (18144)	2803 (2246)

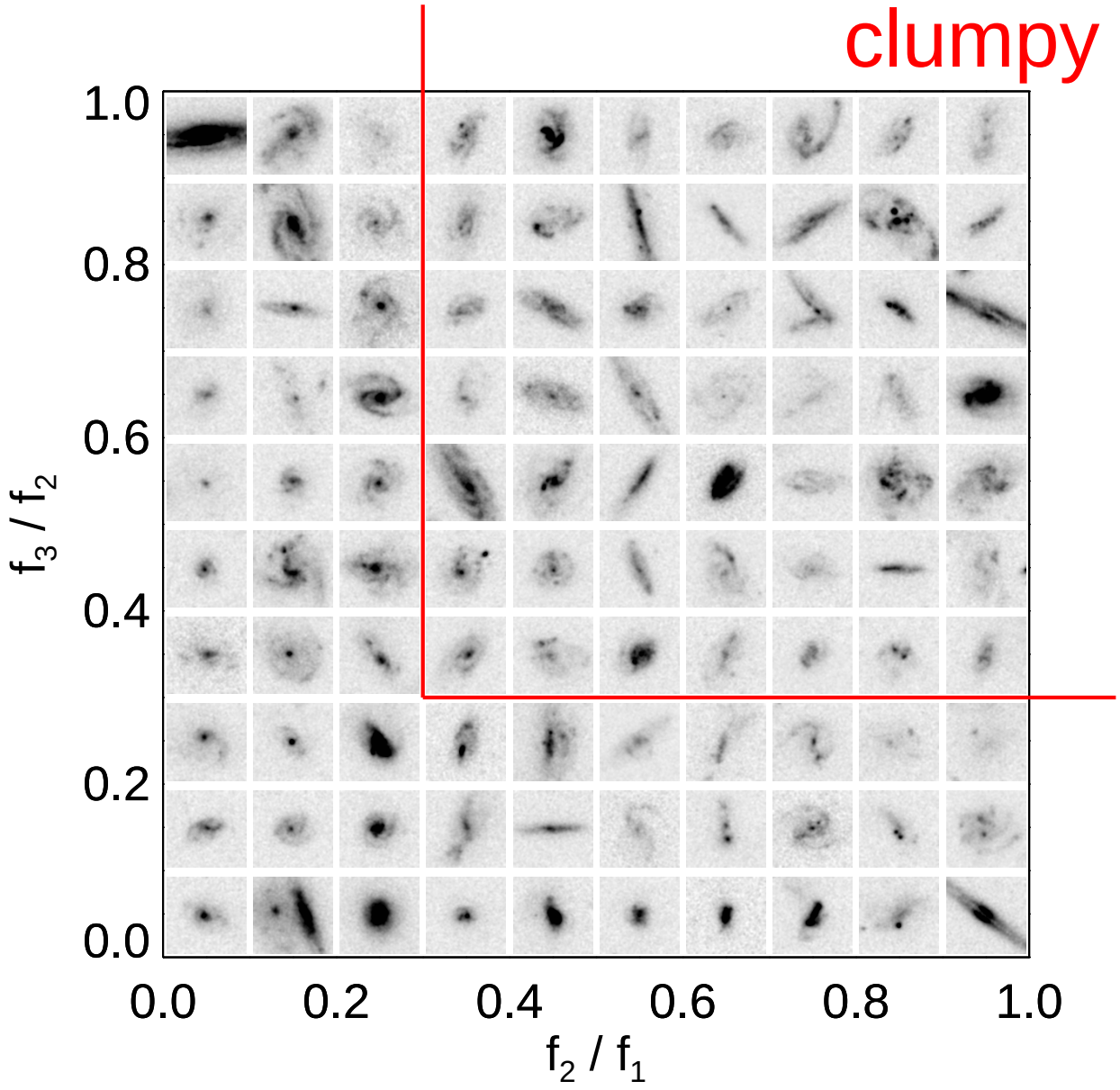

Fig. 1.— *HST*/ACS $I_{\rm F814W}$-band images of galaxies with more than two components as a function of the flux ratios among the brightest three clumps in each galaxy. f_1/f_2 is the ratio between the brightest and the second brightest clumps, while f_2/f_3 is that between the second and third brightest clumps. The red line shows the criteria for clumpy galaxies ($f_1/f_2 \geq 0.3$ & $f_2/f_3 \geq 0.3$).

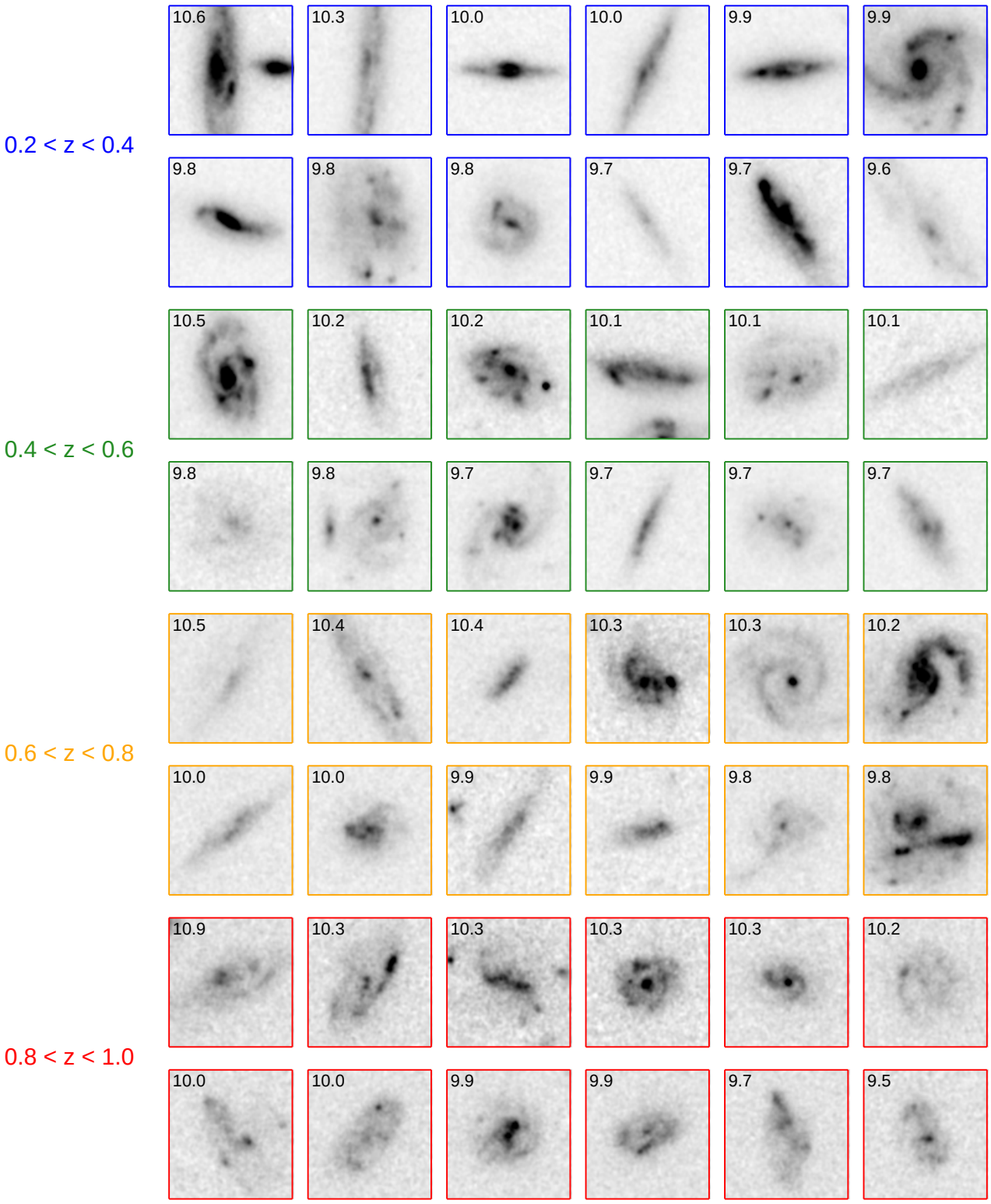

Fig. 2.— Examples of clumpy galaxies with $M_{\rm star} > 10^{9.5} M_{\odot}$ randomly selected in each redshift bin. Galaxies in each redshift bin are shown in the order of their stellar mass. The number in each panel shows $\log(M_{\rm star}/M_{\odot})$.

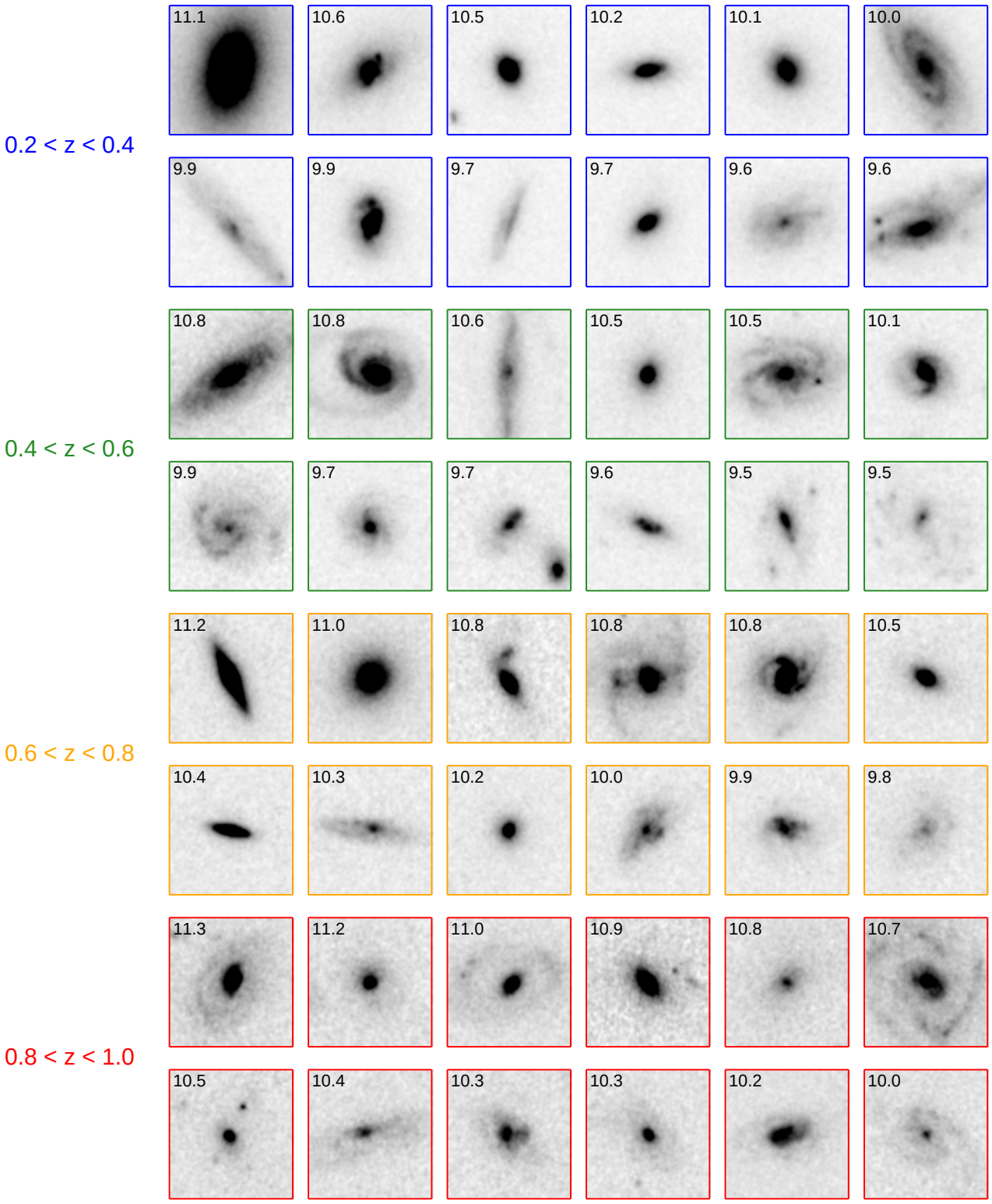

Fig. 3.— The same as Figure 2 but for non-clumpy galaxies.

3. Result

3.1. Stellar Mass and SFR of Clumpy Galaxies

We show the $M_{\rm star}$–SFR diagram for the clumpy and non-clumpy galaxies, respectively, in Figure 4. Relatively small number of galaxies around $M_{\rm star} \sim 10^{9.5} M_{\odot}$ in the both samples is due to the magnitude limit of $I_{\rm F814W} < 22.5$. Since the observed $I_{\rm F814W}$ band samples a shorter rest-frame wavelength at higher redshift, low-mass galaxies with lower SFRs in the high redshift bins tend to be missed by this magnitude limit. We discuss possible systematic effects of the magnitude limit on our results in Section 3.3..

The distribution of non-clumpy galaxies in the $M_{\rm star}$–SFR diagram shows a bimodality, which consists of passively evolving galaxies mainly located at higher stellar mass around $M_{\rm star} \sim 10^{11} M_{\odot}$ and star-forming galaxies located at $M_{\rm star} \lesssim 10^{10.5} M_{\odot}$. The SFRs of star-forming galaxies increase with increasing stellar mass, and they form a sequence in the $M_{\rm star}$–SFR plane, namely, the "main sequence" of star-forming galaxies (e.g., Noeske et al., 2007). The SFRs of star-forming galaxies at a given stellar mass increase with increasing redshift over $0.2 < z < 1.0$. Such distribution of galaxies in the $M_{\rm star}$–SFR plane and its evolution at $z \lesssim 1$ are consistent with previous studies (e.g., Noeske et al., 2007; Santini et al., 2009; Kajisawa et al., 2010).

On the other hand, the clumpy galaxies are preferentially located on the main sequence of star-forming galaxies. In Figure 4, we plot the boundary line of the SFR/$M_{\rm star}$ = 0.1 Gyr^{-1}, which divides galaxies into the passively evolving and star-forming populations, for reference. Since almost all clumpy galaxies lie above the boundary line, especially, at high redshift, they are star-forming galaxies. The range of the SFRs of clumpy galaxies at a given stellar mass is similar to that of the other star-forming galaxies in all the mass and redshift ranges, although their SFRs tend to be higher values as we will show in detail in the following section.

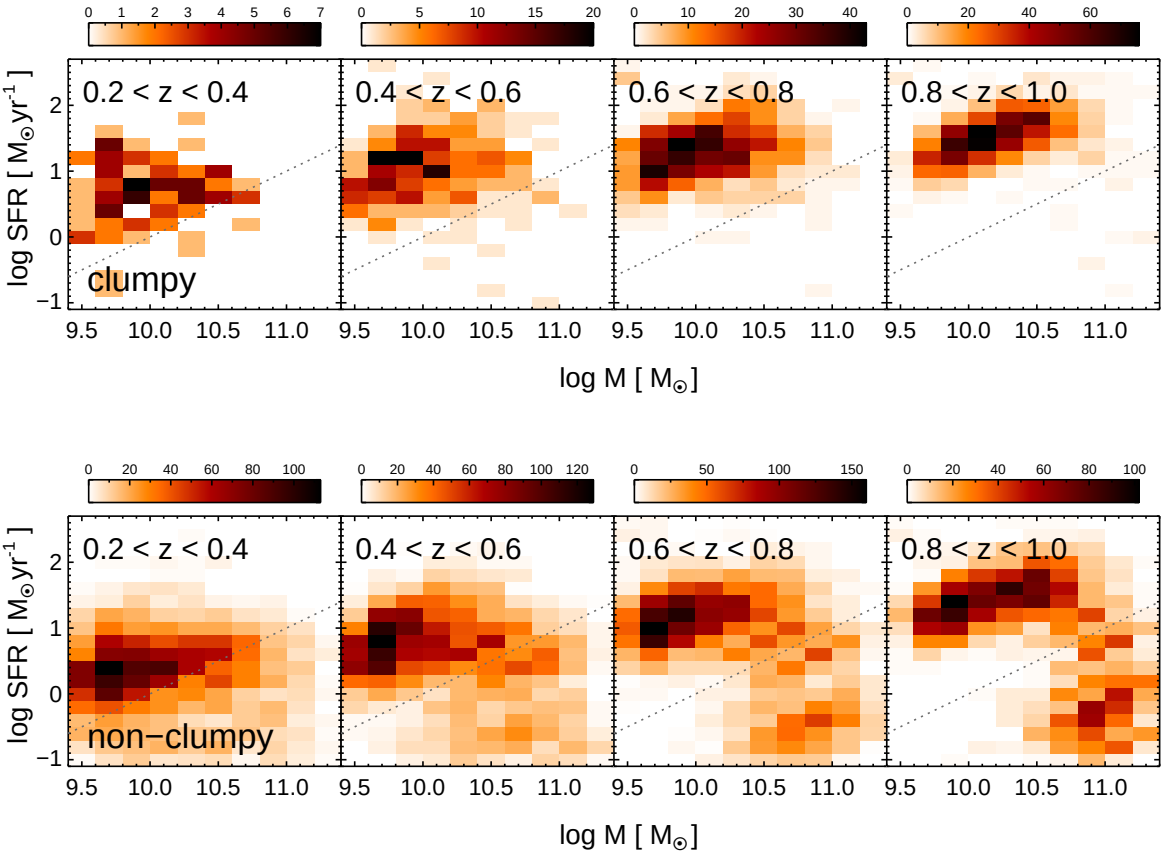

Fig. 4.— SFR vs. stellar mass for clumpy galaxies (top panels) and non-clumpy galaxies (bottom panels) in each redshift bin. The dashed line shows a constant SSFR of 0.1 Gyr^{-1}, above which galaxies are classified as star-forming ones.

3.2. Fraction of Clumpy Galaxies as a Function of Physical Properties

We investigated the fraction of clumpy galaxies in our sample at $0.2 < z < 1.0$ as a function of stellar mass, SFR, and specific SFR (= SFR/$M_{\rm star}$, hereafter SSFR), to study their role in the galaxy evolution and the origins of their morphology. Figure 5 shows the fraction of clumpy galaxies in star-forming galaxies with SSFR > 0.1 Gyr^{-1} as a function of stellar mass for the different redshift bins. The fraction seems to be independent of stellar mass in all the redshift bins, except that the fraction at $0.8 < z < 1.0$ becomes slightly higher around $M_{\rm star} \sim 10^{10} M_{\odot}$. In Figure 4 we can see a concentration of clumpy galaxies at $M_{\rm star} \sim 10^{10} M_{\odot}$ and SFR $\sim 10^{1.5} M_{\odot}$ yr^{-1}, and therefore some fluctuation in the number density of such galaxies in our survey field may cause such high fraction of clumpy galaxies around $M_{\rm star} \sim 10^{10} M_{\odot}$ at $0.8 < z < 1.0$. There may also be the effect of the bias for galaxies with relatively high SSFR near the limiting mass at high redshift caused by the magnitude limit of $I_{\rm F814W} < 22.5$, as we show in Section 3.3.. The fraction of clumpy galaxies decreases with time from ~ 0.3 at $0.8 < z < 1.0$ to ~ 0.05 at $0.2 < z < 0.4$. This is consistent with the results in the previous studies that bright clumpy galaxies are rare in the present universe, while many such galaxies have been observed at $z \gtrsim 1$ (e.g., Elmegreen et al., 2007; Elmegreen et al., 2009b).

We show the fraction of clumpy galaxies in star-forming galaxies with SSFR > 0.1 Gyr^{-1} as a function of SFR in Figure 6. It is shown that the fraction of clumpy galaxies clearly increases with increasing SFR in all the redshift ranges. The fraction at a given SFR decreases with time over the wide range of SFR, although the strength of the evolution seems to depend on SFR. The fraction at SFR $\sim 10^{1.5} M_{\odot}$ yr^{-1} decreases from ~ 0.40 at $0.8 < z < 1.0$ to ~ 0.05 at $0.2 < z < 0.4$, while that at SFR $\sim 10^{0.5} M_{\odot}$ yr^{-1} changes from ~ 0.25 to ~ 0.05 in the same redshift range. A slightly higher fraction around SFR $\sim 10^{1.5} M_{\odot}$ yr^{-1} for galaxies at $0.8 < z < 1.0$ probably corresponds to that at $M_{\rm star} \sim 10^{10} M_{\odot}$ in Figure 5 mentioned above.

Furthermore, we investigated the fraction of clumpy galaxies as a function of SSFR in each mass and redshift range. Figure 7 shows the SSFR distribution and the fraction

of clumpy galaxies as a function of SSFR. In this figure, we used all sample galaxies, including galaxies with SSFR < 0.1 Gyr^{-1}. While the range of SSFRs of clumpy galaxies is similar to that of the other (non-clumpy) star-forming galaxies as shown in Figure 4, the distribution of SSFR of clumpy galaxies tends to be skewed toward higher values. In fact, the fraction of clumpy galaxies clearly increases with increasing SSFR in all the stellar mass and redshift ranges. Interestingly, we found that the fraction at a given SSFR is nearly independent of stellar mass in each redshift bin. In Figure 8, we show the fraction of clumpy galaxies as a function of SSFR for the different mass ranges in the same panel. The SSFR dependences of the fractions for the different stellar mass ranges are similar in each redshift bin, although the uncertainty of each data point is relatively large, especially at very high SSFR. In all the redshift ranges, we can see that the fraction increases with SSFR at SSFR > 0.1 Gyr^{-1}, while it is negligible at SSFR < 0.1 Gyr^{-1}. We can also see that the fraction of clumpy galaxies at a given SSFR decreases with time. For example, the fraction at SSFR ~ 1 Gyr^{-1} changes from ~ 0.25 at $0.8 < z < 1.0$ to ~ 0.10, while that at SSFR ~ 10 Gyr^{-1} decreases from ~ 0.5 to ~ 0.2 in the same redshift range. We fit the data points at SSFR > 0.1 Gyr^{-1} in each panel of Figure 7 with a linear line of $f_{\rm clumpy} = a \times [\log({\rm SSFR}) - 1.0]$, which satisfies $f_{\rm clumpy} = 0$ at $\log({\rm SSFR}) = -1$ (the dashed lines in the figure). The best-fit slope of the linear line on the $f_{\rm clumpy}$ – $\log({\rm SSFR})$ plane clearly becomes steeper with redshift. Therefore, the fraction of clumpy galaxies at a given SSFR does not depend on stellar mass at each redshift, but evolves with time from $z \sim 1$ to $z \sim 0.2$.

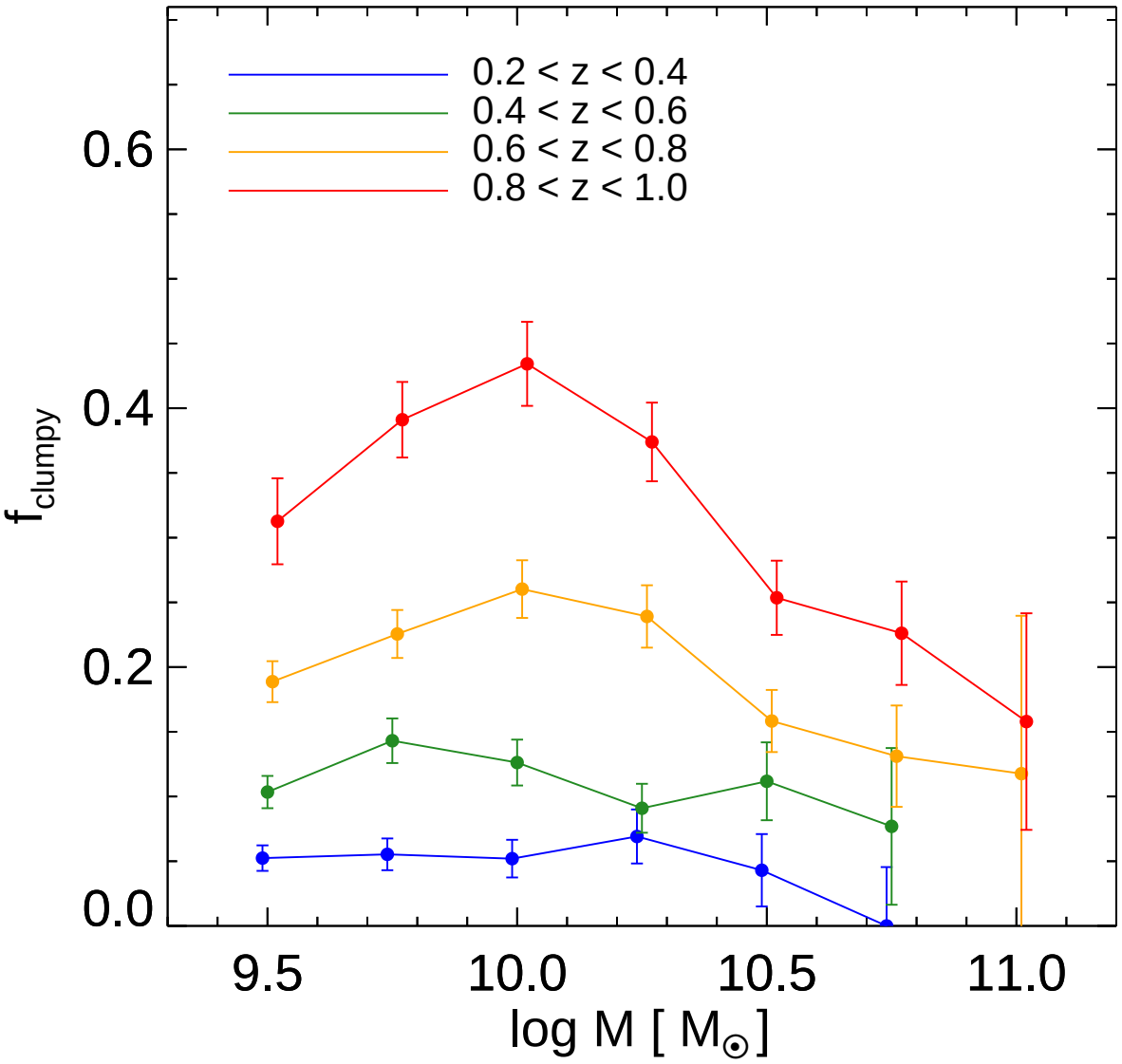

Fig. 5.— Fraction of clumpy galaxies in star-forming galaxies with SSFR > 0.1 Gyr^{-1} as a function of stellar mass for the different redshift bins. The error bars are based on the Poisson statistics.

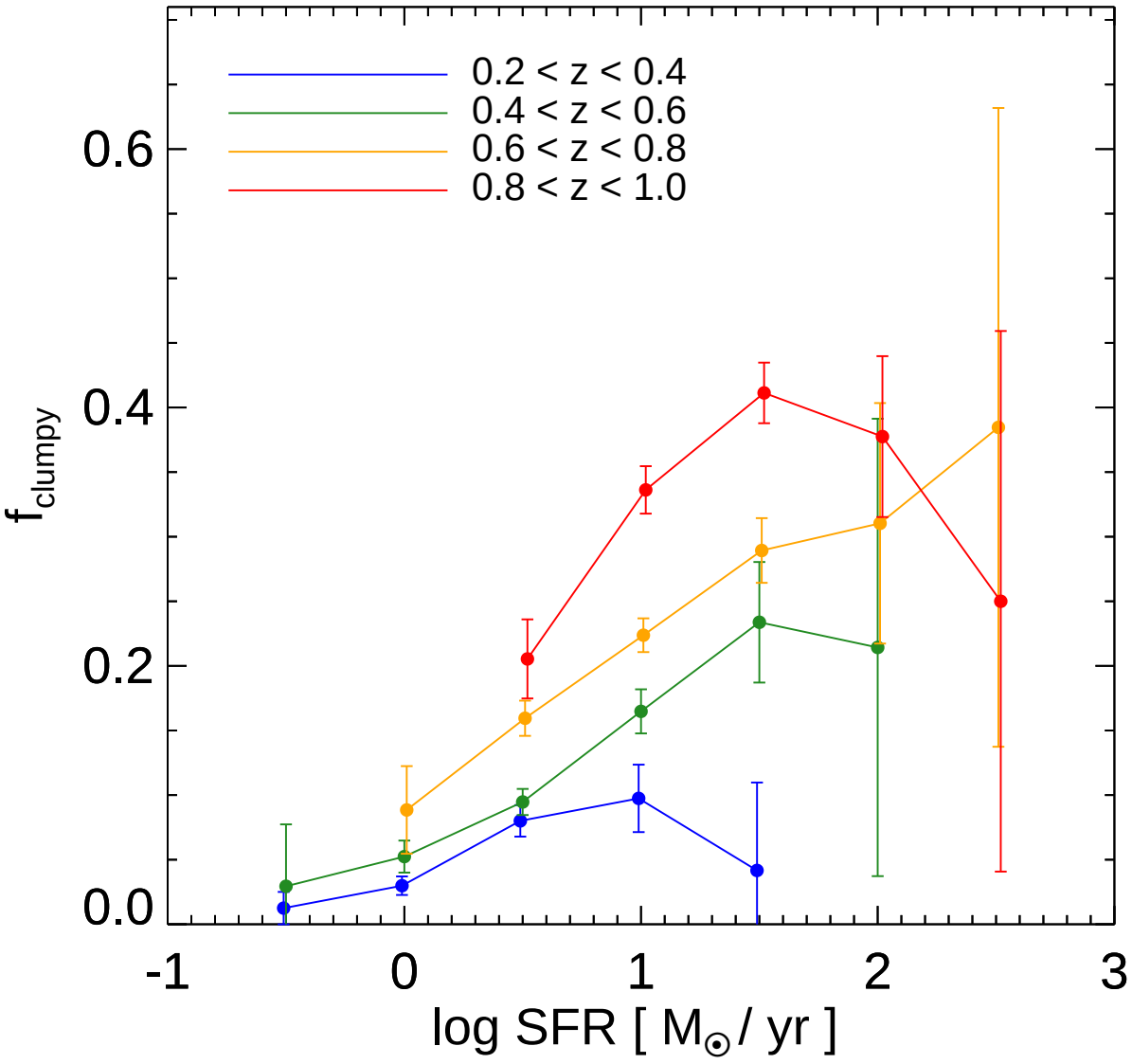

Fig. 6.— Fraction of clumpy galaxies in star-forming galaxies with $M_{\rm star} > 10^{9.5} M_{\odot}$ as a function of SFR for the different redshift bins. The error bars are based on the Poisson statistics.

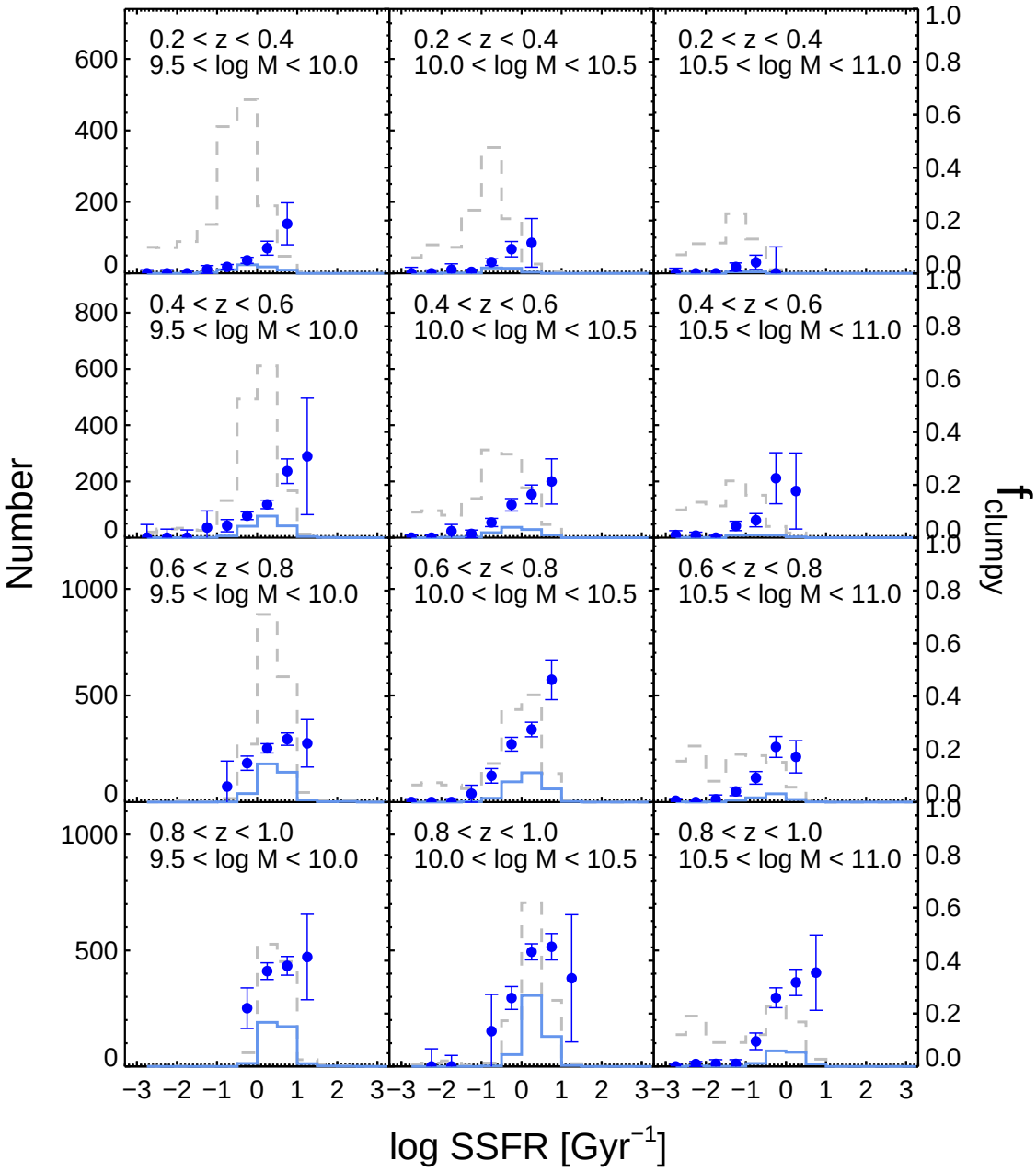

Fig. 7.— SSFR distribution for clumpy and non-clumpy galaxies (histograms) for each redshift and stellar mass bin. The fraction of clumpy galaxies is also shown as a function of SSFR (solid circles, right ordinate). The solid histogram shows clumpy galaxies, while the dashed histogram represents non-clumpy galaxies. The error bars are based on the Poisson statistics.

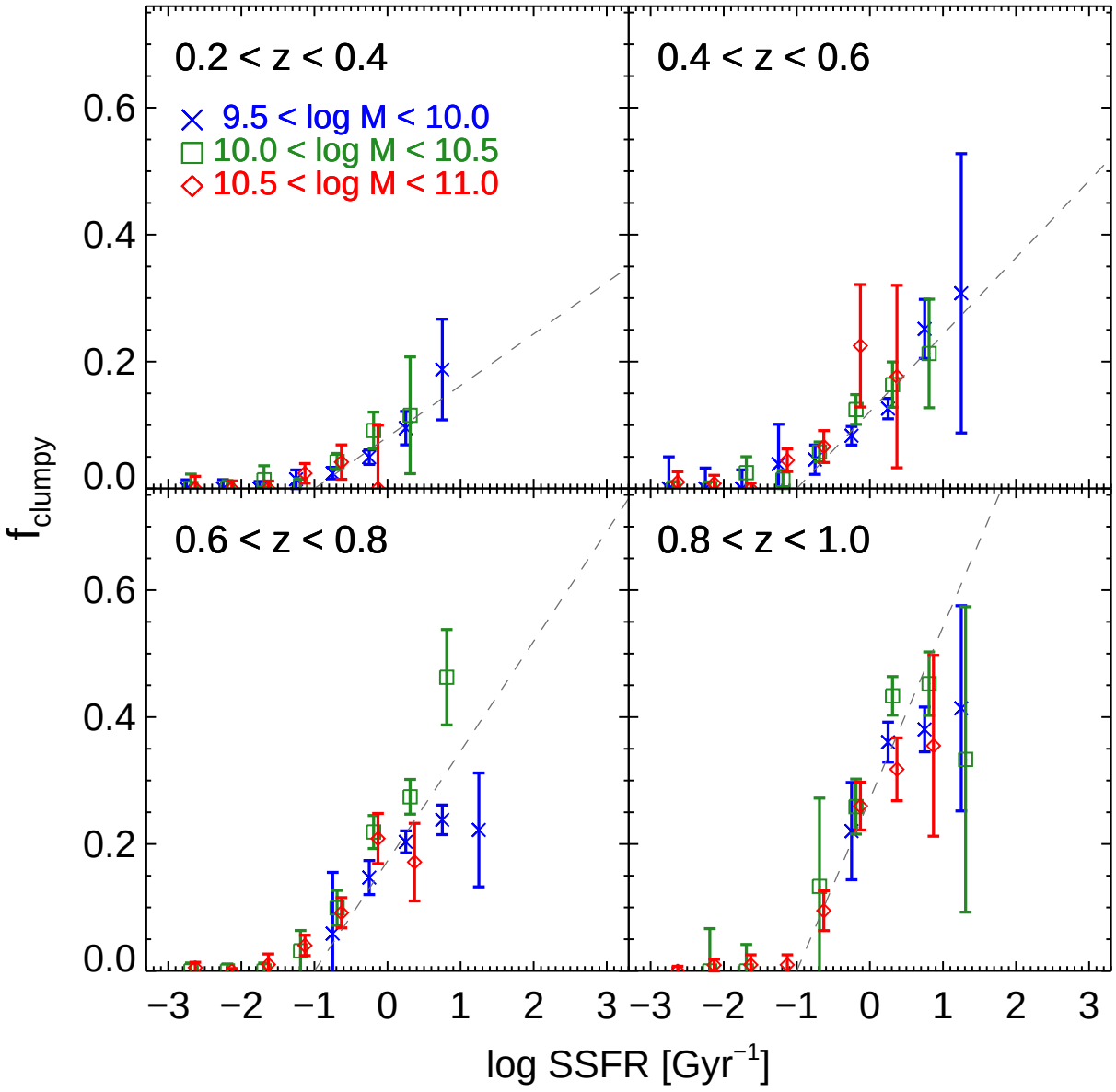

Fig. 8.— Fraction of clumpy galaxies as a function of SSFR for each redshift bin. The fractions for the different stellar mass ranges are shown in the same panel. The dashed line represents the fitting result of the data points at SSFR > 0.1 Gyr^{-1} with a linear line of $f_{\rm clumpy} = a \times [\log(\mathrm{SSFR}) - 1.0]$, where a is a free parameter.

3.3. Possible Biases in Our Analysis

In this section, we checked the effects of possible biases on our results in the previous sections. First, we considered the effects of our magnitude limit of $I_{\rm F814W} < 22.5$, which is set to ensure a secure selection of clumpy galaxies. Since the observed $I_{\rm F814W}$ band samples the rest-frame B band at $z \sim 0.9$, the relatively bright $I_{\rm F814W}$-band magnitude limit can lead to a bias for galaxies with higher SSFRs at lower stellar mass. Therefore we may preferentially miss low-mass galaxies with relatively low SSFRs at higher redshift. In order to check this point, we show the SSFR-$M_{\rm star}$ diagram for galaxies with $I_{\rm F814W} < 22.5$ and those with $I_{\rm F814W} < 25$ in Figure 9. It is shown that galaxies with relatively low SSFRs are missed by the $I_{\rm F814W}$-band magnitude limit at $M_{\rm star} \lesssim 10^{10} M_{\odot}$ in the $0.8 < z < 1.0$ bin, while almost all galaxies with SSFR > 0.1 Gyr^{-1} are picked up down to $M_{\rm star} \sim 10^{9.5} M_{\odot}$ at lower redshifts. In Figure 10, we show the fraction of clumpy galaxies in star-forming galaxies as in Figure 5 but for galaxies with $I_{\rm F814W} < 23.5$. It is shown that the relatively high fraction around $M_{\rm star} \sim 10^{10} M_{\odot}$ for galaxies at $0.8 < z < 1.0$ seen in Figure 5 becomes lower, and the fraction is consistent with a constant value of ~ 0.3. This is because we include low-mass galaxies with relatively low SSFRs at high redshift by using galaxies down to $I_{\rm F814W} = 23.5$. Although we can mitigate the bias against low-mass galaxies with low SSFRs by including more faint galaxies into the sample, we note that the selection of clumpy galaxies becomes less secure for galaxies at $I_{\rm F814W} > 22.5$. On the other hand, the bias caused by the $I_{\rm F814W}$-band magnitude limit does not seem to affect the results in Figures 7 and 8, because the fraction of clumpy galaxies *at a given SSFR* is not changed by this effect. In fact, we performed the same analysis by using the different $I_{\rm F814W}$-band magnitude limits and confirmed that the trends seen in Figures 7 and 8 do not depend on the magnitude limit.

Second, we examined the effect of the morphological K-correction in our analysis. Since we selected our clumpy galaxies in the *HST*/ACS $I_{\rm F814W}$-band images, the morphological selection was done at the rest-frame R band at $z \sim 0.3$, while galaxies at $z \sim 0.9$ were

classified at the rest-frame B band. If the clumps tend to be more conspicuous in shorter wavelengths (e.g., **?**; Wuyts et al., 2012; see also Guo et al., 2012), our ability to select clumpy galaxies could be weaker at lower redshifts. In order to check this effect, we performed the same selection of clumpy galaxies at $0.3 < z < 0.5$, using HST/ACS $V_{\rm F606W}$-band images, which correspond to the rest-frame B band for these galaxies. The $V_{\rm F606W}$-band data were obtained in the CANDELS survey (Grogin et al., 2011; Koekemoer et al., 2011) and cover a field of ~ 260 arcmin^2 in the COSMOS field. Although the area is $\sim$3% of the 2 deg^2 field of the $I_{\rm F814W}$-band data, we can roughly estimate the effect of the morphological K-correction. For ~ 100 star-forming galaxies with SSFR > 0.1 Gyr^{-1} at $0.3 < z < 0.5$, we performed the same morphological analysis with the $V_{\rm F606W}$-band data and found that the fraction of clumpy galaxies increases from ~ 0.1 at the rest-frame V band (the observed $I_{\rm F814}$ band) to ~ 0.3–0.4 at the rest-frame B band. Wuyts et al. (2012) also pointed out that the morphological K-correction significantly affects the fraction of clumpy galaxies at $z \sim 2$. Taking account of these results, we keep in mind the effect of the morphological K-correction when discussing the evolution of the fraction of clumpy galaxies in the following section.

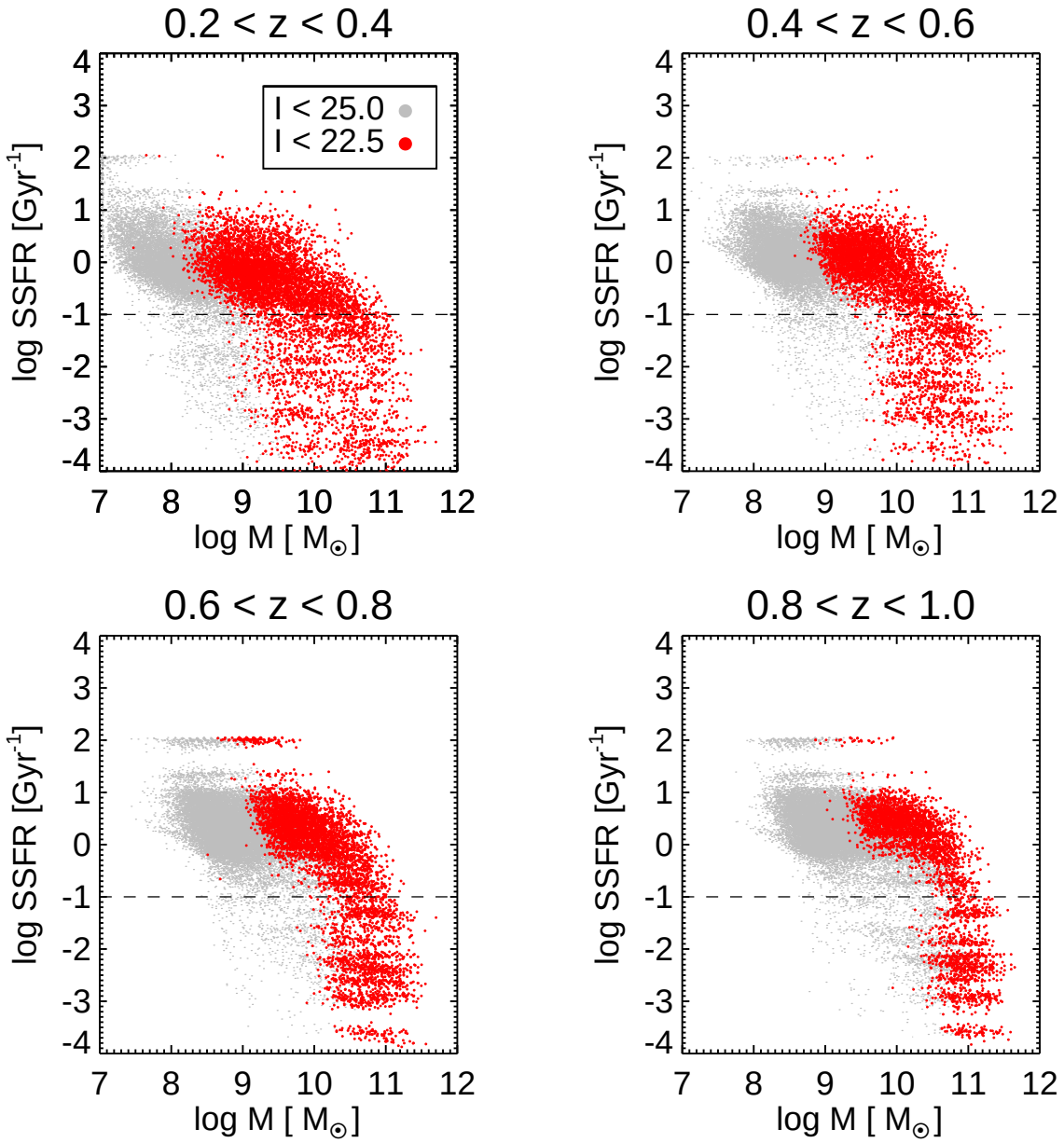

Fig. 9.— SSFR vs. stellar mass for galaxies with $I_{\rm F814W} < 22.5$ (red dots) and for those with $I_{\rm F814W} < 24.0$ (grey dots) for each redshift bin.

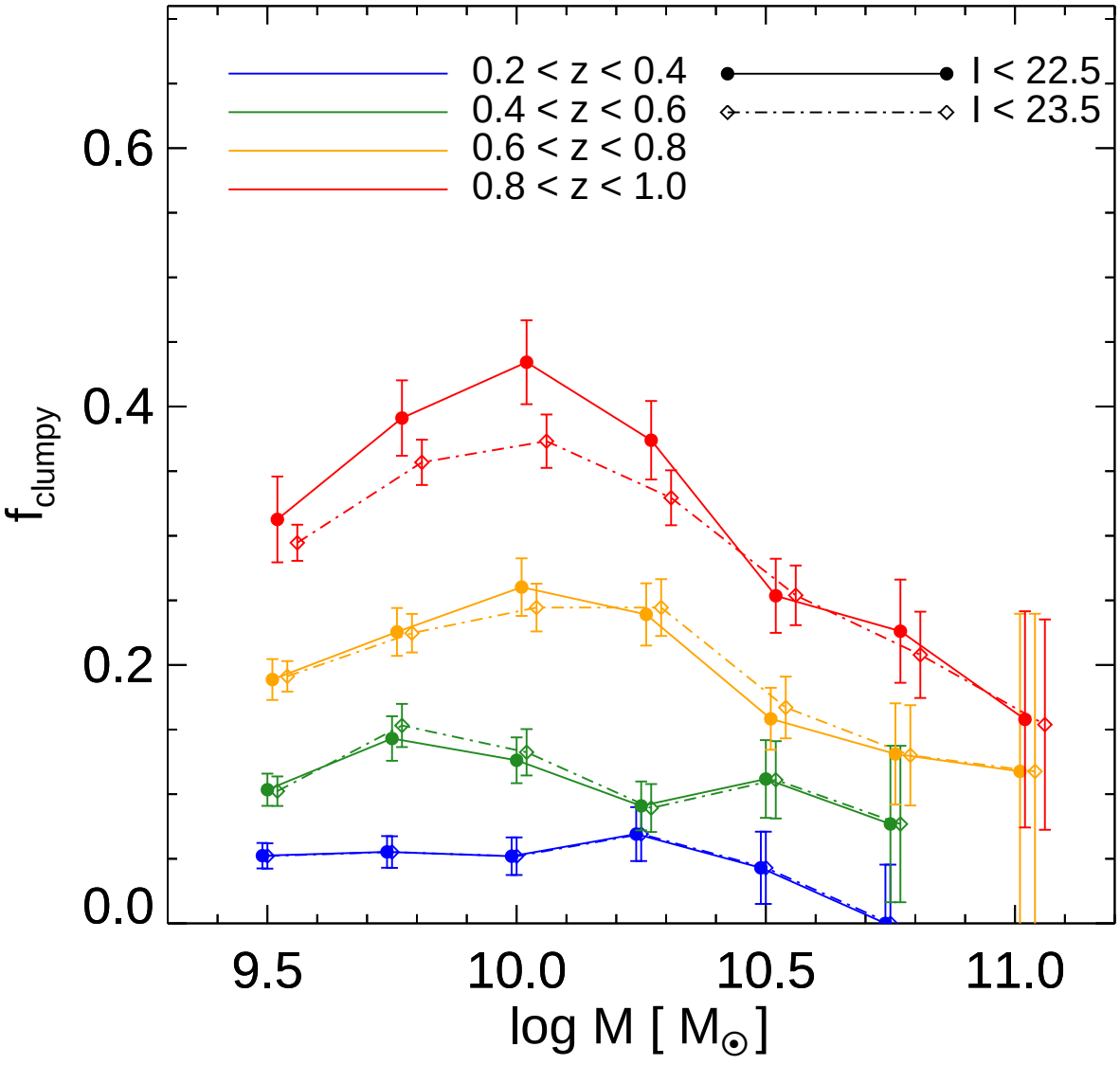

Fig. 10.— The same as Figure 5, but the results for galaxies with $I_{\rm F814W} < 23.5$ are also shown (dashed-dotted lines) as well as those for the basic sample with $I_{\rm F814W} < 22.5$ (solid lines).

4. Discussion

In this study, we constructed a large sample of clumpy galaxies at $0.2 < z < 1.0$ in the COSMOS 2 deg^2 field using the HST/ACS data and investigated the fraction of these galaxies and its evolution as a function of stellar mass, SFR, and SSFR. This is the first systematic search for clumpy galaxies at $z < 1$. Our main results are as follows.

- The fraction of clumpy galaxies in star-forming galaxies decreases with time from ~ 0.3 at $0.8 < z < 1.0$ to ~ 0.05 at $0.2 < z < 0.4$ irrespective of stellar mass.
- The fraction of clumpy galaxies increases with increasing both SFR and SSFR in all the redshift ranges we investigated. In particular, the SSFR dependences of the fractions are similar among galaxies with different stellar masses. Moreover, the fraction at a given SSFR does not depend on stellar mass in each redshift bin.
- The fraction of clumpy galaxies at a given SSFR decreases with time at $SSFR > 0.1$ Gyr^{-1}. This can be explained by the effect of the morphological K-correction.

We discuss these results and their implications for both origins and evolution of clumpy galaxies in the following sections.

4.1. SSFR dependence of the fraction of clumpy galaxies

We found that the fraction of clumpy galaxies increases with increasing both SFR and SSFR. The similar fractions at a given SSFR among galaxies with different stellar masses may indicate that the SSFR is more important and fundamental physical parameter for the origin of the clumpy morphology. Among previous studies on clumpy galaxies, Bournaud et al. (2012) studied 14 clumpy galaxies and 13 smooth disk galaxies at $z \sim 0.7$ selected by an eyeball classification, and found that the average and median SSFRs of clumpy galaxies are higher than those of smooth disk galaxies. Salmi et al. (2012) also reported that clumpy galaxies at $0.5 < z < 1.3$ have systematically higher SSFRs than

the other star-forming galaxies at the same redshifts. They selected clumpy galaxies with a quantitative clumpiness parameter, but their measurement of the clumpiness includes the surface brightness fluctuation on relatively small scales. The SSFR dependence of the fraction of clumpy galaxies seen in Figure 7 is consistent with the results of these previous studies, although the selection methods for clumpy galaxies are different among the studies.

Since the SSFR is a current birth rate of stars to the integrated past star formation rate, it can be considered to represent the evolutionary stages of the stellar mass assembly by the star formation. In this view, the relatively high SSFRs of clumpy galaxies indicates that these galaxies may be systematically in younger stages in their star formation history. We can also consider the SSFR as a proxy for the gas mass to stellar mass ratio, M_{gas}/M_{star}, if we naively assume that the SFRs of galaxies roughly reflect their gas mass. Clumpy galaxies are expected to be (probably young) objects with relatively high gas mass fraction in this case. Recently, the gravitational instability and fragmentation in gas-rich disks is often proposed as a possible origin of the clumpy morphology of high-redshift galaxies, which show both coherent rotation and relatively large velocity dispersion in their gas (e.g., Immeli et al., 2004; Bournaud et al., 2007; Dekel et al., 2009a; Bournaud et al., 2010; Genzel et al., 2012). Gas-rich rotational disks are gravitationally unstable for the fragmentation and lead to the formation of large clumps. In this framework, the gas mass fraction is a key physical parameter. The stability for the gravitational fragmentation of the disks and the maximum unstable mass scale strongly depend on the gas mass fraction (e.g., Escala & Larson, 2008; Cacciato et al., 2012). If the SSFR is closely related to the gas mass fraction, the strong SSFR dependence of the fraction of clumpy galaxies in Figure 7 can be explained by the relationship between the gravitational fragmentation and the gas mass fraction of the rotational disks.

Escala (2011) also discussed that a large maximum unstable mass of gas-rich disks corresponds to a large velocity dispersion of turbulent motions of gas in the self-regulated quasi-stationary state with the Toomre parameter $Q \sim 1$. They also claimed that the large velocity dispersion can cause an enhancement of star formation activity. In fact, the correlation between the mass of the most massive clump of galaxies and their surface SFR density has been observed at $z \gtrsim 1$ (Livermore et al., 2012; Swinbank et al., 2012).

This scenario may explain the relatively higher SSFRs of clumpy galaxies.

Another possible origin of the clumpy morphology is the galaxy merger (e.g., Somerville et al., 2001; Lotz et al., 2004). Morphological studies of high-redshift galaxies and comparisons of these objects with merger galaxies in the nearby universe suggested that some fraction of clumpy and irregular galaxies at $z \gtrsim 1$ are ongoing mergers (e.g., Lotz et al., 2008; Petty et al., 2009; Overzier et al., 2010). Mandelker et al. (2013) also suggested that a non-negligible fraction of large clumps in high-redshift clumpy galaxies come from minor mergers, based on a numerical cosmological simulation of disk galaxies. In this scenario, the SSFR dependence of the fraction of clumpy galaxies can be understood by the enhancement of star formation caused by the galaxy mergers. The galaxy interaction/merger does not only cause disturbed and clumpy morphologies, but also triggers intense star formation. Thus the SSFRs of clumpy galaxies tend to be enhanced from the main sequence of star-forming galaxies. However, it is unclear whether such starbursts by mergers are consistent with the relatively tight SFR-$M_{\rm star}$ relation or not (e.g., Noeske et al., 2007; Elbaz et al., 2007; Renzini, 2009; Wuyts et al., 2011; Rodighiero et al., 2011).

4.2. Evolution of the fraction of clumpy galaxies

We found that the overall fraction of clumpy galaxies in star-forming galaxies with $M_{\rm star} > 10^{9.5} M_{\odot}$ decreases from ~ 0.3 at $z \sim 0.9$ to ~ 0.05 at $z \sim 0.3$. While many actively star-forming galaxies with clumpy morphologies have been observed at $z > 1$ (e.g., Elmegreen et al., 2007; Genzel et al., 2008; Förster Schreiber et al., 2011), most relatively bright galaxies belong to the Hubble sequence and clumpy galaxies are very rare at $z \sim 0$ (e.g., Overzier et al., 2010). Our result naturally connects between these previous studies in the early universe and those in the nearby universe, although the morphological K-correction may affect the result (Section 3.3.). Wuyts et al. (2012) reported that the fraction of clumpy galaxies in star-forming galaxies at $z \sim 1$ is 27 % when the selection for clumps was performed at the rest-frame V band. Our result at $0.8 < z < 1.0$ ($\sim 30\%$), which was obtained at the rest-frame B band (see Section 3.3.), is consistent with their result, although the selection criteria for clumpy galaxies are different.

Another our result of the SSFR dependence of the fraction of clumpy galaxies seen in all the mass and redshift ranges indicates that the evolution of the SSFRs of galaxies leads to the evolution of the fraction of clumpy galaxies. In fact, the median SSFR of star-forming galaxies decreases by ~ 1 dex from $z \sim 0.9$ to $z \sim 0.3$ (Fig. 7). For example, if we assume the relation between the fraction of clumpy galaxies and SSFR at $0.8 < z < 1.0$ shown in Figure 8, the decrease of the SSFR from $SSFR \sim 10^{0.25}$ Gyr^{-1} (median value at $z \sim 0.9$) to $SSFR \sim 10^{-0.75}$ Gyr^{-1} (that at $z \sim 0.3$) corresponds to the evolution of the fraction from ~ 0.3 to ~ 0.05. Thus the evolution of the fraction of clumpy galaxies in star-forming galaxies at $0.2 < z < 1.0$ appear to be explained by the evolution of the SSFR. On the other hand, from such correlation between the fraction of clumpy galaxies and SSFR, the fraction of clumpy galaxies is expected to be higher at higher redshifts, because galaxies tend to have higher SSFRs than those at $z \lesssim 1$. Wuyts et al. (2012) found that the fraction of clumpy galaxies in star-forming galaxies with $M_{\rm star} > 10^{10} M_{\odot}$ at $1.5 < z < 2.5$ is 42% when the morphological selection was done at the rest-frame V band. Tadaki et al. (2013) also reported that 42% of Hα emitters at $z \sim 2.2$ and 2.5 have clumpy morphology, although their clump selection was performed with both rest-frame UV and optical-bands images. The average SSFRs of star-forming galaxies at $z \sim 2$ in both studies are $\sim 10^{0.5}$ Gyr^{-1}, and therefore the fractions of clumpy galaxies of $\sim 40\%$ in these studies seem to be consistent with the relation between the fraction of clumpy galaxies and SSFR at $0.8 < z < 1.0$ shown in Figure 8.

In the gravitational fragmentation model for the formation of giant clumps in disk galaxies, the rapid and smooth streams of gas along filaments effectively penetrate halos of galaxies at high redshift (e.g., Kereš et al., 2005; Dekel et al., 2009b). This "cold accretion" keeps active star formation and a high gas mass fraction of these galaxies, which leads to the formation of the clumpy morphology. In fact, such high gas mass fraction of star-forming galaxies at $z \sim 2$ have been observed (e.g., Daddi et al., 2010; Tacconi et al., 2013), and the observed high turbulent velocity of gas in high-redshift clumpy galaxies also supports this scenario (e.g., Cresci et al., 2009; Förster Schreiber et al., 2009). Using an analytic model, Cacciato et al. (2012) predicted that such disks tend to stabilize at $z \lesssim 1$ mainly due to the decrease of the gas mass fraction. They suggested that the decrease is attributed to the gradual decline of the cosmological accretion rate

into halos of galaxies with time (e.g., Genzel et al., 2008), the gas consumption by the star formation, the inflows of clumps into the center of galaxies by the gravitational torque (e.g, Dekel et al., 2009a), and the gas outflows by the supernova feedback. If the SSFRs of galaxies are closely related to the gas mass fraction as discussed above, the evolution of the fraction of clumpy galaxies at $0.2 < z < 1.0$ could be explained by this scenario. The decrease of the gas mass fraction with time at $z \lesssim 1$ causes the stabilization of galactic disks, while it also leads to the decrease of the SSFRs of these galaxies. The systematic CO observations with ALMA will allow us to investigate the gas mass fraction and gas kinematics of clumpy and non-clumpy star-forming galaxies as a function of SSFR in order to confirm this scenario and understand the origins and evolution of clumpy galaxies.

Finally, we note that the fraction of clumpy galaxies at a given SSFR decreases with time from $z \sim 0.9$ to $z \sim 0.3$. This can be due to the morphological K-correction because we selected clumpy galaxies at the observed $I_{\rm F814W}$ band as discussed in Section 3.3.. If this is the case, the intrinsic fraction of clumpy galaxies at a given SSFR could not depend on redshift. There may be the universal relation between the fraction of clumpy galaxies and SSFR.

Chapter 3

GENUINE TADPOLE GALAXIES IN HIGH REDSHIFT UNIVERSE

1. Abstract

Tadpole galaxies are defined as a galaxy with a bright knot at one end together with a long tail structure in stellar continuum emission. In the local universe, tadpole galaxies are basically either irregular or interacting/merging galaxies. However, since tadpole galaxies at high redshift ($z > 1$) show the so-called cometary structure, it is possible that they are different populations from the local tadpoles. In this study, we select the high-redshift tadpole galaxies whose tadpole structures are not originated from galaxy interaction/merger out of the tadpole catalog in the Hubble Ultra Deep Field. Moreover, we investigate if the ram-pressure or cosmic-web driven formation mechanism works for such high redshift tadpoles that interact with dense intergalactic medium in a quantitative manner. We conclude that the formation sites of tadpole galaxies are numerous enough to reproduce the observed number densities of the tadpoles in our catalog.

2. Introduction

Elliptical and disk galaxies are dominant populations in the local universe. However, there also exist peculiar shaped galaxies. One of the representative peculiar galaxies is

a class of tadpole galaxies, that are defined as a galaxy with a bright knot at one end together with a long tail structure in stellar continuum. Namely, tadpole galaxies has a head-tail structure. The so-called tadpole structure is considered to be originated from galaxy interaction and/or merger and the tadpole galaxies are regarded as dynamically unrelaxed galaxies in the early-stage of interaction/merger (e.g., Windhorst et al. 2006). Ram pressure stripping of gas in dense environment is proposed as another possible origin of the tadpoles (Elmegreen & Elmegreen 2010; Elmegreen et al. 2012). Therefore, the tadpole galaxies are one of the interesting galaxy populations to study the evolution of gas and stars in the early stages of galaxy interaction/merger and/or in interaction with environment.

A couple of well-defined examples of tadpole galaxies at the local universe are collected in the Arp's Catalogue of Peculiar Galaxies (Arp 1966): Arp 266 (= NGC 4861 [Figure 1 (a)]) and Arp 188 (UGC 10214 [Figure 1 (b)]). Although NGC 4861 appears to be a single irregular galaxy, its head is a bright star-forming knot identified as Mrk 59. On the other hand, UGC 10214 consists of a disturbed barred spiral galaxy with a long tidal tail, being interpreted as a consequence of a galaxy merger. In fact, some well-known major merger remnants such as Mrk 273 also show a tadpole-like morphology [Figure 1 (c)]. Therefore, it is considered that tadpole galaxies in the local universe are heterogeneous in their origin (Elmegreen et al. 2012).

Although tadpole galaxies are very rare in the local universe, they are more common in the young universe. Tadpole galaxies at high redshift was first identified in the Hubble Deep Field (HDF; van den Bergh et al. 1996). More than 100 tadpole galaxies are also found in the Hubble Ultra Deep Field (UDF; Elmegreen et al, 2005; Elmegreen & Elmegreen 2010; Starughn et al. 2006). However, tadpole galaxies identified by the previous works are often indistinguishable from chain galaxies, that are also selectively found at high redshift (Cowie et al. 1995; van den Bergh et al. 1996; Elmegreen & Elmegreen 2005, 2006, 2010; Elmegreen et al. 2004a, b, 2007, 2009). Another relevant population is clump-cluster galaxies found by Elmegreen et al. (2004a). Since they propose that clump-cluster galaxies are face-on counterparts of chain galaxies, we also need take account of this population when we consider the origin of tadpole galaxies.

In this study, our first step is to identify various types of tadpole galaxies from the representative tadpole galaxies in the local universe and then classify them unambiguously. These processes are absolutely necessary to understand the origin of tadpole galaxies at high redshift. If there is a new population of tadpole galaxies at high redshift that are different from local tadpole galaxies, detailed investigations of such galaxies will give us a new guideline to understand the early evolution of galaxies. Moreover, we provide a quantitative estimate, for the first time, whether or not the ram pressure in dense gas environment is sufficient to strip gas from the progenitors of tadpole and to explain the number density of observed tadpoles.

3. Observational Characteristics of the Representative Tadpole Galaxies

The morphological definition of tadpole galaxies is quite simple: that is, head-tail structure in stellar continuum emission. However, tadpole galaxies appear to be heterogeneous. In particular, tadpole galaxies in the nearby universe seem to consist of several types. In this section, we first show the observational properties of the tadpole galaxies both at

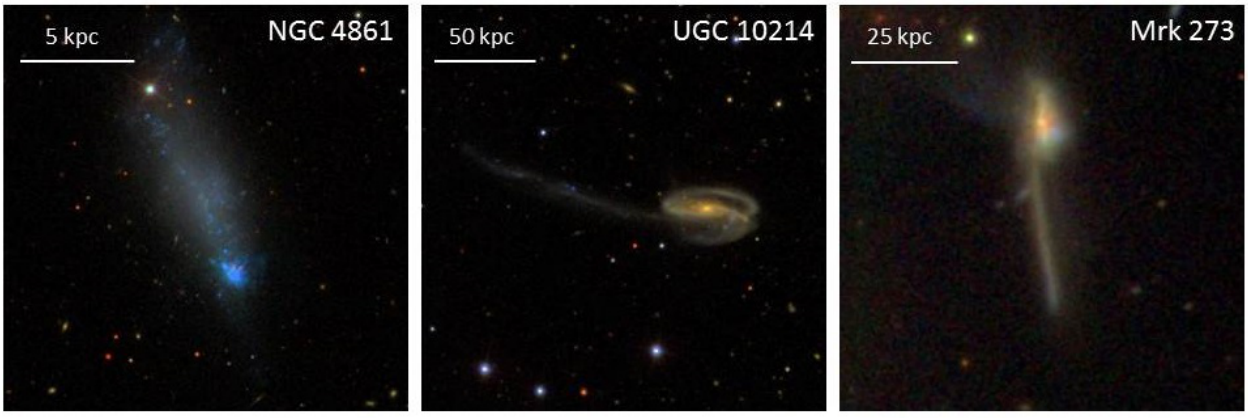

Fig. 1.— Tadpole galaxies in the local Universe taken from the SDSS Data Release 10: (a) NGC 4861, (b) UGC 10214, and (c) Mrk 231. North is up and east is left. Image sizes for the panels of (a), (b), and (c) are 300 arcsec × 300 arcsec, 300 arcsec × 300 arcsec, and 120 arcsec × 120 arcsec, respectively. For reference, physical scales of 5 kpc, 50 kpc, and 25 kpc in panels (a), (b), and (c) are indicated by the bars, respectively.

low- and high-redshift universe in Section 3.1. and 3.5., respectively. Then we discuss their possible origins and propose a new classification scheme in Section 3.8..

3.1. Local Tadpole Galaxies

By definition of tadpole galaxies, they show a head-tail structure; the head is a bright clump located at one edge of the main body and tail is extending from the head. However, there seem to exist the following three types of the head in the nearby tadpole galaxies [see also Elmegreen et al. (2012) and references therein]:

- The head is a bright knot at an edge of the main body of a galaxy which seems to be a tail
- The head consists of a galaxy with a long tail
- The head is a merger remnant with a long tail

The representative galaxies of the above three types are NGC 4861, UGC 10214, and Mrk 273, respectively. We show their observational properties in the following subsections.

3.2. NGC 4861

NGC 4861 appears to be an edge-on disk or irregular galaxy with $M_B \sim -18.2$ at a distance of 12.4 Mpc. As shown in Figure 1 (a), one bright knot is seen at the SW edge of the main body of NGC 4861, making its overall appearance peculiar. The knot is an intense star forming region identified as Mrk 59 (e.g., Wakamatsu 1979), which emits strong nebular emissions including Hα (Carozzi et al. 1974). From Hα observations, it is found that the main bright part of NGC 4861 including Mrk 59 shows a rotation as a normal late-type spiral, while the NE part of the main body shows a rapid decrease in radial velocity more than 50 km s^{-1} (Carozzi et al. 1974).

Although NGC 4861 is confirmed as a normal late-type spiral according to its normal rotation curve including the bright knot of Mrk 59, it can also be interpreted as a minor

merger scenario. We suggest that a dwarf gas-rich satellite, which is now observed as Mrk 59, is merging into the main body of NGC 4861. Absence of a tidal tail can be resolved if it is almost aligned with the line of sight; in this scenario, the NE part of the main body, at which a rapid decrease in radial velocity is observed, could be a candidate of the tidal tail. Although this scenario is not so conspicuous like the following case of UGC 10214, faint tidal stream structures found in $\sim 20\%$ of ~ 500 galaxies in the nearby universe (Miskolczi, Bomans, & Dettmar 2011). The Andromeda galaxy, M 31, and our own Milky Way also have such tidal streams made by minor mergers of dwarf satellite galaxies (e.g., Ibata et al. 2001, 2002).

It is finally noted that, in the catalog of UV-excess galaxies taken by the Kiso Schmidt telescope (Miyauchi-Isobe 2010), NGC 4861-type or irregular-type local tadpole galaxies have been identified (Elmegreen et al. 2012). As their alternatives to galaxy merger, Elmegreen et al. (2012) briefly suggested a ram pressure stripping in dense gas environment such as galaxy clusters and a random collapse of disk gas with large Jeans length comparable to the galaxy radius. They also commented that these origins naturally reproduce the lower fraction of tadpoles in the local universe than at high redshift universe.

3.3. UGC 10214

UGC 10214 is one of the typical tadpole galaxies with $M_B \sim -21.2$ at distance of 136.7 Mpc. As shown in Figure 1 (b), its spectacular feature is a long tail structure (~ 100 kpc; Briggs et al. 2001) extending to EEN direction from the main body of UGC 10214. The main body of UGC 10214 is a disturbed barred spiral galaxy. H I observations by Briggs et al. (2001) show that there are three H I components. Two of them are associated with the main body or the long tail. The remaining component is located at the western edge of the main body, at which we can see a small structure in Figure 1 (b). It is suggested that the third H I component is associated with the merging partner.

UGC 10214 is considered to represent an ongoing merger between a massive spiral and smaller companion, which are the main body of UGC 10214 and the third H I component,

respectively. Therefore, tadpole structure is caused by a minor merger between two (or more) galaxies. A schematic picture of the structures in UGC 10214 system is given in Figure 13 of Briggs et al. (2001).

3.4. Mrk 273

Mrk 273 (= IRAS 13428+5608) is one of the ultra luminous infrared galaxies studied by Sanders et al. (1988) with $M_B \sim -22.0$ located at a distance of 163.5 Mpc. The long tail extending to S direction from the main body of Mrk 273 is the most conspicuous feature, described by Markarian (1969) as an "*exceedingly interesting galaxy with large straight protrusion*". As shown in Figure 1 (c), the tail has a dust lane across the head of Mrk 273. Indeed, radio observation by Cole et al. (1999) reveals the H I absorption in the head of Mrk 273. Two distinct components in radio continuum emission are also found, which are associated with optical components. It indicates that Mrk 273 has a double nucleus due to a recent major merger event.

Although most of major merger remnants show a pair of tidal tails (e.g., Arp 220, Mrk 231, and so on), a number of them including Mrk 273 have only one tidal tail. Observational morphology of tidal tails depend on the number of merging galaxies, dynamical properties of progenitors, orbits, and viewing angle. A single dominant tidal arm can be made by a multiple galaxy merger model studied by Bekki (2001).

3.5. High-Redshift Tadpole Galaxies

We may expect that there are the same three types of tadpole galaxies as those for low-redshift tadpoles described in Section 3.1.. However, in general, identifying the head-tail structure of tadpole galaxies becomes more difficult if they are located at higher redshift. It is because both high angular resolution and sensitivity are required to identify the head-tail structure of tadpole galaxies. The difficulty was resolved by the emergence of the Hubble Space Telescope (HST). To date, a number of high-redshift tadpole galaxies have been identified in the HDF (van den Bergh et al. 1996) and the UDF (Elmegreen et

al. 2005; Straughn et al. 2006).

3.6. Representative High-Redshift Tadpoles

We first examine the characteristic features in the head, tail, and/or whole structure of the high-redshift tadpoles by using a representative catalog of them in the UDF provided by Elmegreen et al. (2005; hereafter E05). We obtain the F775W-band (i_{775}-band) image in the UDF taken by the HST/ACS from the Space Telescope Science Institute (STScI) archive[*1]. Through cross-matching the UDF IDs given in E05 and those of the original UDF catalog, we obtain the i_{775}-band images of all tadpole galaxies in the E05 catalog. For eight tadpoles in E05 without the UDF IDs, their R.A. (J2000.0) and decl. (J2000.0) provided in E05 are used to obtain their images. Then, in order not to miss any faint structures, we check the morphologies in several images for each galaxy with different contrasts.

We find that some samples like UDF 6119 and UDF 9848, shown in the left and middle panels of Figure 2, do not have the so-called tadpole structure: that is, the head-tail structure. UDF 6119 seems to have double components in the head instead of the head-tail structure. UDF 9848 has two head-tail structures extended from the clump into the opposite directions. These features can be interpreted as a consequence of recent galaxy interaction and/or merger. We also find that some tadpole galaxies like UDF 7862, shown in the right panel of Figure 2, represent a clear signature of galaxy interaction. There seems to be two clumps in UDF 7862, which are interpreted as two merging galaxies, connected with a fuzzy component, suggesting an ongoing major merger event between two galaxies.

Among the remaining samples of the tadpole galaxies in E05, we find that they can be classified into the following two types according to the features in the tail:

(i) The tail is detached from the head

(ii) The tail is smoothly connected with the head

[*1] http://archive.stsci.edu/pub/hlsp/udf/acs-wfc/.

The representative tadpoles for the above two types are shown with their schematic images in Figures 3 and 4, respectively.

3.7. Caution on Possible Contamination to Tadpoles

In high-redshift universe, another type of irregular galaxies, chain and clump-cluster galaxies, are more common than the tadpole galaxies (e.g., van den Bergh et al. 1996; Elmegreen et al. 2004a, b, 2005, 2007; Elmegreen & Elmegreen 2010 and references therein). For example, Elmegreen et al. (2007) have found a larger number of chain and clump-cluster galaxies than that of tadpoles by a factor of ~ 5 among their catalog of the galaxies at $z \sim 1$–4 in the UDF. We note that, even in the high-quality imaging data obtained with the HST, such clump-dominated galaxies can be contaminants to tadpole galaxies and vice versa. This is because they shows a quite similar morphology with each other. Indeed, we find some tadpole-like galaxies in the chain galaxy sample studied by E05. We present the images of such galaxies in Figure 5.

As shown in Figure 5, their overall appearances are quite similar to one of the representative tadpoles at local universe, NGC 4861, shown in Figure 1 (a). E05 classified

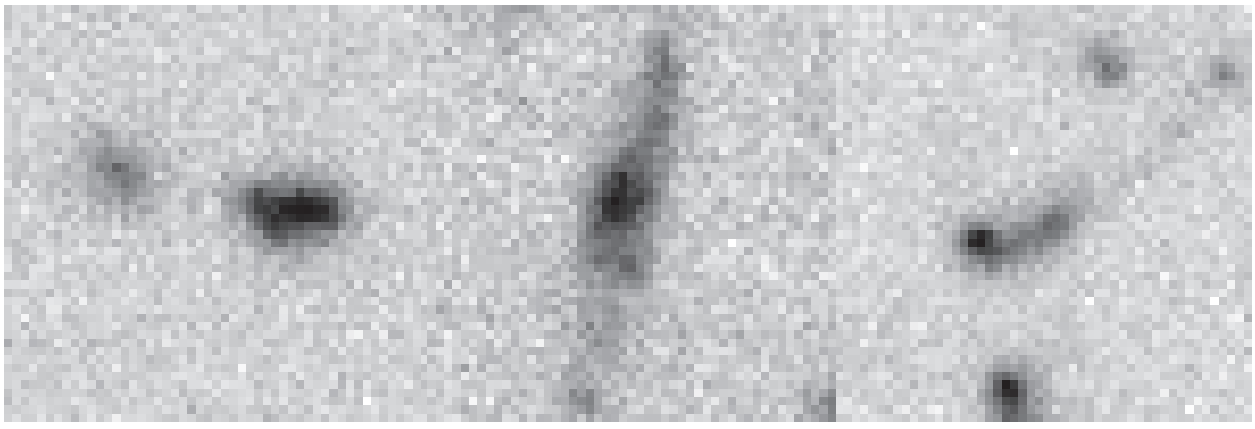

Fig. 2.— HST/ACS i_{775}-band images of the tadpole galaxies without the head-tail structure and with a signature of galaxy interaction from the tadpole catalog in the UDF given by Elmegreen et al. (2005). North is up and east is left. Image sizes are 1.5 arcsec × 1.5 arcsec. The object IDs are UDF 6119 (double components), UDF 9848 (double tails), and UDF 7862 (interaction) from left to right.

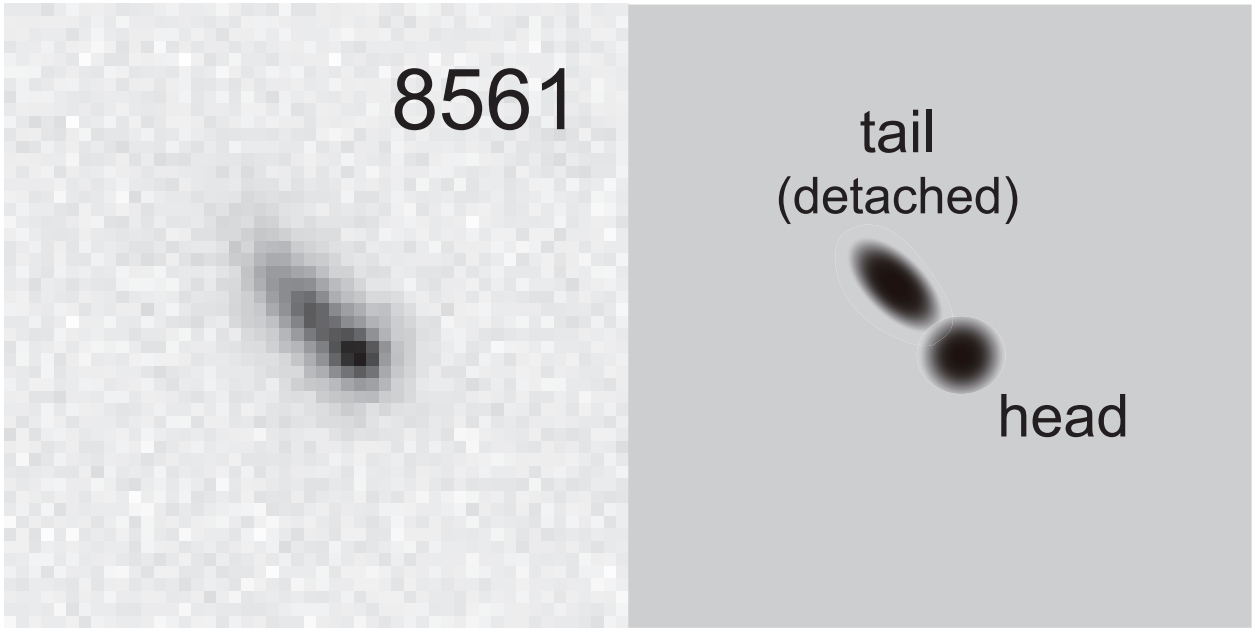

Fig. 3.— (*Left*) HST/ACS i_{775}-band image of a tadpole galaxy having a tail detached from the head, UDF 8561, chosen from the tadpole catalog in the UDF given by E05. North is up and east is left. Image sizes are 1.5 arcsec × 1.5 arcsec. (*Right*) A schematic image of such tadpole galaxies having a detached-tail.

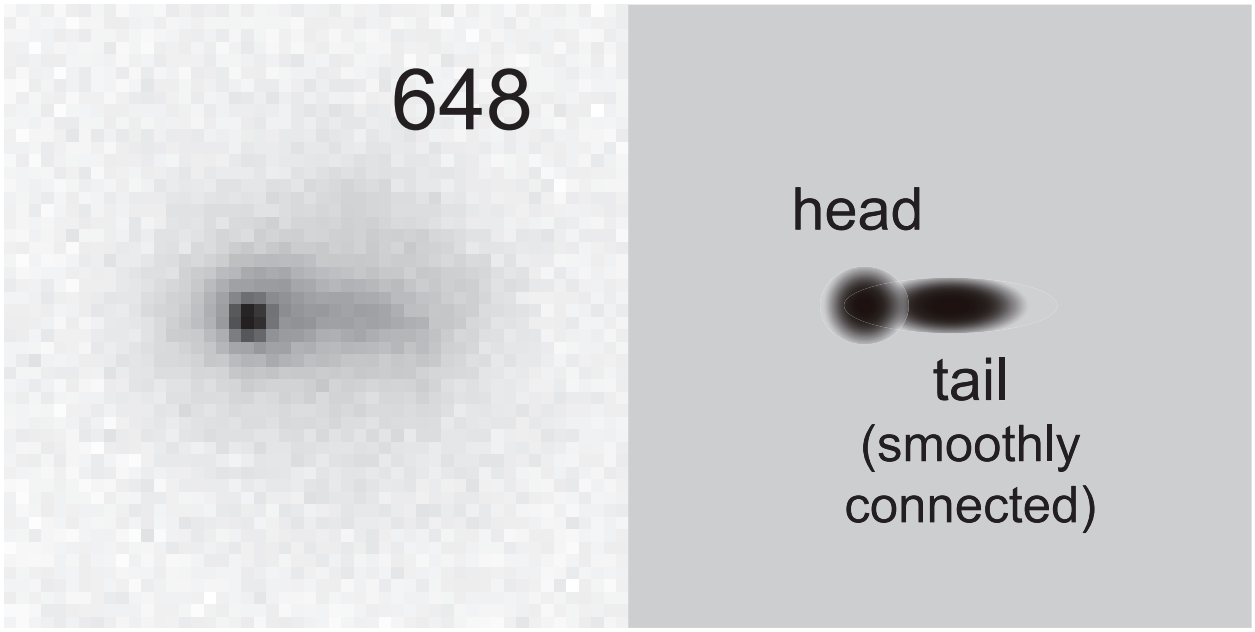

Fig. 4.— Same as Figure 3 but for the tadpoles having a smoothly connected tail with the head. The object ID is UDF 648.

these galaxies into a class of chain galaxy by eye inspection since there exist several clumps in the tail. It is true for the UDF 5787 shown in the left panel of Figure 5; the galaxy have at least three clumps in the tail. However, the UDF 3458+3418 in the right panel does not have any conspicuous clumps in the tail and hence it should be classified into a class of tadpole galaxy. Therefore, more careful selection and consideration are necessary to obtain a clean catalog of tadpole and/or clump-dominated galaxies and to understand their origins.

3.8. Classification of Tadpole Galaxies

Receiving the observational characteristics of both local and high redshift tadpole galaxies described in the previous subsections, we provide the following classification for tadpole galaxies at high redshift:

(1) Merger-driven tadpole galaxies

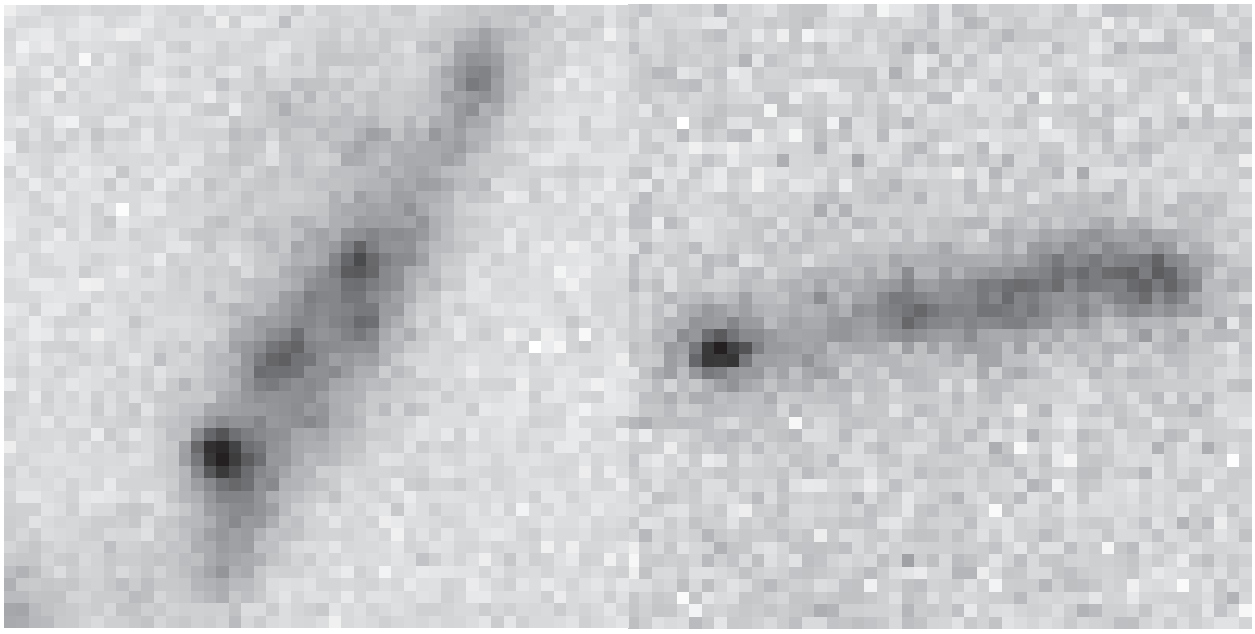

Fig. 5.— Same as Figure 3 but for the chain galaxies from the chain galaxy catalog of Elmegreen et al. (2005). The object IDs of the left and right objects are UDF 5787 and UDF 3458+3418, respectively. Note that the UDF 5787 in the left panel is indeed a chain galaxy but the UDF 3458+3418 in the right panel should be classified into tadpole.

(2) Genuine tadpole galaxies

The tadpole galaxies in the first classification are the tadpoles which show clear signature of galaxy interaction and/or merger (e.g., double clump and/or curved-tail). Their tadpole structures are considered to be caused by galaxy merger and/or interaction; the head consists of two (or more) merging galaxies or a dominant galaxy and the tail is elongated tidal tail. On the other hand, the tadpoles in the second classification are the isolated tadpoles which do not show such signature. Therefore, their origin(s) is in question and that is why we call them as "genuine" tadpole galaxies (GTGs).

The representative tadpole galaxies at local universe for the above classification (1) are NGC 4861, UGC 10214, and Mrk 273 shown in Figure 1. UDF 7862 is also classified into this class (1). On the other hand, the representative tadpoles for the classification (2) are not found in the local universe. Therefore, the GTG is a new type of tadpole galaxies only at high-redshift universe. However, we should note that, as detecting signature of galaxy interaction and/or merger is getting more difficult for the galaxies at higher redshift, some tadpoles identified as GTGs can be the galaxies in interaction/merger. Nevertheless, it is worthwhile to pick up the tadpole galaxies which do not show clear signature of galaxy interaction/merger since such tadpoles can include the tadpoles whose origin is not galaxy interaction/merger, that is, GTGs.

According to the case studies described in Section 3.6., the GTG should be further classified into following two subclasses:

(2-1) Class I GTG
(2-2) Class II GTG

Following our findings in Section 3.6., the class I GTG is the tadpole galaxies at high redshift showing a detached tail from the head, while the class II GTG is those having a smoothly connected tail with the head. The images of the representative galaxies classified into the class I and II GTGs are presented in Figures 3 and 4, respectively. The morphological difference seen in the tails of the class I and II GTGs may simply be attributed to a difference of viewing angle. However, it can be possible that the

morphological difference is originated from differences in evolutionary stage and/or in origin. We will discuss what the morphological difference implies in Section 5.4. briefly.

It should be noted that the tadpole morphology is also explained by the projection effect of two physically unrelated galaxies with an edge-on late-type disk galaxy and a round-shaped dwarf galaxy as shown in Figure 12. Although it is difficult to estimate how often such events occur in the universe, we cannot rule out this possibility. Such "apparent" tadpole galaxies may be present in the current samples of tadpole galaxies studied to date because such chance events are often observed in the universe. One example is Stephan quintet in which one spiral galaxy is a foreground object that is not physically related to the other four galaxies. Such accidental overlaps are also found in a pair of galaxies (e.g., Keel & White 2001; de Grijs & Robertson 2006; Keel et al. 2013; Nakahiro et al. 2013).

We summarize our classification scheme as a schematic picture in Figure 7.

4. Samples of Genuine Tadpole Galaxies

In the previous section, we have proposed a classification for high-redshift tadpole galaxies following our findings from the studies for the representative high-redshift tadpoles. This

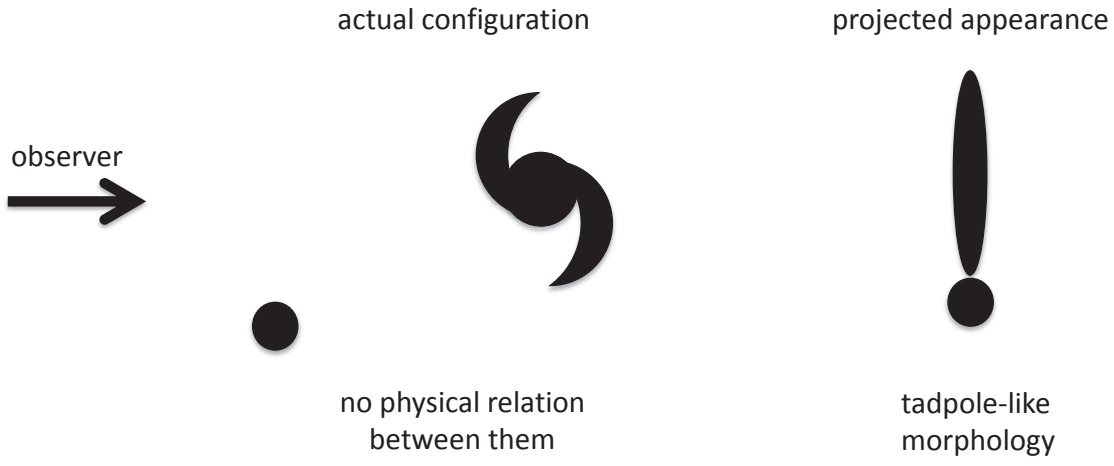

Fig. 6.— Schematic view of the projection effect to result in the tadpole structure.

include the GTG, which is a characteristic class of tadpole galaxies at high redshift. Here, we show the samples of both the class I and II GTGs identified from the tadpole galaxy catalog in E05. As described in Section 3.5., there exist some tadpole galaxies in the chain and/or clump-cluster galaxy catalogs in E05. However, for simplicity, we examine to select the GTGs only from the tadpole galaxy catalog in E05.

4.1. Tadpole Galaxy Catalog of Elmegreen et al. (2005)

E05 have identified astronomical sources using the archival i_{775}-band images taken by the HST/ACS in the whole UDF. They have searched by eye extended objects whose major axes are larger than 10 pixels (i.e., 0".3) in contour plots out to the 2σ limit of the i_{775}-band. Any criteria neither for redshift nor magnitude have not been adopted. They have identified 884 galaxies[*2], including 97 tadpole galaxies that are listed up in their Table 4. However, two objects (UDF 176 and UDF 3823) are also entered in other types of morphology[*3]. Therefore, we use the remaining 95 tadpole galaxies in our analysis.

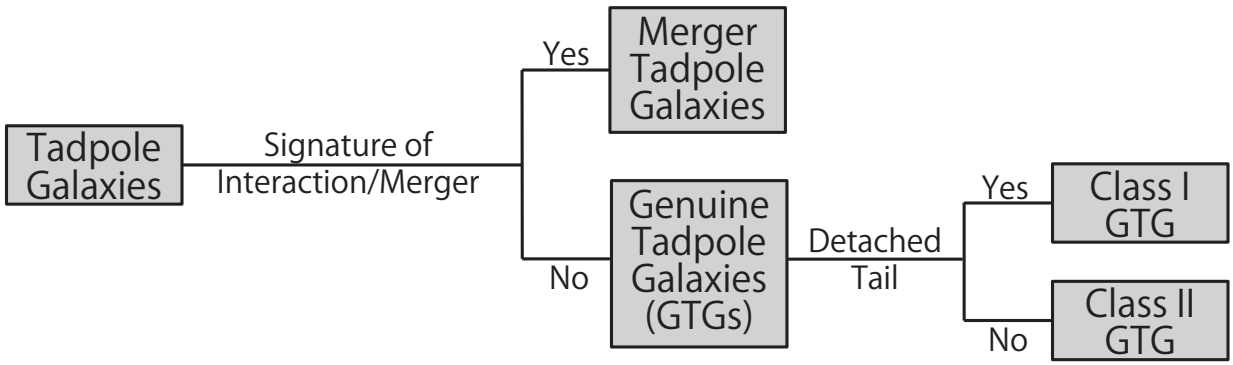

Fig. 7.— The schematic picture of our classification scheme for high-redshift tadpole galaxies.

[*2] As the selection method of E05 is completely independent of that adopted in the original UDF catalog, their samples of galaxies include the galaxies which are not listed in the UDF catalog.

[*3] UDF 176 and UDF 3823 are also listed up in the catalog of elliptical galaxies (their Table 6) and spiral galaxies (their Tables 5), respectively.

66 out of 97 tadpole galaxies in the E05 catalog have photometric redshifts as well as the physical quantities such as stellar masses and ages via SED fitting analysis (Elmegreen et al. 2007; Elmegreen & Elmegreen 2010). However, as the information is not linked to the galaxy ID other than the photometric redshifts of some tadpoles[*4], here we do not utilize it but do see the morphological information only.

4.2. Reclassification of the Galaxies in the Tadpole Catalog of Elmegreen et al. (2005)

We examine to reclassify the tadpole galaxies in the tadpole catalog of E05 into our classification presented in Section 3.8. under the same manner described in Section 3.6.; that is, reclassification is executed by using the several i_{775}-band images with different contrast for each tadpole galaxy. The aim of this reclassification is to construct a catalog of the GTGs, which are the tadpoles originated not by galaxy interactions and/or mergers.

Among the 95 tadpole galaxies in the tadpole catalog of E05, 62 galaxies are classified as interacting or merging galaxies; they have curved-tails, several components in the head, and/or two distinct tails extended in the opposite directions from the head. For the tadpole catalog of E05, the inclusion of the tadpoles having several components in the head seems to be a natural consequence of their definition of tadpoles, in which no criteria for the number of components in the head is adopted (see Section 1 of Elmegreen & Elmegreen 2010). We present the images of these galaxies in Figures 8. Their IDs are listed up in Table 1.

[*4] The IDs in the UDF catalog of the 12 tadpole galaxies whose photometric redshifts are explicitly provided in either Elmegreen et al. (2007) or Elmegreen & Elmegreen (2010) are the following: 285, 741, 2881, 3058, 3508, 3583, 3819, 4592, 5358, 8561, 8614, and 9548. All redshifts other than those of 285 ($z = 0.15$) and 3058 ($z = 0.26$) are $z = 1.5$–4.7. Note that there are 3 tadpoles whose photometric redshifts are provided in Elmegreen & Elmegreen (2010) but whose IDs are not listed in the E05 tadpole catalog: 3527 in their Figure 15, which is classified as double clump galaxy in E05, and 4518 and 4682 in their Figure 14, which are not listed at all in the whole E05 catalog.

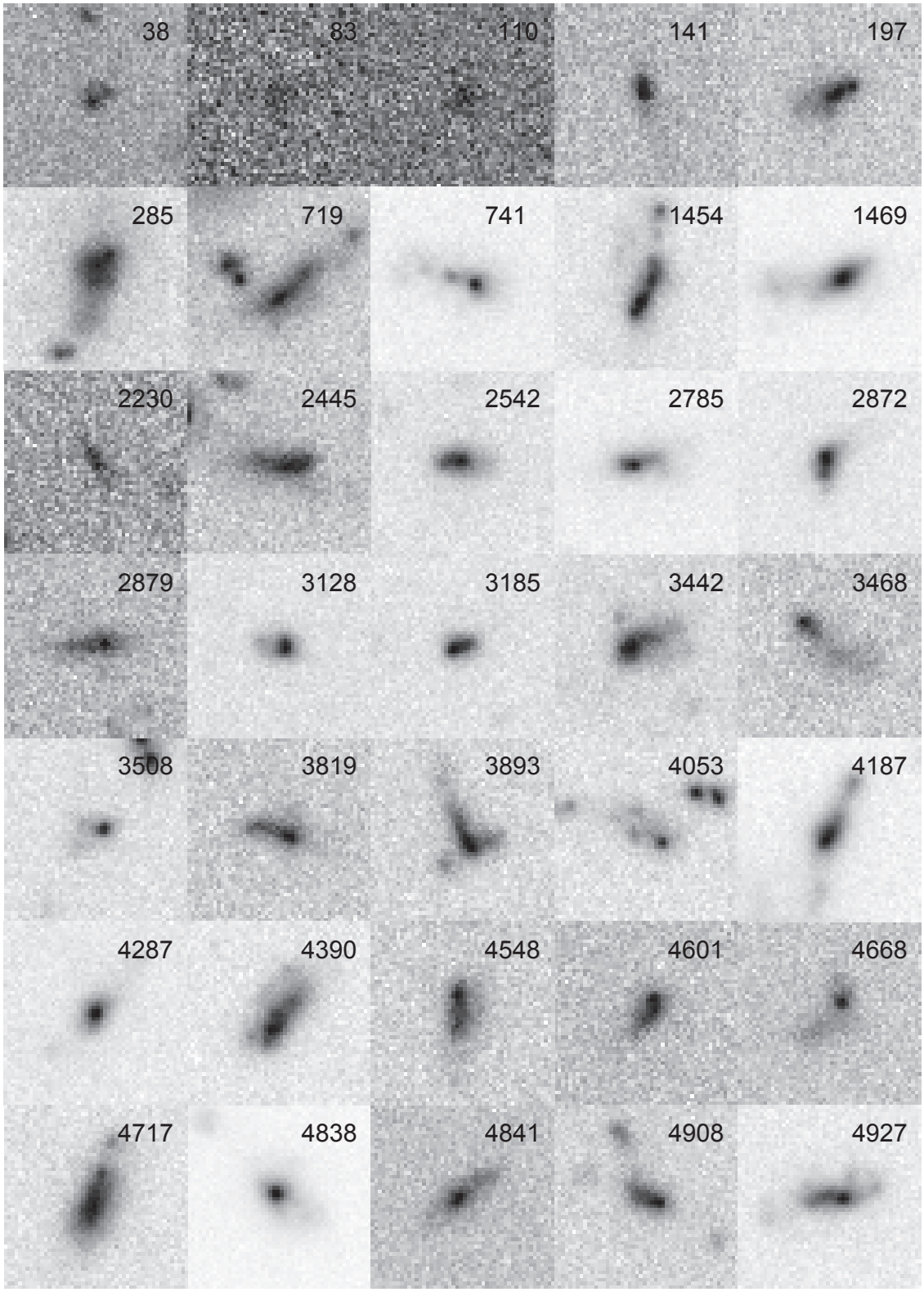

Fig. 8.— HST/ACS i_{775}-band images of the 62 galaxies showing a signature of galaxy interaction and/or merger taken from the tadpole galaxy catalog in the UDF given by E05. North is up and east is left. Image sizes are 1.5 arcsec × 1.5 arcsec. The label in each panel other than T1–7 is the object ID in the UDF catalog. T1–T7 are the object IDs which are not in the UDF catalog and found by E05.

Finally, we find 33 GTGs from the tadpole catalog in the UDF. Among the 33 GTGs, 10 and 23 are classified into class I and II, respectively. To date, they are the representative galaxies classified as GTGs. The images of all class I and II GTGs are presented in Figures 9 and 10, respectively. Their IDs are listed up in Table 2.

Our results of re-classification for the 95 tadpole galaxies in the UDF are summarized

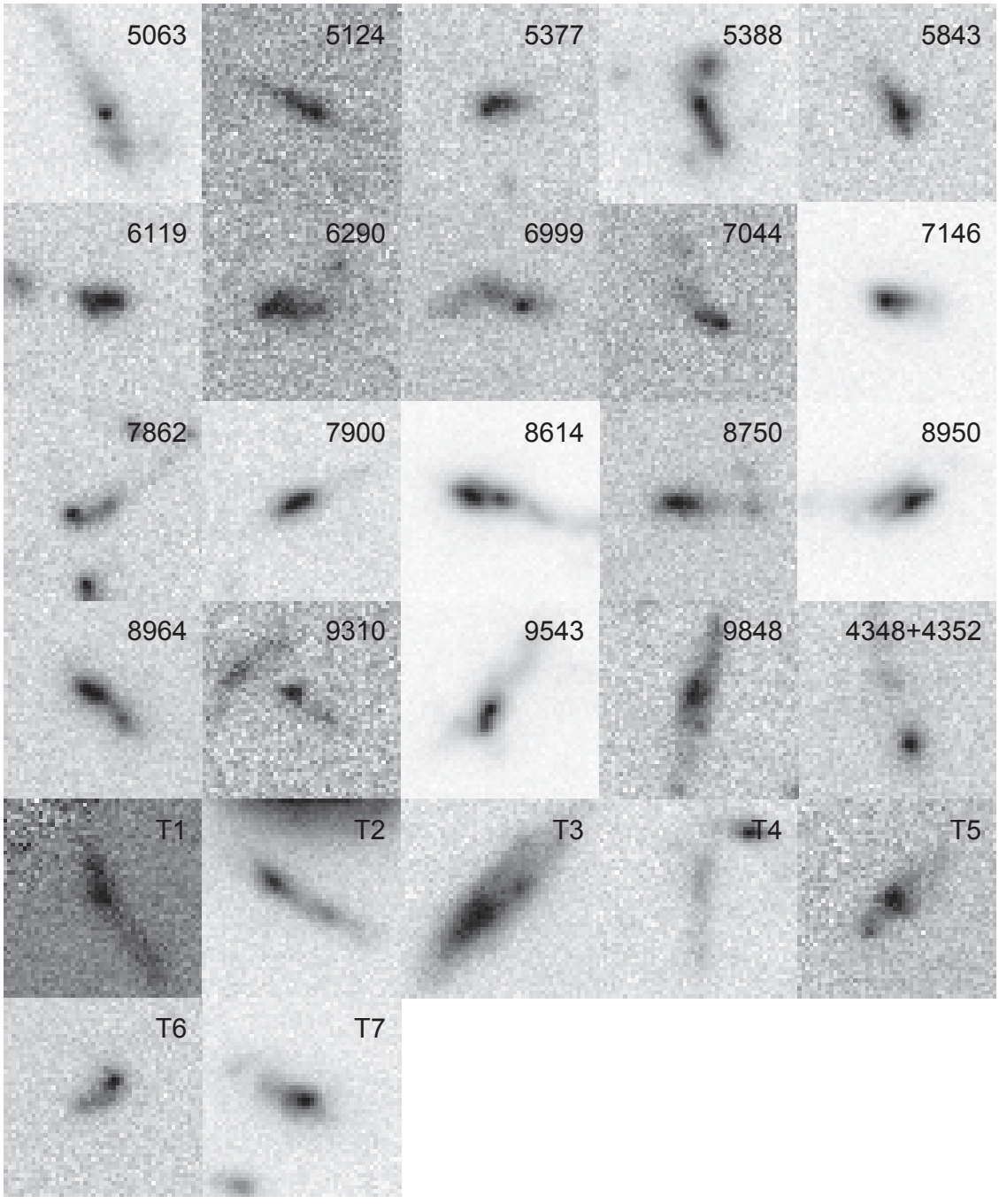

Fig. 8.— (Continued.)

in Table 3.

5. Origins of Genuine Tadpole Galaxies

As described in Section 3.8., the GTGs are in isolation by definition. In order to cause the tadpole structure for such galaxies, for which neither galaxy interaction nor merger is not expected, the following two processes are inevitably required: gas removal from a galaxy and subsequent star formation in the removed gas. The most probable physical

Table 1: Lists of 62 tadpole galaxies in the UDF classified as interacting/merging galaxies.

38	83	110	141	197	285	719	741	1454	1469
2230	2445	2542	2785	2872	2879	3128	3185	3442	3468
3508	3819	3893	4053	4187	4287	4390	4548	4601	4668
4717	4838	4841	4908	4927	5063	5124	5377	5388	5843
6119	6290	6999	7044	7146	7862	7900	8614	8750	8950
8964	9310	9543	9848	4348+4352	T1	T2	T3	T4	T5
T6	T7								

Note. — The numbers other than T1–T7 are the IDs in the UDF catalog. T1–T7 are tadpol which are not in the UDF catalog and found by E05.

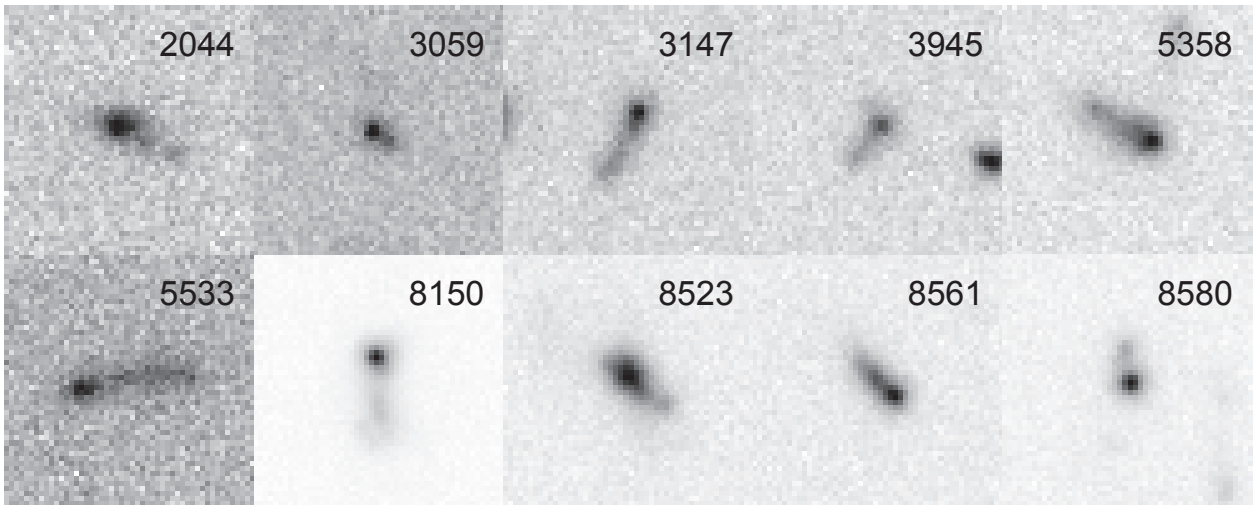

Fig. 9.— Same as Figure 8 but for the 10 class I GTGs.

process necessary to remove gas from a galaxy is considered to be ram pressure stripping. In this section, we give a quantitative estimate whether or not the ram pressure stripping occurs in high redshift GTGs (Sections 5.1. and 5.2.) and also provide a comment on the subsequent star formation in the removed gas (Section 5.3.).

5.1. Ram Pressure Stripping for GTGs

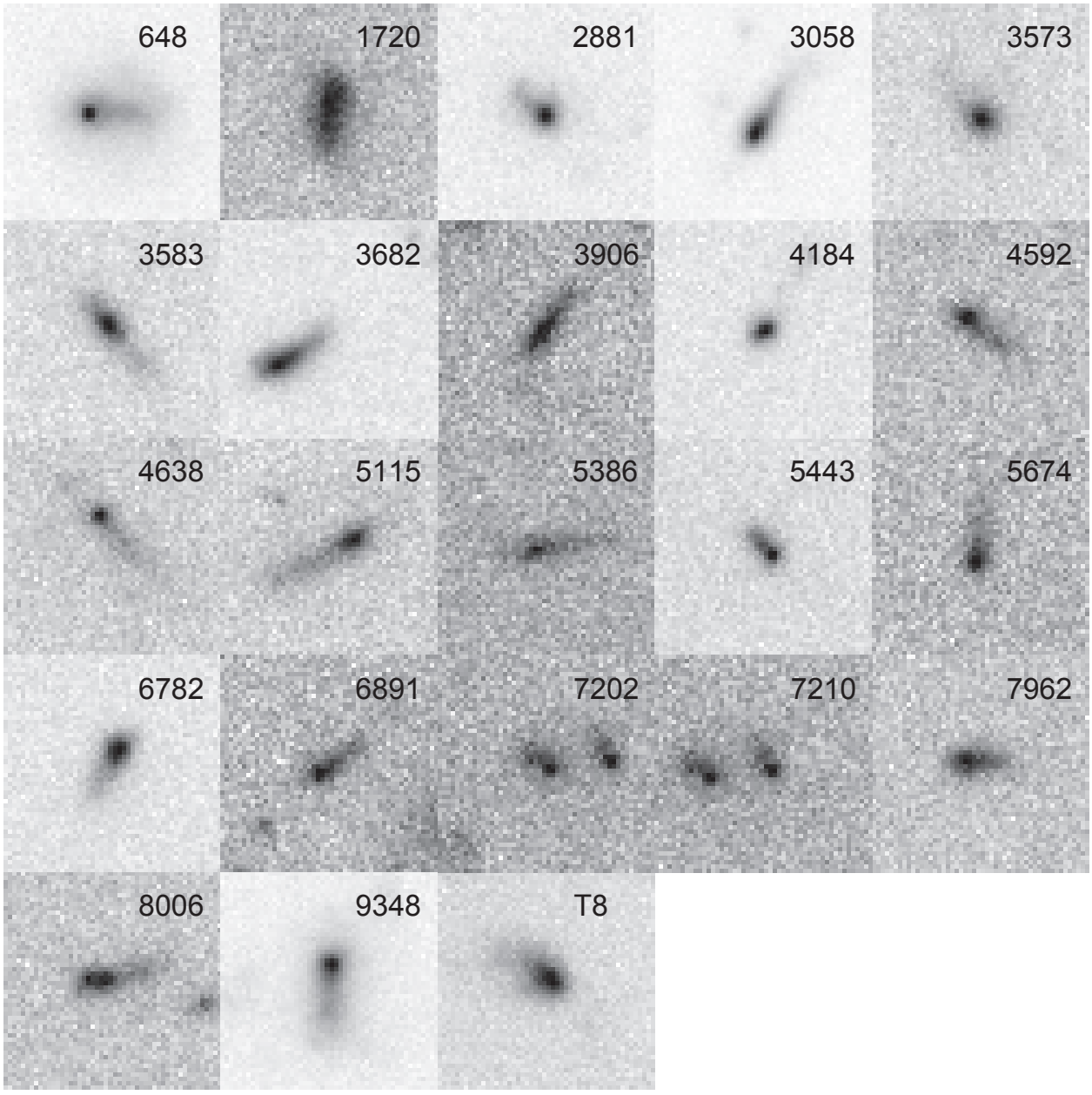

Fig. 10.— Same as Figure 8 but for the 23 class II GTGs.

The ram pressure stripping has already been suggested by Elmegreen & Elmegreen (2010) as a new formation mechanism of high-redshift tadpole galaxies. However, their discussion is not conclusive. Here, let us estimate quantitatively whether or not the ram pressure stripping occurs in high redshift GTGs in their environment for the first time via the so-called Gunn & Gott (1972) criterion,

$$P_{\rm ram} \geq 2\pi G\ \Sigma_{\rm star}\Sigma_{\rm gas}, \tag{3.1}$$

where $P_{\rm ram}$ is ram pressure, G is the gravitational constant, $\Sigma_{\rm star}$ and $\Sigma_{\rm gas}$ are the surface mass densities of stars and gas in a galaxy, respectively (see also, Domainko et al. 2006). The ram pressure is given by

$$P_{\rm ram} = \rho_{\rm IGM} v_{\rm rel}^2, \tag{3.2}$$

where $\rho_{\rm IGM}$ is the mass density of intergalactic matter (IGM) and $v_{\rm rel}$ is the relative velocity between the galaxy and IGM.

In order to estimate the ram pressure, we need fiducial values of both $\rho_{\rm IGM}$ and $v_{\rm rel}$.

Table 2: Lists of class I and class II GTGs.

A list of 10 Class I GTGs									
2044	3059	3147	3945	5358	5533	8150	8523	8561	8580
A list of 23 Class II GTGs									
648	1720	2881	3058	3573	3583	3682	3906	4184	4592
4638	5115	5386	5443	5674	6782	6891	7202	7210	7962
8006	9348	T8							

Note. — The numbers other than T8 are the IDs in the UDF catalog. T8 is a tadpole galax not in the UDF catalog and found by Elmegreen et al. (2005).

Table 3: Results of our classification of 95 tadpole galaxies in Elmegreen et al. (2005)

Our Classification	Number
(1) Interacting/merging galaxies	62
(2) Genuine Tadpole Galaxies (GTGs)	
(2-1) Class I: tail is detached from head	10
(2-2) Class II: tail is smoothly connected with head	23

According to equations (3.1) and (3.2), large $\rho_{\rm IGM}$ and $v_{\rm rel}$ are necessary conditions for the ram pressure stripping, here we consider a dense environment like galaxy cluster. The central mass density of intracluster gas (ICM) in the Coma cluster in the local universe is estimated as $\rho_0 = 6.3 \times 10^{-27}$ g cm^{-3} (Smith et al. 2013). If we consider a tadpole galaxy at $z = 2$, using this ρ_0, the IGM mass density is estimated to be $\rho_{\rm IGM} \simeq 1.7 \times 10^{-25}$ g cm^{-3} ($= 2.5 \times 10^6\ M_\odot$ kpc^{-3}) because the IGM density increases with increasing redshift as proportional to $(1+z)^3$. Adopting $v_{\rm rel} = 1000$ km s^{-1} as a fiducial value, which roughly corresponds to the halo circular velocity of the Coma cluster, we obtain

$$P_{\rm ram} \sim 1.7 \times 10^{-9} \left(\frac{\rho_{\rm IGM}}{1.7 \times 10^{-25}\ {\rm g\ cm^{-3}}} \right) \times \left(\frac{v_{\rm rel}}{1000\ {\rm km\ s^{-1}}} \right)^2 {\rm dyn\ cm^{-2}}. \quad (3.3)$$

Next, we estimate both $\Sigma_{\rm star}$ and $\Sigma_{\rm gas}$. Elmegreen & Elmegreen (2010) give a mean stellar-mass column density of the head region of tadpole galaxies in their sample is $\langle \Sigma_{\rm star} \rangle \sim 880\ M_\odot$ pc^{-2}, while its dispersions is significantly large: $\langle \Sigma_{\rm star} \rangle \sim 880 \pm 1800\ M_\odot$ pc^{-2}. Since the gas fraction in galaxies at $z \sim 2$ is ~ 0.5, the gas mass is comparable to the stellar mass, that is, $\Sigma_{\rm gas} \sim \Sigma_{\rm star}$ (e.g., Carilli & Walter 2013 and references therein). If we assume, as stripped gas typically lies at far from the center of the main body where stellar and gas densities are small, that the mass column densities of gas and star are smaller than the mean value by a factor of $C \sim 3$, we obtain $\Sigma_{\rm star} \sim \Sigma_{\rm gas} \sim 2.9 \times 10^2\ (C/3)^{-1}\ M_\odot$ pc^{-2}. Then, we obtain the value of the right hand side of equation (3.2) as

$$2\pi G\ \Sigma_{\rm star}\Sigma_{\rm gas} \sim 1.6 \times 10^{-9} \left(\frac{\Sigma_{\rm star}}{2.9 \times 10^2\ M_\odot\ {\rm pc^{-2}}} \right)^2 \times \left(\frac{C}{3} \right)^{-2} {\rm dyn\ cm^{-2}}. \quad (3.4)$$

Given the fiducial values adopted in the above order estimates, ram pressure stripping of cold gas from a galaxy seems likely to occur. Indeed, in the nearby clusters of galaxies such as the Virgo and Coma clusters, observational evidence for the ram pressure stripping from cluster spiral galaxies has been accumulated to date (e.g, Chung et al. 2009 and references therein). Therefore, the interstellar gas of the head region of tadpole galaxies

can be stripped via the ram pressure if they reside in such rare and massive halos.

5.2. Number Density of GTGs

Through the above estimates, we present the ram pressure stripping in dense environment can be a possible origin for the GTG in high-redshift universe. Is this scenario also consistent with the observed number density of the GTGs we selected from the E05 catalog?

In order to answer the question, we first estimate the expected number density of the formation sites of the GTGs. As there is no signature for clustering seen in the GTGs, our finding of 33 GTGs in the UDF field implies that the number density of their formation sites is $\sim 10^{-4}$ Mpc^{-3} at least (see Figure 6 of Elmegreen et al. 2007). Then we give an estimation for the number density of the dense environments where ram pressure stripping of gas is expected to occur. In the case that the relative velocity of $v_{\rm rel}$ corresponds to halo circular velocity $v_{\rm circ}$, the value adopted in the above estimation of $v_{\rm rel} = v_{\rm circ} = 1000$ km s^{-1} is translated into halo mass of $M_{\rm halo} = 1.2 \times 10^{14}\ M_\odot$ at $z = 2$. The cumulative number density of such massive halo is extremely rare at $z = 2$: $n(> M_{\rm halo}) \sim 10^{-6}$ Mpc^{-3}. Therefore, although $v_{\rm circ} = 1000$ km s^{-1} is similar one for the host halos of the Virgo and Coma clusters, the number density of such massive halo is much smaller than the expected number density of the formation sites of the GTGs.

This disagreement can be relaxed if we adopt $v_{\rm rel}/v_{\rm circ} \sim 2$ keeping $v_{\rm rel} = 1000$ km s^{-1} and $\rho_{\rm IGM} = 1.7 \times 10^{-25}$ g cm^{-3} unchanged; $v_{\rm rel} \gtrsim v_{\rm circ}$ is possible, for example, in the cases that a galaxy is orbiting in elliptical and/or parabolic orbits or that a galaxy is falling into a halo for the first time. In the case of $v_{\rm circ} \sim 500$ km s^{-1}, the corresponding halo mass and cumulative number density become $M_{\rm halo} = 1.5 \times 10^{13}\ M_\odot$ and $n(> M_{\rm halo}) \sim 10^{-4}$ Mpc^{-3}. The number density becomes comparable to the minimum one for the expected number densities.

Therefore, in order to explain the observed number density of the GTGs, another formation mechanism(s) is inevitably required. As a new formation mechanism of the GTG, we propose the "*cosmic-web stripping*", which is recently found in a cosmological

simulation (Benítez-Llambay et al. 2013). It removes gas from the galaxies across the collapsing cosmic-web via ram pressure during the large-scale structure forms. As the cosmic web will be expected to sweep a large volume, the number density of the formation sites of GTGs will high enough to explain the observed number density of the GTGs if the cosmic-web stripping acts as the origin of the GTGs. However, it is difficult to estimate whether or not the cosmic-web stripping is powerful enough to remove gas from the progenitors of the GTGs. This is because the simulation executed in Benítez-Llambay et al. (2013) is only for the Local Group and hence the velocity of the pancake is relatively small ($\sim$ 300 km s^{-1}). Nevertheless, as larger velocities are naturally expected in the formation sites of more massive halos, this cosmic-web stripping can be another formation mechanism than the ram-pressure stripping in dense environments.

5.3. Star Formation in the Stripped Gas

In order to cause the tadpole morphology, it is also necessary to form stars in the stripped gas because the tail in tadpole galaxies consists of stars based on their broad band imaging data. This requirement causes another difficulty to form the GTGs via ram-pressure and/or cosmic-web stripping. That is, more favored condition for star formation in the stripped gas is more disfavored one for stripping; denser gas is preferred and unfavorable for star formation and gas stripping, respectively. This can be represented by C used in the estimation of Section 5.1.. Larger value of C makes stripping gas via ram pressure easier but, at the same time, subsequent star formation in the stripped gas more difficult. Although it is unclear what is the appropriate value of C, some kind of fine-tuning seems to be required to meet both criteria. It is speculated that the trade-off between these requirements determines the emergence of the GTGs only at high-redshift universe.

However, such a new star formation in ram pressure stripped gas clouds are observationally found in galaxies in the Coma cluster (Yoshida et al. 2008, 2012; Yagi et al. 2010; Fumagalli et al. 2011; Kenney et al. 2013) and in clusters of galaxies (Yagi et al. 2013; see also Yamagami & Fujita 2011). It is therefore suggested that the ram-pressure and/or cosmic-web striping from galaxies at high redshift could occur, causing GTGs. If this is the case, such GTGs are new populations that are not identified in the local

universe. We can therefore identify them as probable candidates of GTGs.

5.4. Origins of Class I and II GTGs

In Section 3.8., we propose a classification for GTGs, that is, class I and II, according to their features in tails. Class I GTG has a separated tail from head, while class II GTG shows a smoothly-connected tail like a comet. They can be a same population with each other but seen from different viewing angle as already mentioned in Section 3.8.. In this case, all of the GTGs must have separated tail from the head because a smoothly-connected tail cannot be observed as a separated tail in any viewing angles. However, this interpretation conflicts with the observed numbers of classes I and II GTGs as follows.

First, let us assume that all GTGs have intrinsically detached tails from their heads. Then, the probability that a GTG is observed as either classes I or II can be determined by its viewing angle, as shown in Figure 9. That is, the number ratio between the classes I and II GTGs can be represented by a critical viewing angle, $\theta_{\rm crit}$, which is defined as

$$\theta_{\rm crit} \approx \arcsin\left(\frac{r_{\rm head}}{r_{\rm head}+r_{\rm det}}\right), \tag{3.5}$$

where $r_{\rm head}$ is the size of the head and $r_{\rm det}$ is the detached distance between the head and tail; if a GTG is viewed from $0^\circ < \theta < \theta_{\rm crit}$ or $90^\circ - \theta_{\rm crit} < \theta < 90^\circ$, it is observed as the class II GTG showing smoothly connected tail with the head. Therefore, the number ratio between the class II GTG and all GTGs is represented by

$$\frac{N_{\rm classII}}{N_{\rm GTG}} = \frac{N_{\rm classII}}{N_{\rm classI}+N_{\rm classII}} \approx 1-\cos\theta_{\rm crit}. \tag{3.6}$$

As a tail is observed to be detached from the head, $r_{\rm det} \gtrsim r_{\rm head}$ is expected. This is translated into $\theta_{\rm crit} \lesssim 30^\circ$ by its definition of eq. (3.5). Therefore, the number fraction of the class II GTGs among all GTGs should be less than $1-\cos 30^\circ \approx 0.13$ under this interpretation. However, as we identify 23 class II GTGs among 33 GTGs, the number fraction is $N_{\rm classII}/N_{\rm GTG} = 0.70 \pm 0.19$, which is significantly larger than the maximum number fraction in this interpretation. Note that, in the case of $r_{\rm det} \approx 0.05 r_{\rm head}$, $N_{\rm classII}/N_{\rm GTG} = 0.70$ is consistent with this interpretation. However, such small detached

distance is in conflict with the observational fact that the tail is detected to be detached from the head as described above. Moreover, if this interpretation could be correct, the tail lengths of the class II GTGs are expected to be shorter than those of the class I GTGs, also conflicting with the observed results. Therefore, we can conclude that (at least half of) the class II GTGs are intrinsically distinct population from the class I GTGs, which have different origins and/or evolutionary stages.

We note that, in the above estimation, the probability that a GTG is not observed as a tadpole galaxy (e.g., viewing angles of (a) or (e) shown in Figure 9) is implicitly assumed to be negligibly small. This is based on the observational fact that the tail lengths of the E05 tadpole galaxies are found to be much longer than their head sizes; a mean length of

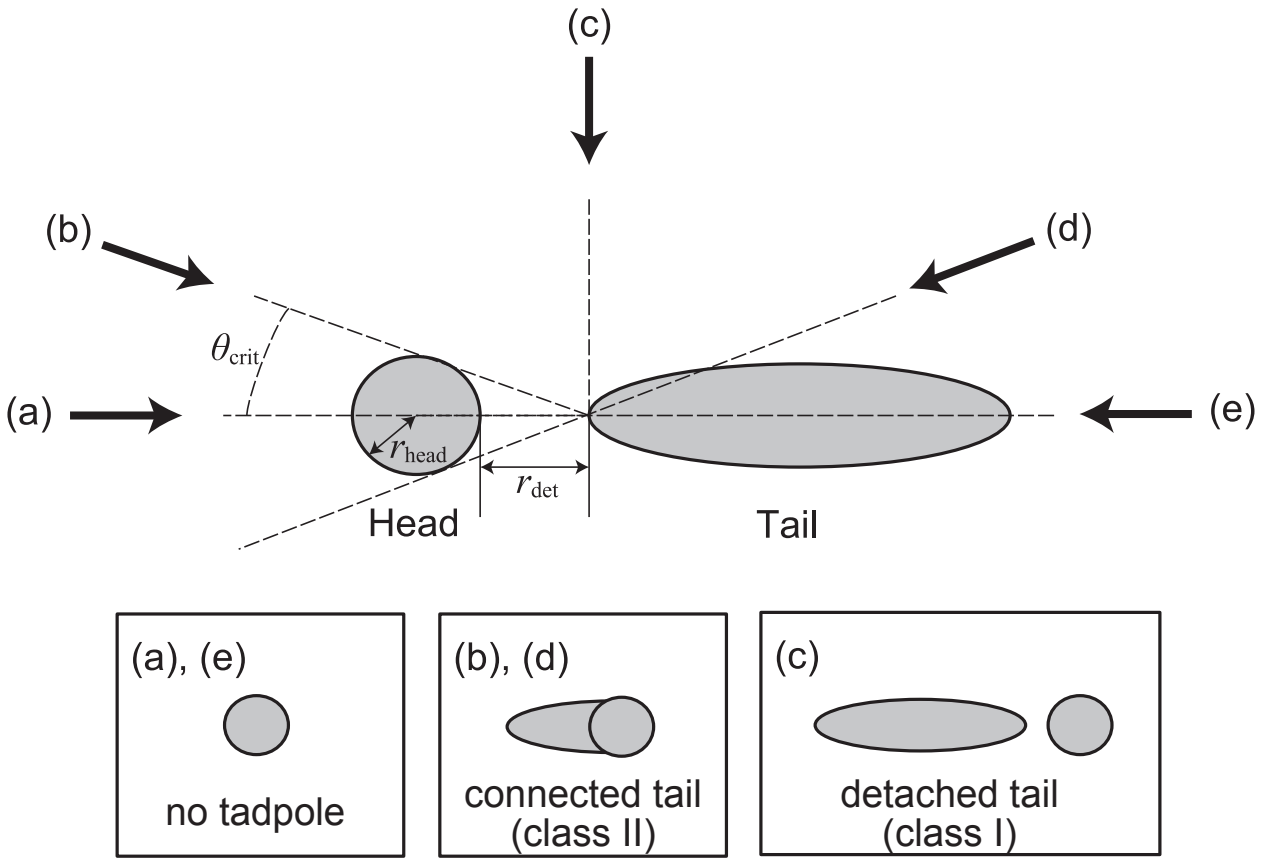

Fig. 11.— Schematic view of the dependence of the GTG morphology on the viewing angle. Here the GTG is assumed to have a detached tail intrinsically. The detached tail, which is characteristic feature for the class I GTG, is observed only if it is viewed from the angles between (b) and (d), like (c). The tail is observed to be connected with the head if it is viewed from the angles between (a) and (b) or (d) and (e). It is also possible that the GTG is not observed as a tadpole galaxy if it is viewed from the angles like (a) or (e).

tail of 3.9 ± 1.7 kpc is about 10 times larger than a mean size of head of 0.31 ± 0.36 kpc (see Figure 11 of Elmegreen & Elmegreen 2010). However, taking a realistic probability into account, the conclusion becomes more significant because the probability that a GTG is observed as a class II GTG decreases keeping that of class I GTG unchanged.

It is possible that a difference only in evolutionary stage can explain the morphological difference between the two classes of the GTGs. Even in the case that both classes I and II GTGs have the same origin of the ram-pressure and/or cosmic-web stripping, the tail morphology will be determined via a combination of the following quantities: the timescales of gas stripping and star formation in the stripped gas ($t_{\rm strip}$ and $t_{\rm sf}$), the velocity of the stripped gas ($v_{\rm gas}$), and the escape velocity from the gravitational potential well of the head ($v_{\rm esc}$). In the case of $t_{\rm strip} \sim t_{\rm sf}$ (i.e., star formation occurs during gas stripping proceeds), a GTG is born as a class II GTG. If $v_{\rm gas}$ is larger than $v_{\rm esc}$, the GTG will evolve into a class I GTG. In contrast to the case, a GTG will be formed as a class I GTG in the case of $t_{\rm strip} \ll t_{\rm sf}$ and evolve into a class II GTG if $v_{\rm gas} < v_{\rm esc}$. Numerical simulation will be required to predict which scenario is more realistic.

6. Conclusion

Our conclusions in this study are summarized below.

(1) We have clarified that there are several types of tadpole galaxies. In the local universe, a part of minor- and major mergers are identified as tadpole galaxies solely with their head-tail structures.

(2) As for high-redshift tadpole galaxies, we have found some tadpole galaxies without any signatures for galaxy interaction and/or merger. We call them as genuine tadpole galaxies (GTGs). We have also found that the GTG is a unique population in high-redshift universe.

(3) Then we have examined the possibility that the GTGs could be made by the ram-pressure stripping in dense IGM environments and/or cosmic-web stripping as large-scale structure forms. Our analysis suggest that such ram-pressure and/or

cosmic-web stripping can occur at high redshift.

(4) However, physical conditions of cold gas clouds in galaxies and the IGM at high redshift have not yet been investigated accurately. Future new observations will prove whether or not the ram-pressure driven formation of tadpole galaxies occurs. If this mechanism works efficiently at high redshift, a new insight will be obtained for the understanding early evolution of galaxies.

(5) It is finally mentioned that a half of the tadpole sample galaxies in E05 are not classified as tadpole galaxies in our new classification. On one hand, some well-defined tadpole galaxies are found in the catalog of chain galaxies in Elmegreen et al. (2005). This means that eye-ball classification is generally difficult, in particular for distant small galaxies. Computer-aided automatic classifiers will be necessary to classify such galaxies in future.

Chapter 4

GENUINE CHAIN GALAXIES IN HIGH REDSHIFT UNIVERSE

1. Abstract

In order to investigate the origin of chain galaxies at high redshift, we investigate the observational properties of chain, bent-chain, and the clump-cluster galaxies in the Hubble Ultra Deep Field, catalogued by Elmegreen et al. (2005). Since it appears that interacting/merging galaxies are also classified as the above three types of galaxies in previous studies, we have re-classified all the sample galaxies by ourselves and then obtained unambiguous samples of 36 chain, 11 bent-chain, and 68 clump-cluster galaxies. In order to secure the accuracy of photometric redshift, we use 21 chain, 7 bent-chain, and 60 clump-cluster galaxies that are brighter than $i_{775} = 26.5$ AB magnitude. Using the photometric data of CANDELS, we evaluate their photometric redshifts, V-band absolute magnitudes (M_V), and rest-frame $B-V$ colors. It is found that the distributions of M_V and rest-frame $B-V$ color between chain and clump-cluster galaxies cannot be distinguished from K-S statistical tests. If all chain galaxies were the edge-on counterpart of clump-cluster galaxies, chain galaxies would tend to be fainter and redder because of larger extinction. It is thus suggested that a part of chain galaxies are genuine chain galaxies that have a linear structure. Another line of evidence for such genuine chain galaxies is the presence of bent-chain galaxies that are chain galaxies with a curved

morphology. If these bent-chain galaxies are the edge-on counterpart of clump-cluster galaxies, they would have either "U"-shaped or "C"-shaped warping in their putative disk although we cannot rule out a possibility of the bending (or fire-hose) instability. Accordingly, we suggest that there present genuine chain galaxies with a linear or curved morphology at high redshift although they are considered to be rare because of their dynamically unstable property.

2. Introduction

Our nearby universe appears to be dominated regular-shaped galaxies such elliptical and disk galaxies. Therefore, the so-called Hubble sequence provides us a good guideline to investigate the formation and evolution of galaxies. Namely, one important goal is the understanding of the origin of Hubble sequence; when and how the Hubble sequence was established during the course of galaxy evolution from high redshift to the present day (e.g., Kajisawa & Yamada 2001; Conselice et al. 2005; Law et al. 2007).

For this purpose, it is essentially important to probe morphological properties of galaxies at high redshift. Since the Hubble Deep field project in 1995 (Williams et al. 1996), we have realized that there exist unusual populations of galaxies in the high-redshift universe. They are chain galaxies including bent-chain galaxies, and clump-cluster galaxies, (e.g., van den Bergh et al. 1996; Elmegreen et al. 2004a [hereafter EEH04]; Elmegreen & Elmegreen 2006b [hereafter EE06]). Their typical examples are shown in Figure 1.

However, it is still uncertain whether or not chain and clump-cluster galaxies are different populations. In fact, the discovery of clump-cluster galaxies led EEH04 to propose that these two populations are the same population but viewed from different lines of sight; i.e., chain galaxies are interpreted as edge-on counterparts of clump-cluster galaxies (EEH04). Since the majority of high-redshift galaxies show clumpy morphology, it is crucially important to understand the nature of clump-dominated galaxies in the young universe and explore their origin. For this purpose, we focus on the physical relationship between chain galaxies and clump-cluster galaxies.

In order to clarify what we know on such clump-dominated galaxies and what problems are remained now, we give a brief summary on both chain and clump-cluster galaxies at high redshift below.

2.1. Chain Galaxies

The population of chain galaxies was first identified in the HST WFPC2 imaging of the Hawaii Survey fields, SSA 13 and SSA 22, by Cowie et al. (1995). They suggested that chain galaxies are linearly organized giant star forming regions at $z \sim 0.5 - 3$. Since such linear structures are dynamically unstable, chain galaxies are considered to be in a forming phase of galaxies. Subsequently, chain galaxies are also found in the Hubble Deep Field (van den Bergh et al. 1996). A typical example is HDF 3-531. More later, Elmegreen et al. (2004b; hereafter EES04) identified 69 chain galaxies in the Tadpole Advanced Camera for Survey (ACS) Field.

Chain galaxies were once considered to be edge-on low-surface-brightness galaxies

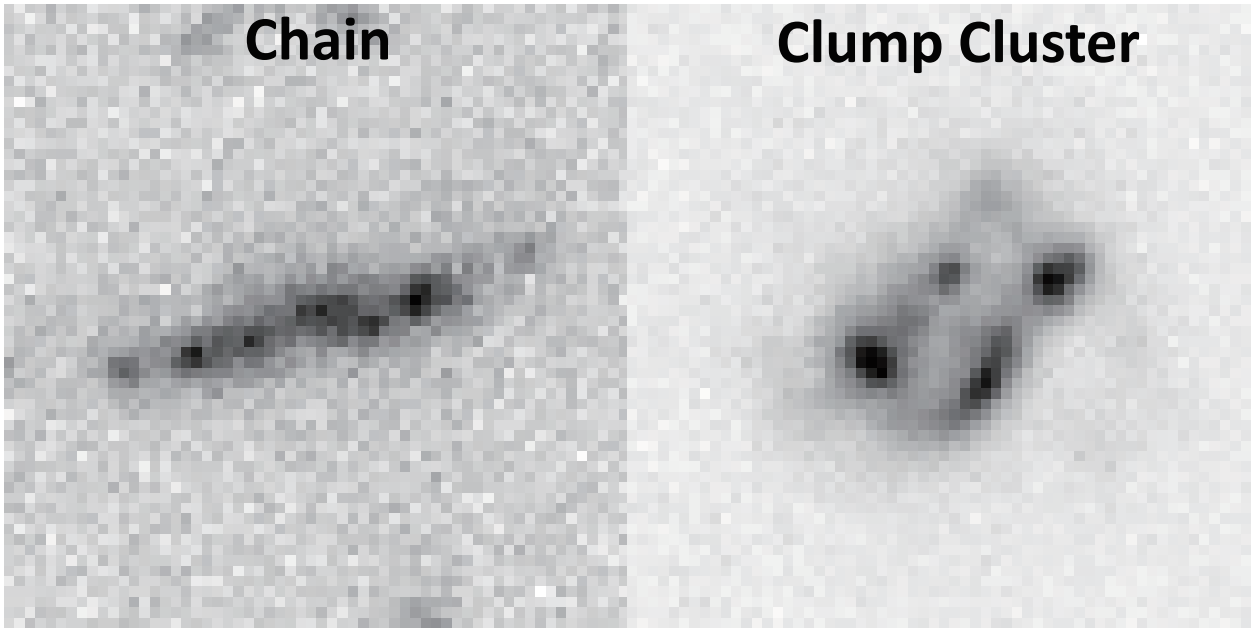

Fig. 1.— ACS i_{775}-band images of the chain galaxy (UDF 6478, left), and the clump-cluster galaxy (CC 12, right) in the Hubble Ultra Deep Field. Note that CC 12 is not included in the UDF catalog and found by Elmegreen et al. (2005). The Image size is 1.8 arcsec $\times$ 1.8 arcsec in each panel.

at low redshift (Dalcanton & Shectman 1996). However, it has turned out that most chain galaxies are located at intermediate and high redshift as originally suggested by Cowie et al. (1995). Unfortunately, most chain galaxies are too faint to be observed in spectroscopy even by using 8 – 10 m class telescopes. However, almost all chain galaxies are estimated to be located at $z > 0.5$ with the photometric redshift method (e.g., Elmegreen & Elmegreen 2005 [hereafter EE05]; EE06; Elmegreen & Elmegreen 2010; EES04; Elmegreen et al. 2007; Elmegreen et al. 2009a [hereafter E09a]; Elmegreen et al. 2009b [hereafter E09b]).

One probable formation mechanism for chain galaxies at high redshift has been proposed by Taniguchi & Shioya (2001; hereafter TY01). In their model, chain galaxies are formed through the gravitational instability in a dense gaseous sheet that could be made by interaction between two neutral gaseous shells driven by the superwind activity. Since, however, such one-dimensional structures are dynamically unstable, they have already evolved into dwarf elliptical galaxies in the present universe. Therefore, chain galaxies are observed only at high redshift. One of the original chain galaxies, HDF 4-455.1 (the Hot Dog galaxy) at $z = 2.803$ does not show any systematic rotational motion (Bunker et al. 2000). The TY01 model is naturally applicable to this type of chain galaxies.

Another possible interpretation is that chain galaxies are edge-on counterparts of clump-cluster galaxies that are also observed at similar redshifts (EEH04); see next subsection in detail. Since there present clump-cluster galaxies at high redshift, a part of high-redshift chain galaxies can be interpreted as their edge-on counterparts. However, this does not mean necessarily that all chain galaxies are such counterparts.

EE06 found a new population of chain galaxies in the course of their survey of ring galaxies in GEMS and GOODS fields. They are called as bent-chain galaxies because they show a curved chain morphology. In Figure 2, we show a couple of examples of bent chain galaxies. It appears that they cannot be interpreted as edge-on counterparts of clump-cluster galaxies because of their morphological properties. The presence of bent-chain galaxies also suggest that there present genuine chain galaxies with a linear or a curved morphology at high redshift.

2.2. Clump-Cluster Galaxies

Since the great success of the Hubble Deep Field (Williams et al. 1996), it has turned out that most high-redshift galaxies have peculiar or irregular morphology (e.g., Abraham et al. 1996; van den Bergh et al. 1996). Some of them are interacting or merging galaxies. However, the majority looks isolated galaxies with unusual morphology that cannot be seen at low redshift. For example, van den Bergh et al. (1996) suggest the presence of proto spiral and proto barred spiral galaxies all of which show clumpy structures around a nucleus (or a bulge).

Later, EEH04 found 87 clump-cluster galaxies together with 69 chain galaxies in the Tadpole ACS field (see also EES04). They pointed out the similarity in colors and apparent magnitudes of the brightest clumps in the clump-cluster and chain galaxies. They also pointed out the similarity between the distribution of axial ratios for the combined sample of the clump-cluster and chain galaxies and that for normal disk

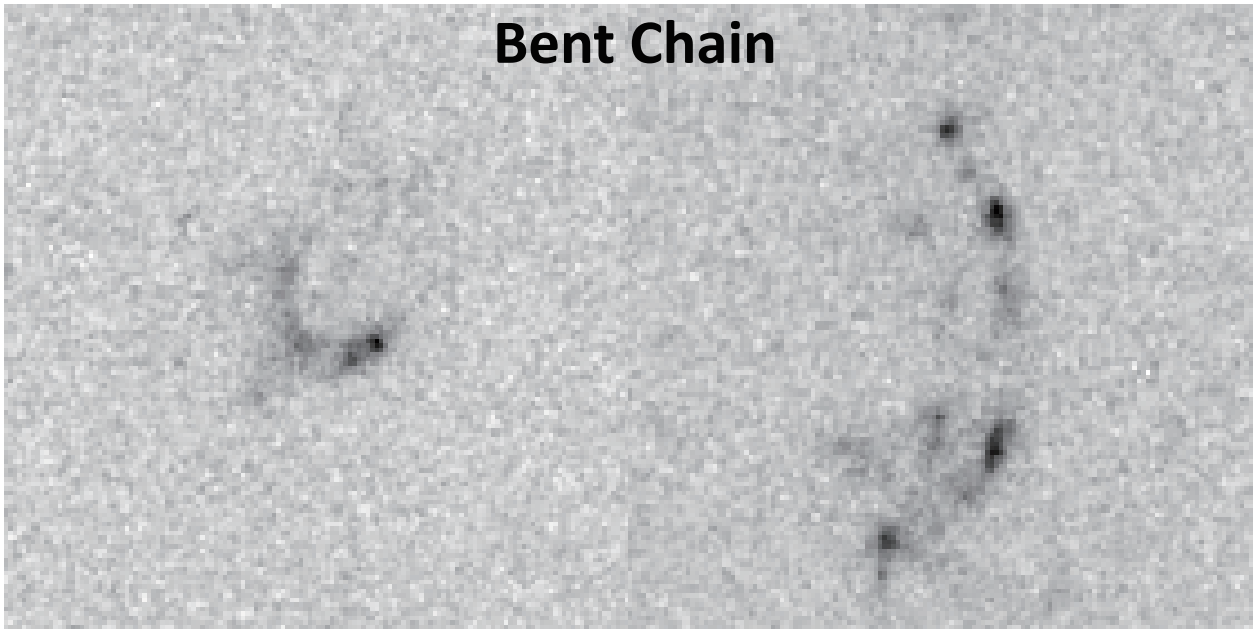

Fig. 2.— ACS V_{606}-band images of bent-chain galaxies in the GEMS field. The object IDs are COMBO-17 12329 (left) and COMBO-17 3618 (right). The image size is 4.2 arcsec × 4.2 arcsec in each panel.

galaxies. Based on these results, they proposed that chain galaxies may be edge-on counterparts of clump-cluster galaxies.

Young galaxies at high redshift tend to be gas-rich. Observationally, the cold gas fraction in galaxies at $z \sim 2$ reaches to ~ 50 percent (Carilli & Walter 2013). Since a gas-rich galactic disk is unstable for the gravitational instability, it is expected that the disk shows clumpy structures (Noguchi 1998; Agertz et al. 2009; Ceverino, Dekel, & Bournaud 2010). It is also expected that a multiple clump system in the disk evolves to make a bulge in the central region (Elmegreen et al. 2008; see also Genzel et al. 2008) although all galaxies may not always take this path.

3. Intrinsic Properties of Chain, Bent-Chain, and Clump-Cluster Galaxies

EEH04 proposed that clump-cluster galaxies are face-on counterparts of chain galaxies. This proposal is based on the similarity in apparent magnitudes and observed tcolors of the brightest clump between the clump-cluster and chain galaxies. EEH04 also noted that whole chain galaxies are fainter by ~ 1 mag than whole clump-cluster galaxies. They interpreted that this difference is attributed to larger extinction in the chain galaxies if they are edge-on counterparts of clump-cluster galaxies.

Here, we remind that both clump-cluster and chain galaxies are distributed in a wide range of redshift, e.g., from $z \sim 0$ to $z \sim 5$ (Elmegreen et al. 2007; E09a; E09b). Therefore, in order to examine their similarity or difference quantitatively, one has to compare their intrinsic physical properties. For this purpose, we make comparisons of the absolute V-band magnitude and the rest-frame $B - V$ color for the two samples with redshift information.

3.1. Sample Selection Procedures

In our analysis, we use the sample of 884 galaxies that are morphologically classified in Elmegreen et al. (2005; hereafter E05). Their detection procedure is briefly summarized here. They first selected all objects with a major axis greater than 10 pixels. Then, they classified their morphology based on the i_{775}-band images, brightness profiles, and contour maps (1σ contour level corresponds to a surface brightness of 25.5 mag arcsec^{-2}).

E05 classified all the galaxies into the following six categories: chain, clump-cluster, double, tadpole, spiral, and elliptical galaxies. However, we have found that a large number of galaxies appear to be either interacting or merging galaxies that cannot be classified into the six types given above. Such galaxies are contaminants in any comparative studies of chain and clump-cluster galaxies interested here. We also find that a number of the tadpole galaxies in E05 show chain-like morphology. Therefore, we have re-classified all the chain, clump-cluster, and tadpole galaxies in E05 by ourselves; note that 112 chain galaxies, 176 clump-cluster galaxies, and 95 tadpole galaxies. are catalogued in E05.

In our own morphological classification, we add the new category, bent-chain galaxies, since this type of galaxies are not simply considered as the edge-on counterparts of the clump-cluster galaxies (see §3.2). Using HST/ACS i_{775}-band images, three authors (KLT, YT, and YS) have classified all the sample galaxies in E05. If one or more authors did not classify a galaxy as either a chain, bent-chain, or clump-cluster galaxy, we omitted this galaxy in further discussion. This procedure is important to exclude any contaminants, providing us unambiguous samples of chain, bent-chain, and clump-cluster galaxies. We then have selected 36 chain galaxies, 11 bent-chain galaxies, and 68 clump-cluster galaxies. Details of the results of our classification and their relations to the E05 classification results are summarized in Table 1. As for the galaxies that are not classified as either, chain, bent-chain, or clump-cluster galaxies in our new classification are summarized in Appendix A1.

Our purpose here is to compare physical properties among the samples of chain, bent-chain, and clump-cluster galaxies. To perform this, we need redshift information on the sample galaxies. Since no spectroscopic redshift is available for any galaxies in our samples, we estimate their photometric redshifts. In order to obtain more reliable

Table 1: Summary of our classification

Our Classification	Classification in E05	Number of Galaxies
Chain Galaxies	Chain Galaxies	35
	Tadpole Galaxies	1
	Total	36
Bent-Chain Galaxies	Chain Galaxies	7
	Clump-Cluster Galaxies	2
	Tadpole Galaxies	2
	Total	11
Clump-Clusters Galaxies	Chain Galaxies	1
	Clump-Cluster Galaxies	66
	Tadpole Galaxies	1
	Total	68

photometric redshifts, we use the CANDELS photometric catalogue (Guo et al. 2013) because near infrared photometry is available as well as optical one.

To estimate the photometric redshift, we use the EAZY code (Brammer et al. 2008). All photometric data are taken from the CANDELS photometric catalog (Guo et al. 2013). After crossmatching our objects with those in the CANDELS catalog, our sample consists of 33 chain galaxies, 11 bent-chain galaxies, and 66 clump clusters. It appears that the number of clump-cluster galaxies decrease at $i_{775} \simeq 26.5$. Since this is due to the surface brightness limit in the sample selection by using the HUDF/ACS data, we use only galaxies with $i_{775} \leq 26.5$. Then, we obtain our final samples including 21 chain galaxies, 7 bent-chain galaxies, and 60 clump-cluster galaxies. We summarize the number of our sample in Table 2. The i_{775}-band images of our final samples are shown in Figures 3, 4, and 5 for the chain, bent-chain, and clump-cluster galaxies, respectively. As for our sample galaxies with $i_{775} > 26.5$ and no CANDELS data, we show their images in Appendix A2 for readers' convenience.

Using the photometric redshift and the spectral energy distribution (SED) of the best-fit template, we estimate the rest-frame V-band absolute magnitude (M_V) and the rest-frame $B-V$ color for all our final samples. We summarize the basic data of our final samples in Tables 3, 4, and 5. It is noted that the error of M_V corresponds to that of the photometric redshift.

Table 2: A summary of our samples of chain, bent-chain, and clump-cluster galaxies

i_{775} in the CANDELS catalog	Chain	Bent-Chain	Clump-Cluster
$i_{775} \leq 26.5$ (Final Sample)	21	7	60
$i_{775} > 26.5$	11	4	6
no data	4	0	2
Total	36	11	68

Table 3: Summary of basic properties of the chain galaxies with $i_{775} \leq 26.5$

ID		$z_{\rm ph}$	M_V	$B-V$[a]
UDF	CANDELS		(mag)	
401	9945	$4.43^{+0.06}_{-0.09}$	$-21.46^{+0.03}_{-0.02}$	0.02
521	10084	$0.97^{+0.04}_{-0.12}$	$-18.57^{+0.29}_{-0.08}$	0.19
666	10234	$1.15^{+0.04}_{-0.06}$	$-18.56^{+0.11}_{-0.07}$	0.10
741	10316	$3.23^{+0.10}_{-0.10}$	$-22.02^{+0.05}_{-0.05}$	0.21
1428	11077	$0.01^{+1.17}_{+0.71}$	$-8.21^{-9.86}_{-10.53}$	0.07
2265	11619	$0.03^{+0.05}_{-0.01}$	$-8.83^{+1.24}_{-2.24}$	0.27
3143	12189	$1.05^{+0.05}_{-0.06}$	$-19.18^{+0.13}_{-0.11}$	0.16
3299	12483	$1.09^{+0.07}_{-0.05}$	$-19.30^{+0.09}_{-0.14}$	0.18
4243	12950	$1.71^{+0.05}_{-0.10}$	$-19.61^{+0.12}_{-0.05}$	0.02
6391	14221	$1.33^{+0.09}_{-0.07}$	$-18.25^{+0.11}_{-0.14}$	0.11
6478	14309	$3.11^{+0.05}_{-0.09}$	$-21.26^{+0.05}_{-0.03}$	0.13
7037	15015	$1.84^{+0.10}_{-0.08}$	$-21.20^{+0.08}_{-0.11}$	0.24
7269	15205	$0.69^{+0.08}_{-0.05}$	$-19.26^{+0.18}_{-0.23}$	0.23
8624	15735	$0.83^{+0.05}_{-0.08}$	$-18.35^{+0.23}_{-0.12}$	0.21
8372	16097	$0.53^{+0.05}_{-0.06}$	$-19.42^{+0.26}_{-0.21}$	0.26
7737	16664	$0.56^{+0.05}_{-0.06}$	$-18.37^{+0.26}_{-0.20}$	0.21
9676	17375	$3.07^{+0.06}_{-0.08}$	$-20.67^{+0.05}_{-0.03}$	0.13
9839	17926	$2.33^{+0.08}_{-0.06}$	$-20.81^{+0.05}_{-0.07}$	0.10
9974	18064	$0.99^{+0.04}_{-0.10}$	$-19.05^{+0.22}_{-0.09}$	0.14
C7	13174	$3.72^{+0.10}_{-0.11}$	$-20.95^{+0.05}_{-0.05}$	0.08
C5	15783	$1.26^{+0.07}_{-0.07}$	$-18.20^{+0.12}_{-0.11}$	0.12

Note. — (a) Rest-frame $B-V$.

3.2. The Difference of Absolute Magnitudes

We show the rest-frame V-band absolute magnitude (M_V) of our final sample as a function of photometric redshift ($z_{\rm ph}$) in panel (a) of Figure 6. Two chain galaxies (UDF 1428 and UDF 2265) and three clump-cluster galaxies (UDF 1681, UDF 5634 and UDF 5768) are outside of this figure. because they are fainter than $M_V = -11$; note that all these galaxies are nearby ones at $z_{\rm ph} \leq 0.04$.

First, we comment on the redshift range of our sample galaxies. Although the two chain galaxies (UDF 1428, UDF 2265) and the six clump-cluster galaxies (UDF 1681, UDF 5634, UDF 5748, UDF 5501, UDF 6133, CC4) are located at $z_{\rm ph} < 0.5$, more than 90% (81/89) of our final sample exist at $0.5 < z_{\rm ph} < 4.5$; only one chain galaxy (UDF 401) is located at $z_{\rm ph} > 4$.

Now, let us compare the absolute V band magnitude distributions among the chain, bent-chain, and clump-cluster galaxies in our final samples. Our results are shown in Figure 6. In order to examine whether or not the M_V distributions are the same among the samples, we apply a Kolmogorov-Smirnov (K-S) test. This statistical test gives the probability that two concerned samples arise from the same distribution function,

Table 4: Summary of basic properties of the bent-chain galaxies with $i_{775} \leq 26.5$

ID		$z_{\rm ph}$	M_V	$B-V$[a]
UDFCANDELS			(mag)	
1375	11267	$0.63^{+0.06}_{-0.05}$	$-19.44^{+0.17}_{-0.21}$	0.18
1383	10995	$3.23^{+0.08}_{-0.09}$	$-20.26^{+0.05}_{-0.04}$	0.08
4010	12702	$3.54^{+0.07}_{-0.09}$	$-21.73^{+0.05}_{-0.03}$	0.19
3977	12997	$1.03^{+0.05}_{-0.07}$	$-20.50^{+0.15}_{-0.10}$	0.17
7617	16482	$2.99^{+0.06}_{-0.08}$	$-20.33^{+0.05}_{-0.04}$	0.09
1454	11173	$2.57^{+0.07}_{-0.05}$	$-20.41^{+0.04}_{-0.05}$	0.02
6999	14652	$2.95^{+0.08}_{-0.09}$	$-20.05^{+0.05}_{-0.05}$	0.13

Note. — (a) Rest-frame $B-V$.

Table 5: Summary of basic properties of the clump-cluster galaxies with $i_{775} \leq 26.5$

ID		$z_{\rm ph}$	M_V	$B-V$[a]
UDF	CANDELS		(mag)	
126	9527	$1.81^{+0.07}_{-0.17}$	$-21.29^{+0.20}_{-0.08}$	0.41
1681	11227	$0.04^{+1.64}_{-0.02}$	$-10.61^{+1.46}_{-8.18}$	0.02
1666	11561	$1.22^{+0.06}_{-0.04}$	$-20.68^{+0.08}_{-0.10}$	0.10
2012	11597	$2.87^{+0.05}_{-0.06}$	$-22.51^{+0.04}_{-0.03}$	0.17
2291	11702	$3.27^{+0.09}_{-0.08}$	$-20.18^{+0.04}_{-0.05}$	0.02
2340	11719	$1.20^{+0.07}_{-0.08}$	$-18.42^{+0.15}_{-0.13}$	0.14
2350	11730	$2.87^{+0.06}_{-0.09}$	$-20.20^{+0.06}_{-0.04}$	0.10
3745	12632	$1.33^{+0.07}_{-0.09}$	$-19.54^{+0.15}_{-0.11}$	0.14
3778	12668	$3.23^{+0.06}_{-0.09}$	$-21.81^{+0.05}_{-0.03}$	0.17
3752	12855	$1.55^{+0.10}_{-0.08}$	$-20.69^{+0.11}_{-0.12}$	0.18
3844	12893	$2.08^{+0.08}_{-0.07}$	$-21.67^{+0.07}_{-0.08}$	0.18
4053	12688	$3.11^{+0.09}_{-0.10}$	$-19.86^{+0.06}_{-0.05}$	0.05
5107	13384	$3.54^{+0.05}_{-0.11}$	$-19.72^{+0.06}_{-0.03}$	0.02
4860	13396	$3.49^{+0.08}_{-0.06}$	$-21.11^{+0.03}_{-0.04}$	0.08
5634	13686	$0.01^{+0.49}_{+0.02}$	$-6.42^{-2.47}_{-8.66}$	0.27
5190	13859	$1.22^{+0.05}_{-0.06}$	$-20.99^{+0.11}_{-0.09}$	0.18
5620	13953	$0.17^{+0.04}_{-0.04}$	$-16.01^{+0.67}_{-0.47}$	0.09
5748	13969	$0.02^{+0.07}_{-0.00}$	$-9.66^{+0.35}_{-3.42}$	0.15
5878	14040	$1.87^{+0.14}_{-0.09}$	$-20.93^{+0.10}_{-0.14}$	0.17
5501	14042	$0.12^{+1.59}_{-0.04}$	$-14.62^{+0.80}_{-5.91}$	0.27
5685	14057	$0.60^{+0.05}_{-0.08}$	$-17.82^{+0.33}_{-0.19}$	0.15
6056	14118	$0.52^{+0.17}_{-0.44}$	$-16.69^{+4.30}_{-0.63}$	0.06
6133	14163	$0.10^{+0.03}_{-0.05}$	$-14.29^{+1.59}_{-0.56}$	0.14
5827	14263	$1.71^{+0.12}_{-0.13}$	$-21.94^{+0.15}_{-0.13}$	0.31
6486	14356	$2.43^{+0.07}_{-2.32}$	$-19.41^{+6.71}_{-0.05}$	0.02
6438	14456	$2.17^{+0.13}_{-0.08}$	$-20.81^{+0.07}_{-0.11}$	0.14
6499	14479	$1.50^{+0.15}_{-0.06}$	$-19.20^{+0.09}_{-0.19}$	0.16
6837	14501	$2.65^{+0.10}_{-0.12}$	$-20.21^{+0.08}_{-0.07}$	0.13
6645	14529	$1.33^{+0.05}_{-0.11}$	$-19.22^{+0.18}_{-0.07}$	0.14
6394	14533	$1.52^{+0.10}_{-0.07}$	$-20.57^{+0.10}_{-0.13}$	0.19
6939	14713	$1.01^{+0.04}_{-0.14}$	$-18.60^{+0.32}_{-0.09}$	0.10
7185	14852	$0.87^{+0.05}_{-0.08}$	$-17.01^{+0.22}_{-0.13}$	0.13
6821	14867	$1.07^{+0.06}_{-0.04}$	$-20.64^{+0.08}_{-0.12}$	0.16
6785	14871	$1.20^{+0.05}_{-0.05}$	$-21.15^{+0.10}_{-0.08}$	0.21
7230	14975	$2.33^{+0.04}_{-0.11}$	$-20.48^{+0.09}_{-0.03}$	0.11
7526	15293	$1.84^{+0.18}_{-0.05}$	$-20.97^{+0.06}_{-0.18}$	0.12
7905	15429	$0.95^{+0.05}_{-0.08}$	$-18.79^{+0.19}_{-0.11}$	0.11
8859	15485	$2.95^{+0.05}_{-0.09}$	$-20.95^{+0.06}_{-0.03}$	0.12
8880	15518	$1.45^{+0.09}_{-0.05}$	$-20.80^{+0.07}_{-0.12}$	0.40
9159	15565	$1.84^{+0.08}_{-0.11}$	$-21.45^{+0.12}_{-0.09}$	0.22
8765	15582	$1.35^{+0.07}_{-0.09}$	$-19.73^{+0.15}_{-0.10}$	0.11
8125	15704	$1.05^{+0.05}_{-0.06}$	$-20.45^{+0.14}_{-0.10}$	0.12
8749	15775	$1.01^{+0.04}_{-0.06}$	$-21.07^{+0.13}_{-0.09}$	0.44
8217	16082	$2.76^{+0.11}_{-0.11}$	$-21.97^{+0.08}_{-0.07}$	0.24
8022	16207	$3.49^{+0.11}_{-0.08}$	$-21.24^{+0.04}_{-0.05}$	0.17
7995	16412	$1.22^{+0.05}_{-0.07}$	$-21.69^{+0.13}_{-0.08}$	0.25
7756	16466	$1.40^{+0.07}_{-0.06}$	$-20.07^{+0.08}_{-0.11}$	0.29
7678	16503	$0.73^{+0.15}_{-0.03}$	$-18.23^{+0.10}_{-0.41}$	0.15
7725	16548	$1.24^{+0.05}_{-0.07}$	$-21.12^{+0.13}_{-0.08}$	0.24
7559	16719	$0.97^{+0.05}_{-0.08}$	$-20.97^{+0.19}_{-0.10}$	0.22
9299	16827	$3.03^{+0.05}_{-0.05}$	$-20.89^{+0.03}_{-0.03}$	0.02
9273	16849	$1.01^{+0.06}_{-0.07}$	$-18.52^{+0.17}_{-0.13}$	0.09
9356	17049	$0.97^{+0.04}_{-0.15}$	$-17.96^{+0.35}_{-0.08}$	0.14
9474	17185	$1.03^{+0.05}_{-0.06}$	$-19.60^{+0.13}_{-0.10}$	0.21
9396	17227	$2.08^{+0.08}_{-0.11}$	$-20.60^{+0.10}_{-0.07}$	0.09
6153	14295	$1.20^{+0.05}_{-0.06}$	$-18.92^{+0.11}_{-0.09}$	0.09
CC3	10440	$0.71^{+0.14}_{-0.03}$	$-16.98^{+0.09}_{-0.38}$	0.06
CC4	13571	$0.08^{+0.03}_{-0.05}$	$-15.65^{+1.78}_{-0.66}$	0.15
CC6	14213	$2.83^{+0.07}_{-0.08}$	$-20.40^{+0.06}_{-0.04}$	0.12
CC12	17824	$1.40^{+0.08}_{-0.06}$	$-21.90^{+0.08}_{-0.11}$	0.30

Note (a) Rest-frame $B-V$.

comparing their cumulative distributions. First, for the chain and the clump-cluster samples, we show their cumulative distributions of M_V in panel (b) of Figure 6. Applying the K-S test, we obtain the probability of $p = 0.136$. Therefore, we do not find any statistically significant difference between them. Second, for the clump-cluster sample and the combined sample (chain + bent-chain), we show their cumulative distributions of M_V in panel (c) of Figure 6. Applying the K-S test, we obtain the probability of $p = 0.641$.

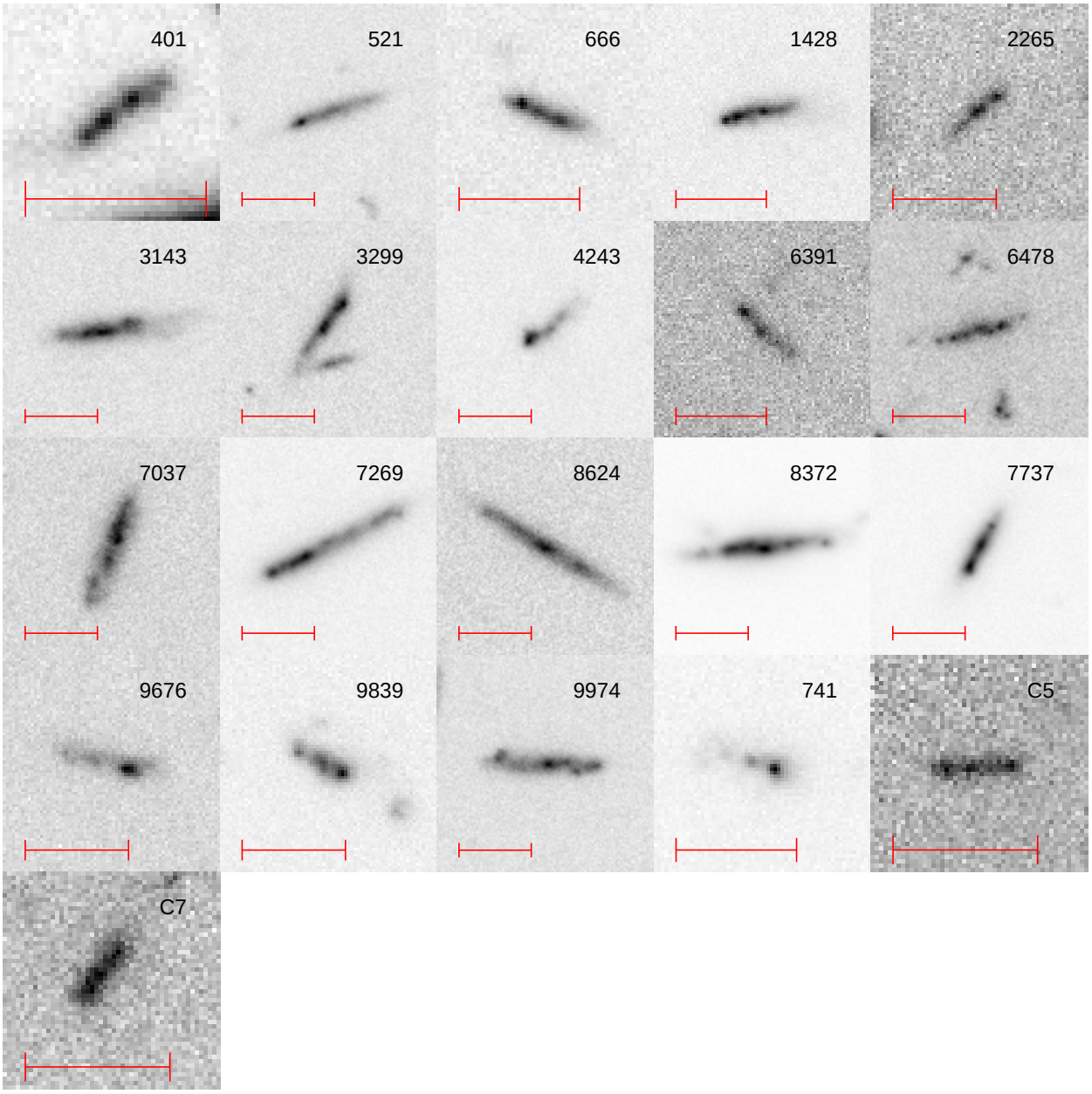

Fig. 3.— ACS i_{775}-band images of the chain galaxies with $i_{775} \leq 26.5$ (see Table 3). North is up and east is left. A red line in each panel shows 1 arcsec. The label in each panel except C7 is the object ID in the UDF catalog. Note that C7 is the object ID in E05.

Again, we do not find any statistically significant difference between them. Finally, for the chain and bent-chain samples, we show their cumulative distributions of M_V in panel (d) of Figure 6. Applying the K-S test, we obtain the probability of $p = 0.013$. Again, we do not find any statistically significant difference between them. If we adopt the significance level of 95%, we reject the null hypothesis that the two distributions are the same. This result is attributed to that most bent-chain galaxies are brighter than $M_V = -20$ while the chain sample contains a number of faint galaxies between $M_V = -18$ and $M_V = -20$.

In addition to the difference between the chain and bent-chain samples shown above, we also find a significant difference between the chain and clump-cluster subsamples at $z_{\rm ph} \leq 1.7$; see panel (a) of Figure 6. It is shown that all the chain galaxies are fainter than $M_V = -20$ while the clump-cluster galaxies are distributed in a wide range of M_V up to -22. On one hand, at $z_{\rm ph} > 1.7$, the three types of galaxies show little difference in the distribution of M_V. In order to study these properties quantitatively, we show cumulative distribution functions of M_V for the chain, bent-chain, clump-cluster, and the combined sample (chain + bent-chain) in Figure 7. Applying the K-S test between the chain and clump-cluster galaxy samples, we obtain the probability of 0.723 and 0.023 for $z_{\rm ph} > 1.7$ and $z_{\rm ph} < 1.7$, respectively. Adopting the significance level of 95%, the difference of M_V distributions between the two samples is considered to be real, implying that all chain

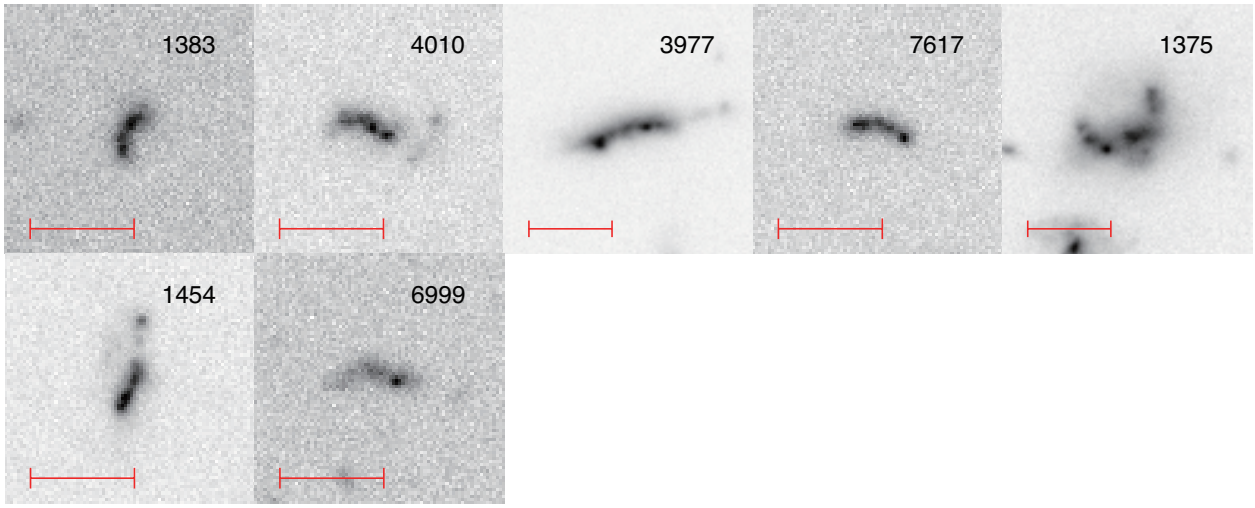

Fig. 4.— ACS i_{775}-band images of the bent-chain galaxies with $i_{775} \leq 26.5$ (see Table 4). North is up and east is left. A red line in each panel shows 1 arcsec. The label in each panel is the object ID in the UDF catalog.

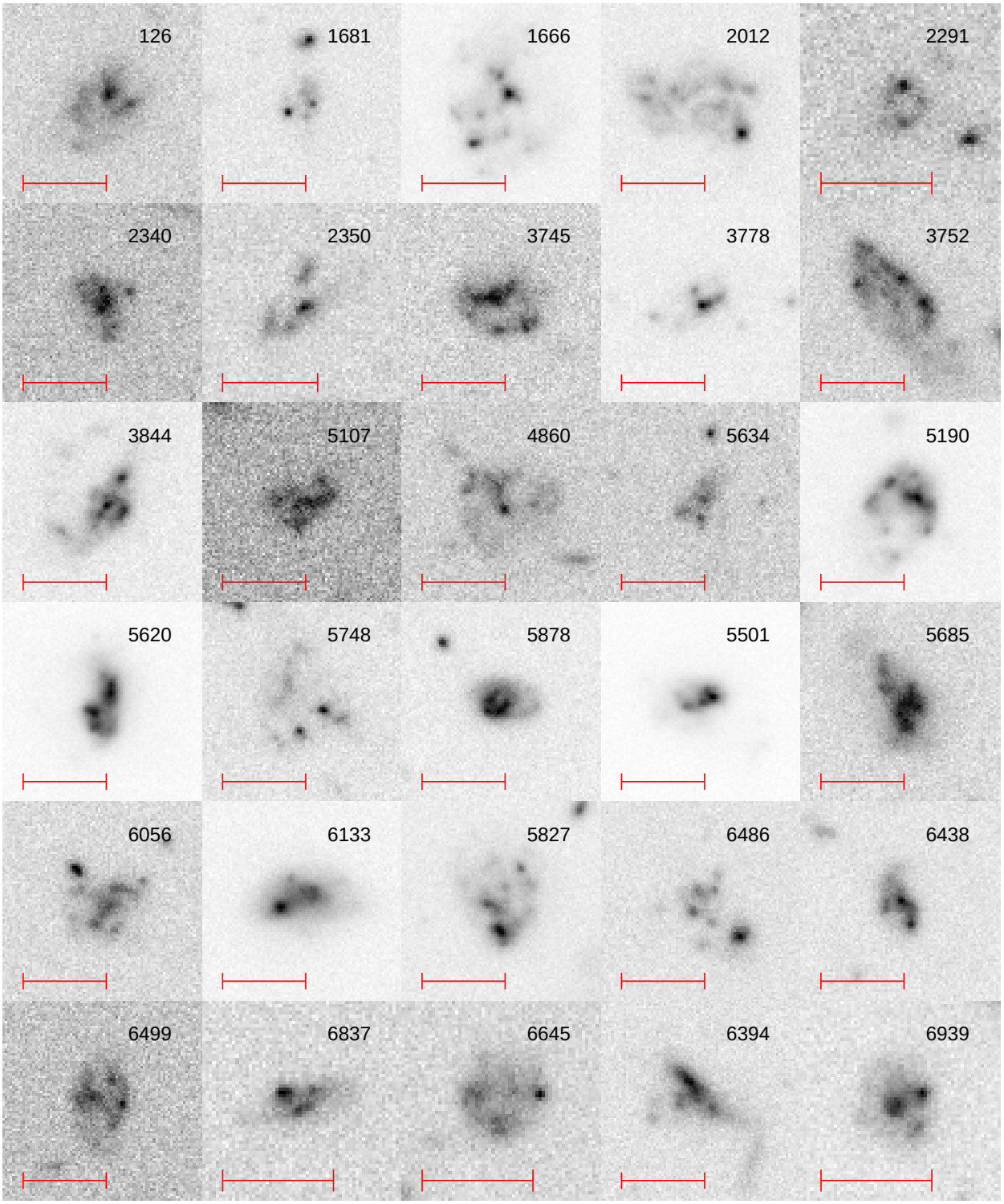

Fig. 5.— ACS i_{775}-band images of the clump-cluster galaxies with $i_{775} \leq 26.5$ (see Table 5). North is up and east is left. A red line in each panel shows 1 arcsec. The label in each panel is the object ID in the UDF catalog.

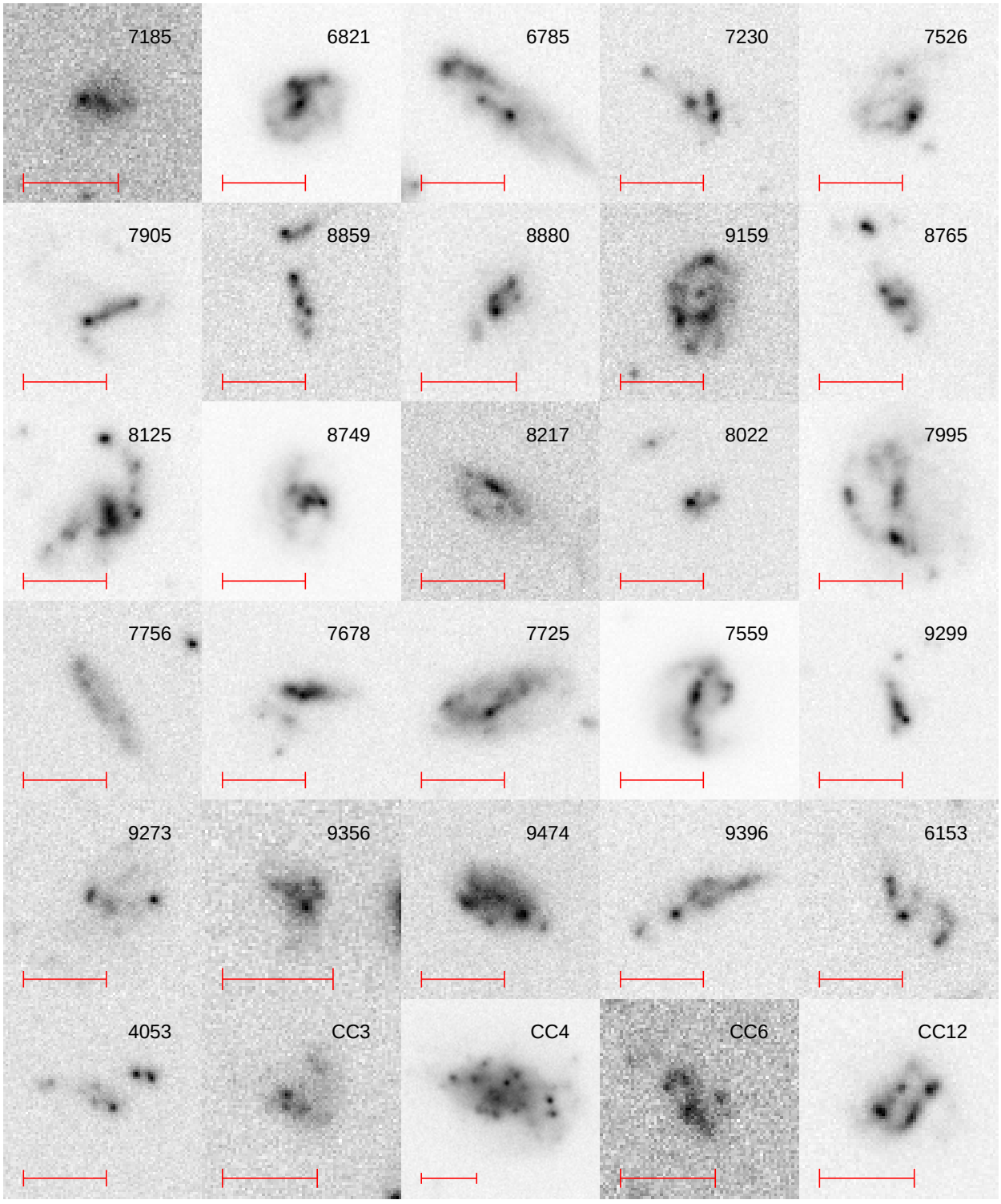

Fig. 5.— (Continued.)

galaxies are not the edge-on counterpart of clump-cluster galaxies. Since, however, the samples are not large enough to obtain a more convincing result, future investigations will be necessary with much larger samples. Finally, we note that there may be a possible effect of the so-called morphological K-correction because the ACS i_{775}-band imaging probes rest-frame near UV (shorter than 3000Å) for galaxies at $z_{\rm ph} > 1.7$ while optical for galaxies at $z_{\rm ph} < 1.7$. This point is also recommend to be taken into account in future studies.

3.3. The Difference of Rest-Frame Optical Color

Next, we compare the rest-frame $B - V$ color distributions between the chain and clump-cluster samples. We show the rest-frame $B - V$ color of our samples as a function of photometric redshift in the left panel of Figure 8. For comparison, we also show the

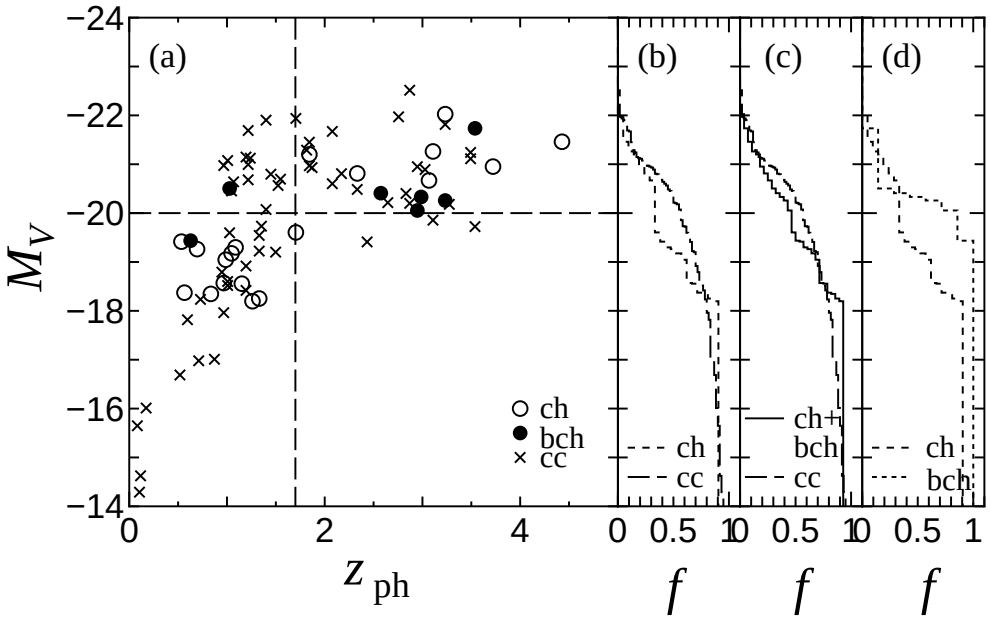

Fig. 6.— (a) Rest-frame V-band absolute magnitude (M_V) as a function of $z_{\rm ph}$. Open circles, filled circles, and crosses show chain, bent-chain, and clump-cluster galaxies, respectively. (b) Cumulative distribution functions of M_V for chain galaxies (short-dashed line) and clump cluster galaxies (dashed line). (c) Cumulative distribution function of M_V for combined sample (chain + bent-chain) (solid line) and clump-cluster (dashed line). (d) Cumulative distribution function of M_V for chain galaxies (short-dashed line) and bent-chain galaxies (dotted line).

typical rest-frame $B-V$ colors of nearby Sbc, Scd, and irregular (Irr) galaxies using the spectral energy distribution obtained by Coleman, Wu, & Weedman (1980). All the chain and bent-chain galaxies have colors within a range of $0 < B-V < 0.3$, being similar to local irregular galaxies. Although 3 clump-cluster galaxies at $1 < z_{\rm ph} < 2$ have redder colors ($B-V \sim 0.4$), the majority of them also tend to be as blue as the chain and bent-chain galaxies.

We show the cumulative distribution functions of rest-frame $B-V$ for the chain and bent-chain samples (panel b), for the combined (chain + bent-chain) and clump-cluster samples (panel c), and for the chain and bent-chain samples (panel d) in Figure 8.

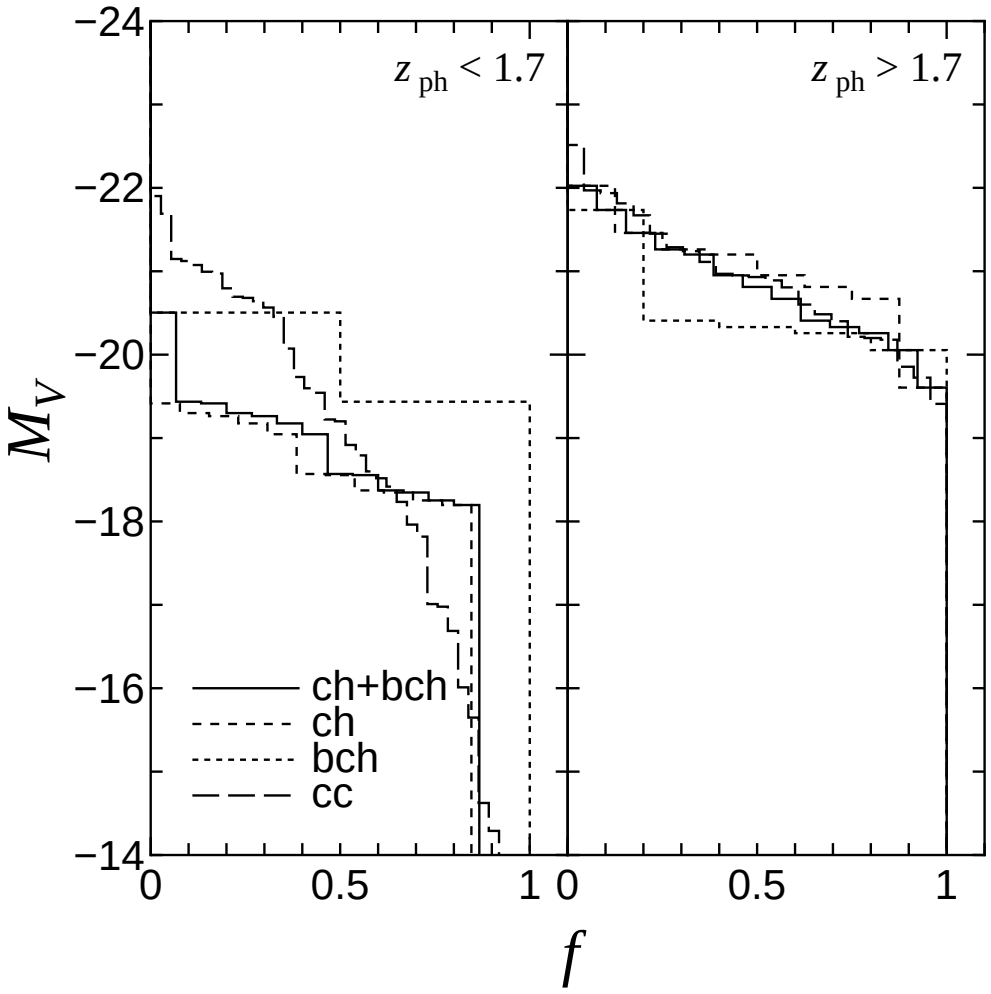

Fig. 7.— Cumulative distribution functions of M_V for the chain (short-dashed line), bent-chain (dotted line), combined sample (chain + bent-chain) (solid line), and clump-cluster samples (dashed line) for $z_{\rm ph} < 1.7$ (left panel) and $z_{\rm ph} \geq 1.7$ (right panel).

Applying the K-S test for the above three comparisons, we obtain the probability of $p = 0.872$, 0.944, and 0.344, respectively. We find that there is little difference in the three comparisons. If chain galaxies are edge-on counterparts of clump-cluster galaxies, they tend to be more reddened by dust extinction (EEH04). However, we cannot find such evidence in our analysis.

Erb et al. (2004) made a spectroscopic study of 13 elongated galaxies at $z \sim 2$ in the GOODS-North field. They found that such elongated galaxies are less reddened than those randomly selected sample galaxies using UV colors. The color properties of our chain galaxies appears to be similar those of their sample galaxies.

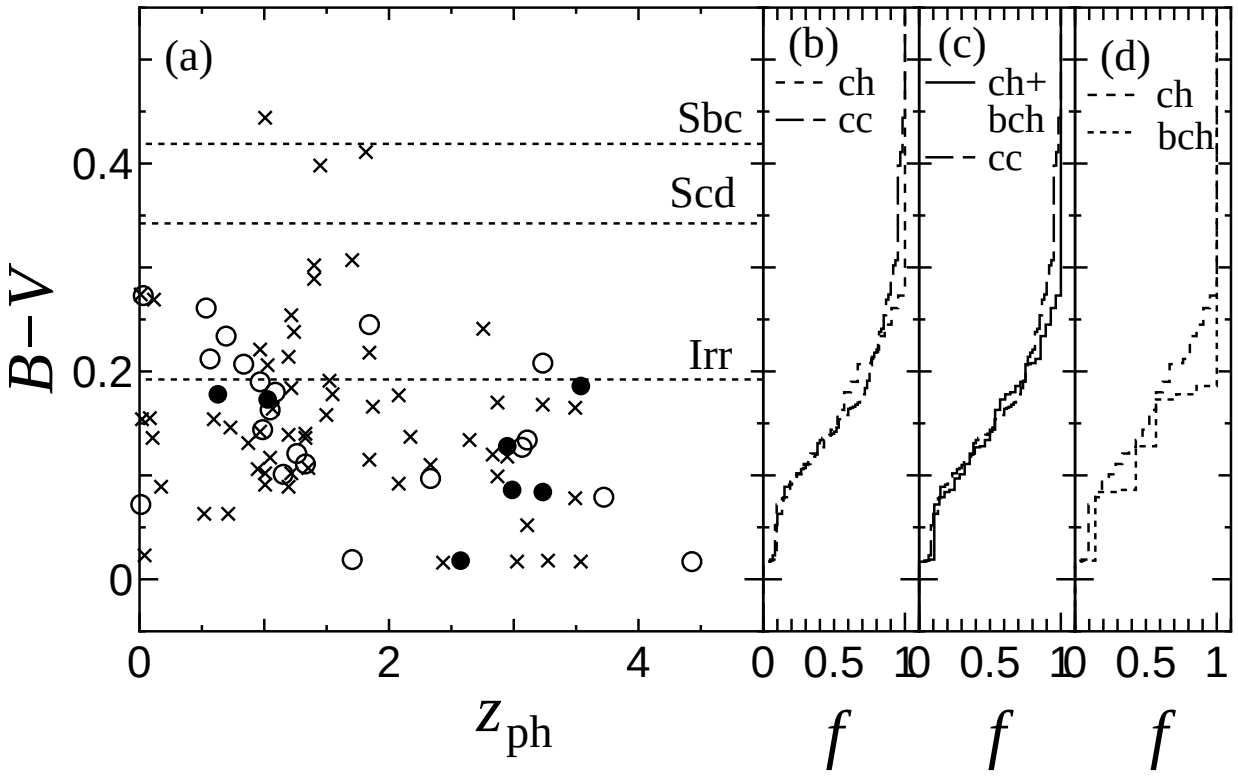

Fig. 8.— (a) Rest-frame $B-V$ color of our samples as a function of $z_{\rm ph}$. Open circles, filled circles, and crosses show the chain, bent-chain, and clump-cluster galaxies. Horizontal dotted lines show the typical $B-V$ colors of Sbc, Scd, and Irr galaxies in the local universe (see text). (b) Cumulative distribution functions of rest-frame $B-V$ color for the chain galaxies (short-dashed line) and clump-cluster galaxies (short dashed line). (c) Cumulative distribution functions of rest-frame $B-V$ color for the combined sample (chain + bent-chain) (solid line) and the clump-cluster galaxies (dashed line). (d) Cumulative distribution functions of rest-frame $B-V$ color for the chain galaxies (short-dashed line) and the bent-chain galaxies (dotted line).

3.4. The Number Ratio between Chain and Clump-Cluster Galaxies

As proposed by EEH04, if all the clump-cluster galaxies are face-on counterparts of chain galaxies, their number ratio is controlled by the median major-to-minor axial ratio of chain galaxies, $f_{\rm axis} = a/b$ where a and b are the major and minor axes, respectively (see Figure 9). Therefore, given the median axial ratio for chain galaxies, we can make an observational test to investigate whether or not all clump-cluster galaxies are face-on counterparts of chain galaxies.

The median major-to-minor axial ratio of chain galaxies, gives a critical viewing angle,

$$\theta_{\rm crit} = 90^\circ - \tan^{-1} f_{\rm axis}^{-1}. \tag{4.1}$$

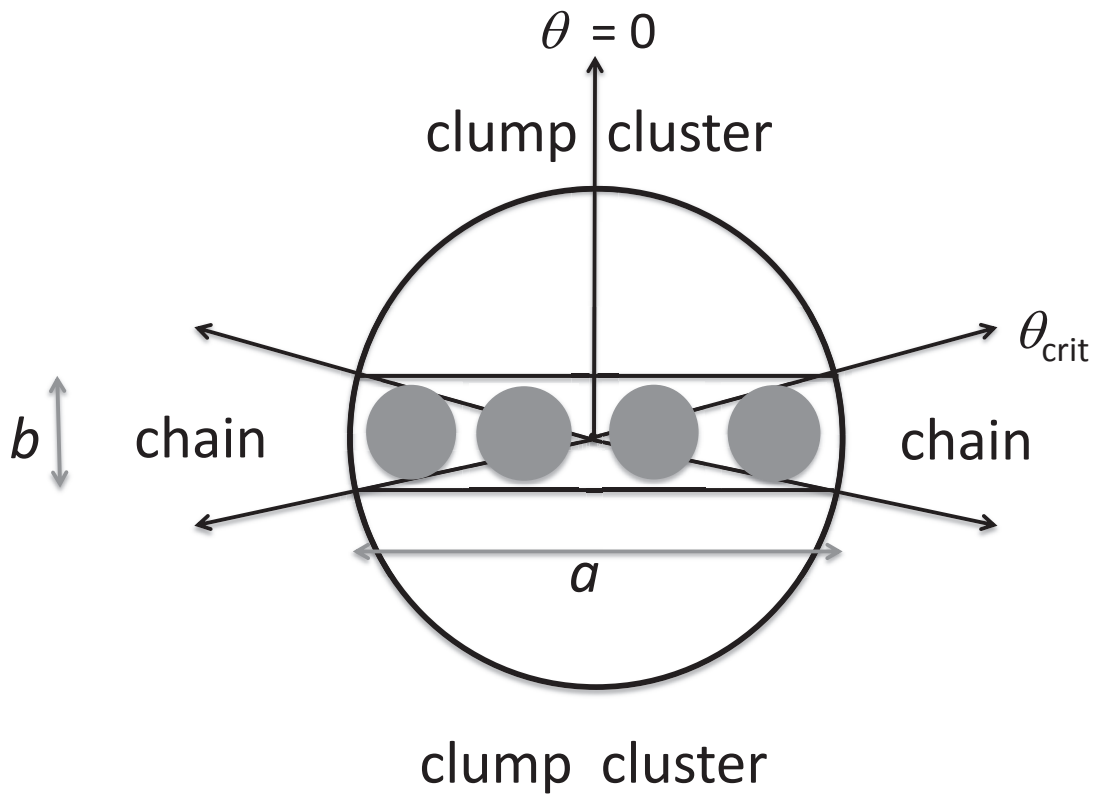

Fig. 9.— The viewing angle dependence of observed morphology of a clump-cluster galaxy.

Clump-cluster galaxies are viewed from an angle of $0 \leq \theta \leq \theta_{\rm crit}$ while chain galaxies are viewed from $\theta_{\rm crit} < \theta \leq 90^\circ$ for the first quadrant. In this case, the numbers of chain and clump-cluster galaxies ($N_{\rm chain}$ and $N_{\rm clump}$, respectively) are related to the critical viewing angle, $\theta_{\rm crit}$, with the following formula,

$$\frac{N_{\rm clump}}{N_{\rm clump} + N_{\rm chain}} = 1 - \cos\theta_{\rm crit}. \tag{4.2}$$

This gives the number ratio between chain and clump-cluster galaxies, R, as

$$R \equiv \frac{N_{\rm chain}}{N_{\rm clump}} = \frac{\cos\theta_{\rm crit}}{1 - \cos\theta_{\rm crit}}. \tag{4.3}$$

In the discovery paper of chain galaxies by Cowie et al. (1995), the median axial ratio is given as $f_{\rm axis} = 4.7 \pm 0.3$. If we adopt $f_{\rm axis} = 5$, we obtain $\theta_{\rm crit} = 78.7^\circ$. This leads to the number ratio between chain and clump-cluster galaxies, $R \simeq 0.25$. On the other hand, EEH04 obtains an axial ratio as $f_{\rm axis} \sim 3$ for their sample galaxies (see their Figure 4). If this is the case, we obtain $R \simeq 0.47$. However, a number of galaxies with a curved morphology are included in their chain galaxy sample, the axial ratio of chain galaxies would be larger than their median value. Therefore, it seems safe to estimate the axial ratio ranges from $f_{\rm axis} \simeq 3$ to 5.

As we described in §2.2.1, the numbers of chain and clump-cluster galaxies are $N_{\rm clump} = 60$ and $N_{\rm chain} = 21$ in our final sample with redshift information, giving the number ratio of $R \simeq 0.35$. This value seems to be consistent with the expected number ratio of $R \simeq 0.25 - 0.47$, corresponding to the axial ratio of $f_{\rm axis} = 5$ to 3.

If bent-chain galaxies are also edge-on counterparts of clump-cluster galaxies, the number ratio between the combined sample (chain + bent-chain) and the clump-cluster sample is related to the critical viewing angle as follows:

$$R \equiv \frac{N_{\rm chain} + N_{\rm bent\text{-}chain}}{N_{\rm clump}} = 0.47.$$

This value also seems to be consistent with the expected number ratio for $f_{\rm axis} = 3$.

3.5. Distributions of the Minor-to-Major Axial Ratio for the Combined Sample of Chain and Clump-Cluster Galaxies

EES04 showed that the distribution of minor-to-major axial ratios for their combined sample of chain and clump-cluster galaxies is similar to that of disk galaxies in the nearby Universe. This is consistent with the idea that chain galaxies are edge-on counterparts of clump-cluster galaxies (see also E05). Let us re-visit this issue based on our new samples described above.

Figure 10 shows the distributions of minor-to-major axial ratio for the chain sample (top), the clump-cluster sample (middle), and our combined sample of chain and clump-cluster galaxies (bottom). For nearby disk galaxies, the distribution appears to be flat for the minor-to-major axial ratio, $r_0 = b/a > 0.2$ (Sandage et al. 1970). However, our combined sample shows a double-peak feature as shown in bottom panel of Figure 10 . A similar distribution is also found for the original sample studied by EEH04.

For a thick ellipsoidal disk with the intrinsic minor-to-major axial ratio, $r_0 = b/a$, the distribution function of the axial ratios should follow the curve $f(r) = [(1 - r_0^2)(1 - r_0^2/r^2)]^{-1/2}$ (Sandage, Freeman, & Stokes 1970). It is also found that the observed distribution of axial ratio for local disk galaxies is explained if the distribution function of the intrinsic minor-to-major axial ratio is a Gaussian with $\mu = 0.25$ and $\sigma = 0.06$, where μ is a position of the peak and σ is a standard deviation (Sandage et al. 1970). Applying the same analysis, we find that the observed distribution of axial ratio for the combined sample of chain and clump-cluster galaxies is also explained if the distribution function of the intrinsic minor-to-major axial ratio is a Gaussian. However, our analysis gives $(\mu, \sigma) = (0.30, 0.10)$. It is interesting to note that the clumpy disks at high redshift are slightly thicker than the disk component in present-day disk galaxies.

4. Discussion

4.1. Comparisons between Chain and Clump-Cluster Galaxies

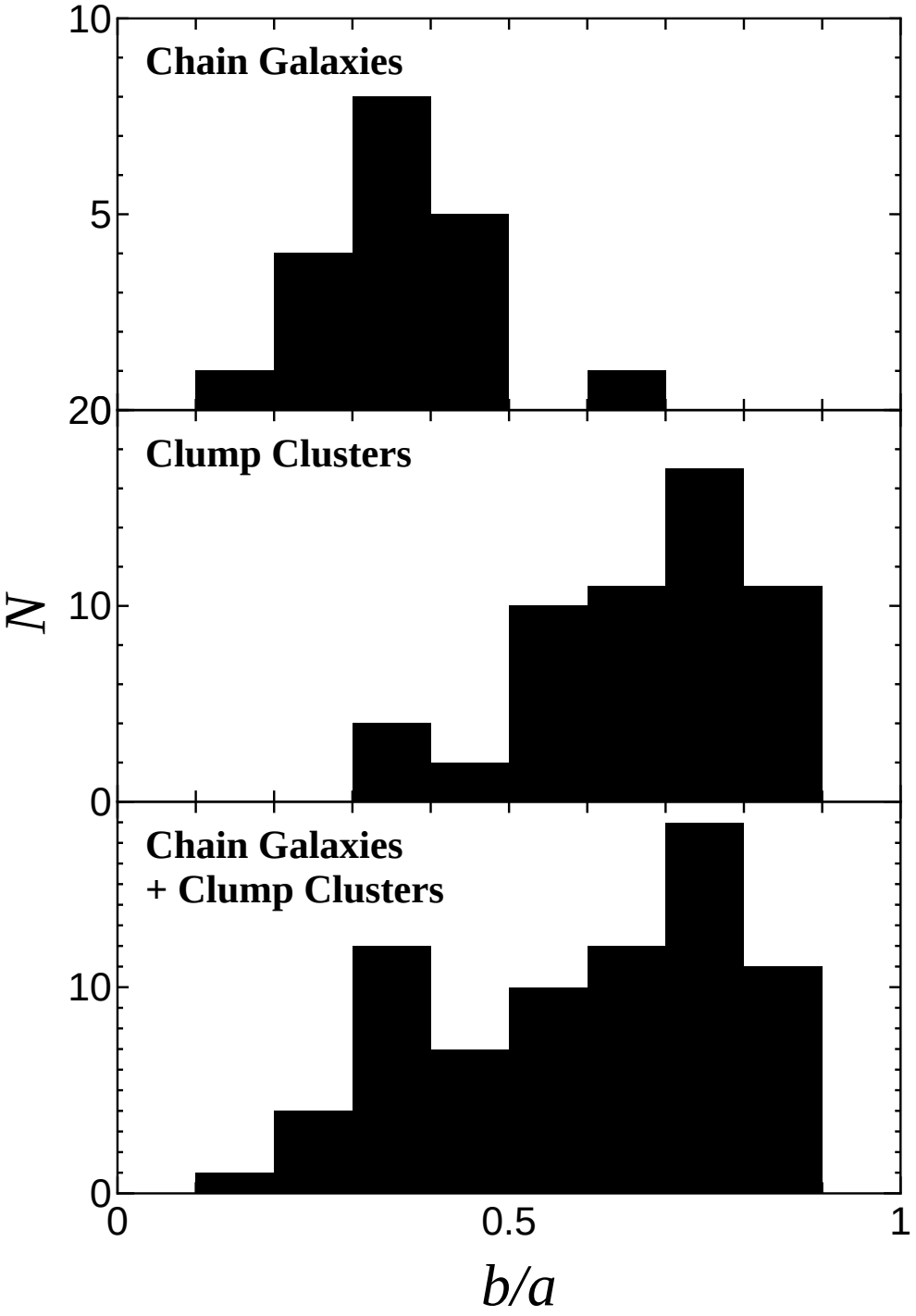

Fig. 10.— Distributions of the minor-to-major axial ratio for the chain galaxies (upper panel), the clump-cluster galaxies (middle panel) and the combined sample of the chain and the clump-cluster galaxies.

First, we summarize our results on the comparative study between the chain (including bent-chain) and the clump-cluster samples analyzed in this study.

- *Absolute V-band magnitude, M_V*
  The distributions of absolute V-band magnitude, M_V, are the same between the chain and clump-cluster samples. Even if we include the bent-chain galaxies into the chain sample, we obtain the same result. However, if we use the subsamples at $z_{\rm ph} < 1.7$, there is no bright chain galaxies (all the chain galaxies are fainter than $M_V = -20$ mag) while the clump-cluster galaxies are distributed in a wide range of magnitude up to $M_V \sim -22$ mag. The K-S test shows that this difference is statistically significant.
- *Rest-frame $B-V$ color*
  There is no statistically significant difference in the rest-frame $B-V$ colors between the chain and clump-cluster samples. It is suggested that there is little difference in both their stellar contents and dust extinction.
- *Number ratio between chain and clump-cluster galaxies*
  The number ratio between chain and clump-cluster galaxies is examined from a viewpoint that chain galaxies are edge-on counterparts of clump-cluster galaxies. We find that the number ratio is almost consistent with the viewpoint above. However, if we include the bent-chain galaxies into the chain sample, a light overabundance of chain galaxies is obtained.
- *Distribution of Axial ratio for the combined sample of chain and clump-cluster galaxies*
  We examine the distribution of axial ratio for the combined sample of chain and clump-cluster galaxies from the same viewpoint that chain galaxies are edge-on counterparts of clump-cluster galaxies. The result is consistent with that expected from the viewpoint. However, it is suggested that clumpy disks at high redshift are slightly thicker than disks in local spiral galaxies.

Our results given above show that there is little difference between the chain and clump-cluster sample used in our analysis in M_V and the rest-frame $B-V$. It is also shown that both the number ratio and axial ratio are interpreted as that chain

galaxies are edge-on counterparts of clump cluster galaxies. However, the observed little difference in the rest-frame $B-V$ color is inconsistent with the expectation that the chain galaxies are redder than the clump-cluster galaxies because of their edge-on view property. It is also noted that the chain galaxies at $z_{\rm ph} < 1.7$ are systematically fainter than the clump-cluster galaxies. Taking all these observational results into account, we conclude that the majority of chain galaxies at high-redshift are the edge-on counterpart of clump-cluster galaxies. Since there present clump-cluster galaxies at high redshift, this conclusion seems to be reasonable. However, the observed little difference in the rest-frame $B-V$ color suggests that all chain galaxies are not necessarily the edge-on counterpart of clump-cluster galaxies. This means that chain galaxies with a linear morphology also present at high redshift although they are not major populations.

4.2. The Presence of Bent-Chain Galaxies

There is another line of evidence for the presence of chain galaxies with a linear or a curved morphology. They are bent-chain galaxies studied by EE06. Fifteen objects are identified as bent-chain galaxies in EE06; five objects are located at $z < 0.3$ while 8 objects are at $z > 0.5$ based on the photometric redshift obtained by COMBO-17 (Wolf et al. 2003). Note that the remaining two objects have no redshift information. We carefully examine their morphology by ourselves and then construct an unambiguous sample of eight bent-chain galaxies (see Figure 11). In our new classification, four objects are classified as interacting galaxies (ID numbers are 26239, 23308, 54277, and the right-bottom galaxy in Figure 3 of their paper). The remaining three galaxies (ID numbers, 27211, 41096, and 30656) are classified as multiple mergers like HDF 2-403 studied by van den Bergh (1996) because they appear to consist of three clumps. Our new classification is summarized in Table 6.

EE06 identified 19 chain galaxies in the same GEMS and GOODS fields. Since the number of bent-chain galaxies is roughly a half of that of chain galaxies (8/19), they are not rare populations. If these bent-chain galaxies would be edge-on counterparts of clump-cluster galaxies, their disks would be significantly warped with either "U"-shaped or "C"-shaped morphology.

The warping of galactic disks itself is often observed in disk galaxies in the nearby Universe, including our Milky Way Galaxy. Although several mechanism have been proposed to explain the observed warping, the warping is one of long-standing problems in galactic dynamics (e.g., Binney & Tremaine 2008). Typically, the warping shows an "integral-sign" shape if we see it from an edge on view. Namely, the warping is observed to be upward at one side while downward at the opposite side. One good example of such a warped disk galaxy in the nearby Universe is a super thin galaxy UGC 3697 that has a physical companion galaxy UGC 3714 (Goad & Roberts 1981).

As shown in Figures 2 and 4, the bent-chain galaxies have either "U" shaped or "C" shaped morphology. Since these morphological properties cannot be explained by the warping of edge-on clump-cluster galaxies, it is strongly suggested that the bent-chain galaxies are genuine chain galaxies with a curved morphology. It is noted that the formation mechanism of chain galaxies proposed by TY01 can explain such bent morphology naturally. In their model, chain galaxies could be born in a shocked cold gaseous shell driven by superwinds. Therefore, such curved morphology is expected as well as linear chain morphology.

Finally, we comment on the bending instability (or the fire-hose instability) in galactic disks (e.g., Toomre 1964; Raha et al. 1991; Merritt & Sellwood 2004; Revaz & Pfenniger 2004). It is known that thin stellar disks are subject to this type of instability if the centrifugal force is stronger than the gravitational restoring force of the disk itself. When this instability occurs in a galactic disk, the disk becomes to show either "U" shaped or "C" shaped morphology because of the bending instability. If we see such disks from an edge-on view, they are observed as bent-chain galaxies. Since galaxies at high redshift are gas-rich, it is uncertain that the bending instability would occur in such gas-rich disks. Although this issue is beyond of the scope of this study, detailed studies of bent-chain galaxies is strongly recommended in future.

4.3. Kinematical Evidence for Chain Galaxies with Little Rotation

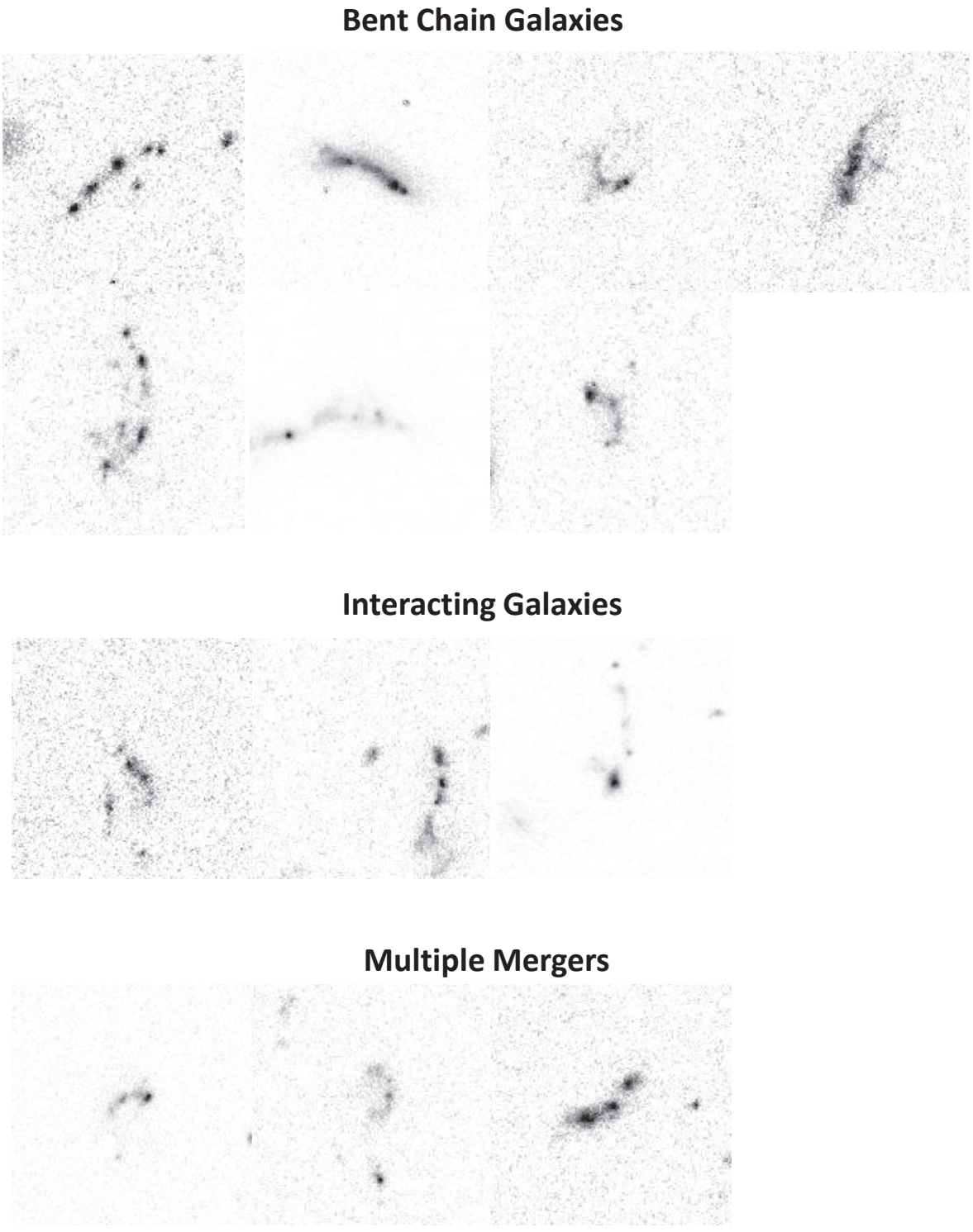

Fig. 11.— V_{606}-band images of bent-chain galaxies in EE06. The image size is 5.0 arcsec × 5.0 arcsec in each panel.

If all chain galaxies at high redshift are the edge-on counterparts of clump-cluster galaxies, they should be observed as rotation-dominated galaxies. However, as noted in Section 1.1, one of the original chain galaxies, HDF 4-455.1 (the Hot Dog galaxy) at $z = 2.803$ does not show any systematic rotational motion (Bunker et al. 2000). In their Keck/LRIS spectrum shows that any systematic rotation is smaller than 100 km s^{-1}.

Erb et al. (2004) investigated the kinematics of 13 elongated galaxies at $z \sim 2$ and found that only two galaxies show the spatially resolved velocity shear, that is expected if the elongated galaxies are highly inclined disks. Weiner et al. (2006) also investigated the morphologies of rotation-dominated galaxies ($V_{\rm rot} > \sigma$) and dispersion dominated galaxies ($V_{\rm rot} < \sigma$) and found that only one-third of chain/hyphen galaxies are dominated by rotation.

Almost all chain galaxies studied in this study are too faint to be observed by optical or near infrared spectroscopy with the available 8 – 10 m class telescopes at present. However, next-generation extremely large optical-infrared telescopes will be capable of carrying out spectroscopic investigations of chain and clump-cluster galaxies at high redshift.

4.4. Comments on Pole-on-View Chain Galaxies

If the structure of high-redshift chain galaxies is a string-like as discussed in TY01, we may observe some of them from a pole on view. Such galaxies are observed to be compact galaxies because a typical radius of clumps in chain galaxies is $\sim 0.5 - 1$ kpc (Elmegreen & Elmegreen 2006a; EE06). It is also expected that the surface brightness is brighter by a factor of several because we observed several clumps along a single line of sight.

Table 6: Summary of Bent-Chain Galaxies in EE06

Our classification	N
Bent-Chain Galaxies	8
Interacting Galaxies	4
Multiple Mergers	3
Total	15

Such very compact galaxies have been found around $z \sim 2$ (van Dokkum et al. 2008). However, some of them have a velocity dispersion of 500 km s^{-1} and thus their dynamical masses are estimated to be $M_{\rm dyn} > 10^{11}\ M_\odot$ (van Dokkum et al. 2009). Since a typical dynamical mass of high-z chain galaxies are of the order of $M_{\rm dyn} \sim 10^9\ M_\odot$, the compact galaxies found by van Dokkum et al. (2008) are not chain galaxies viewed from a pole on. It is, however, noted that some chain galaxy are going to collapse along the chain axis, evolving to dwarf elliptical galaxies in the present day (TY01). If we observe a chain galaxy in such a collapsing phase, we could obtain higher systemic velocity dispersion together with the high surface brightness.

On one hand, a part of extreme emission line galaxies around $z \sim 2$ may be candidates of pole-on-view chain galaxies because of their intense star formation, compactness, small velocity dispersion (~ 50 km s^{-1}, and low systemic mass ($M_{\rm dyn} < 3 \times 10^9\ M_\odot$) (Maseda et al. 2013). It is noted that a typical velocity dispersion of a clump in chain galaxies is $\sigma_v \sim 30(M_{\rm clump}/10^8\ M_\odot)^{1/2}(R/0.5\ {\rm kpc})^{-1/2}$ km s^{-1}, given both a typical clump mass in chain galaxies at $z > 1$, $M_{\rm clump} \sim 10^8\ M_\odot$ and a typical radius of 0.5 kpc (E09a).

5. Concluding Remarks

The presence of bent-chain galaxies reinforces the presence of genuine chain galaxies (hereafter GCGs) that have a linear or curved chain of clumps in early Universe. This is also advocated by the presence of little rotation in a number of chain-like galaxies at high redshift. Since if we observe a bent-chain galaxy from an edge-on view, it is observed as a linear chain galaxies. The observed numbers of chain and bent-chain galaxies are not large enough to study their statistical properties based on our present samples. However, in conclusion, some GCGs are surely present in the high redshift Universe although it is considered that they are minor populations because of their dynamically unstable nature.

Incorporating the above arguments, we propose a new classification scheme of chain galaxies. One is GCGs. This class is divided into the following two subclasses; (1) linear-chain galaxies, and (2) bent-chain galaxies. It is noted that a part of bent-chain galaxies are classified as linear-chain galaxies, depending on the viewing angle to them.

The other class is edge-on counterparts of clump-cluster galaxies. In Figure 12 , we show a summary of our new classification scheme.

GCGs consist of several clumps with a linear configuration. Although we do not know star formation activity in the whole region of a GCG, star formation activity should be much higher in the clumps than in inter-clump regions by the appearance. On the other hand, if clump-cluster galaxies come from the gravitational instability of a gas-rich disk, a moderate level of star formation activity could also occur in the inter-clump regions (e.g., Noguchi 1998; Ceverino et al. 2010). If chain galaxies are edge-on counterparts of such clump-cluster galaxies, their inter-clump regions could be fairly brighter than those of GCGs. Since the star formation history is expected to be different from galaxy to galaxy, it seems difficult to specify the critical surface brightness of inter-clump regions that distinguish the two populations. However, this surface brightness test will be useful in future investigations on the relationship between GCGs and clump-cluster galaxies.

Appendix

A1. galaxies that are not classified as either, chain, bent-chain, or clump-cluster galaxies in our new classification

As shown in Table 1, 43 out of 112 chain galaxies in E05 are classified as chain galaxies, bent-chain galaxies, or clump-cluster galaxies in our classification. The remaining 69

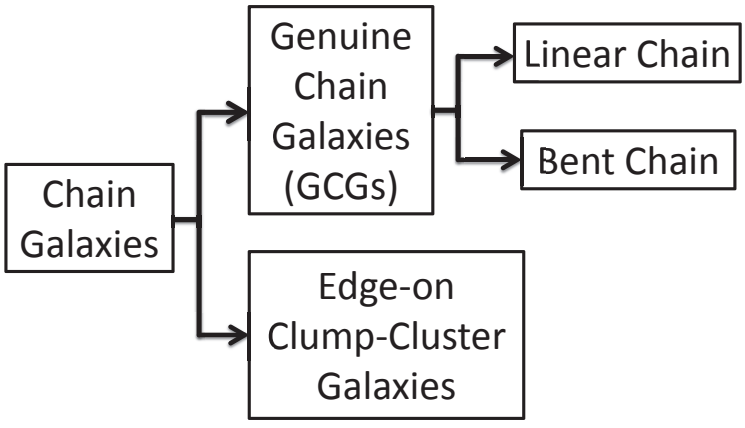

Fig. 12.— The classification of chain galaxies.

galaxies are possible interacting and/or merging galaxies. HST/ACS i_{775}-band images of them are shown in Figure 13. Similarly, 69 out of 176 clump-cluster galaxies in E05 are classified either as bent-chain galaxies, or as clump-cluster galaxies in our classification. The remaining 107 galaxies are possible interacting or merging galaxies. Their HST/ACS i_{775}-band images are shown in Figure 14.

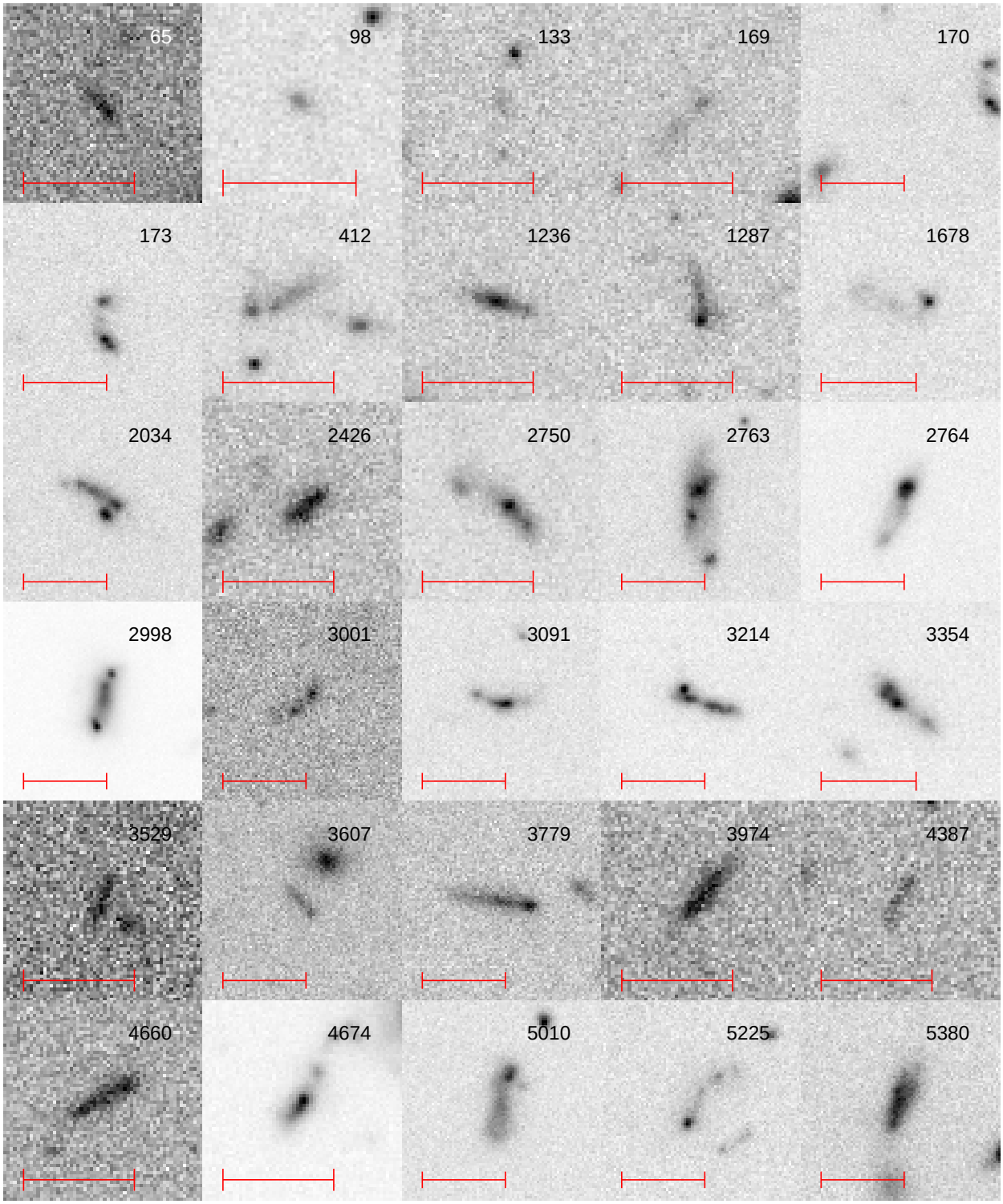

Fig. 13.— HST/ACS i_{775}-band images of chain galaxies in E05 but possible interacting and/or merging galaxies in our classification.

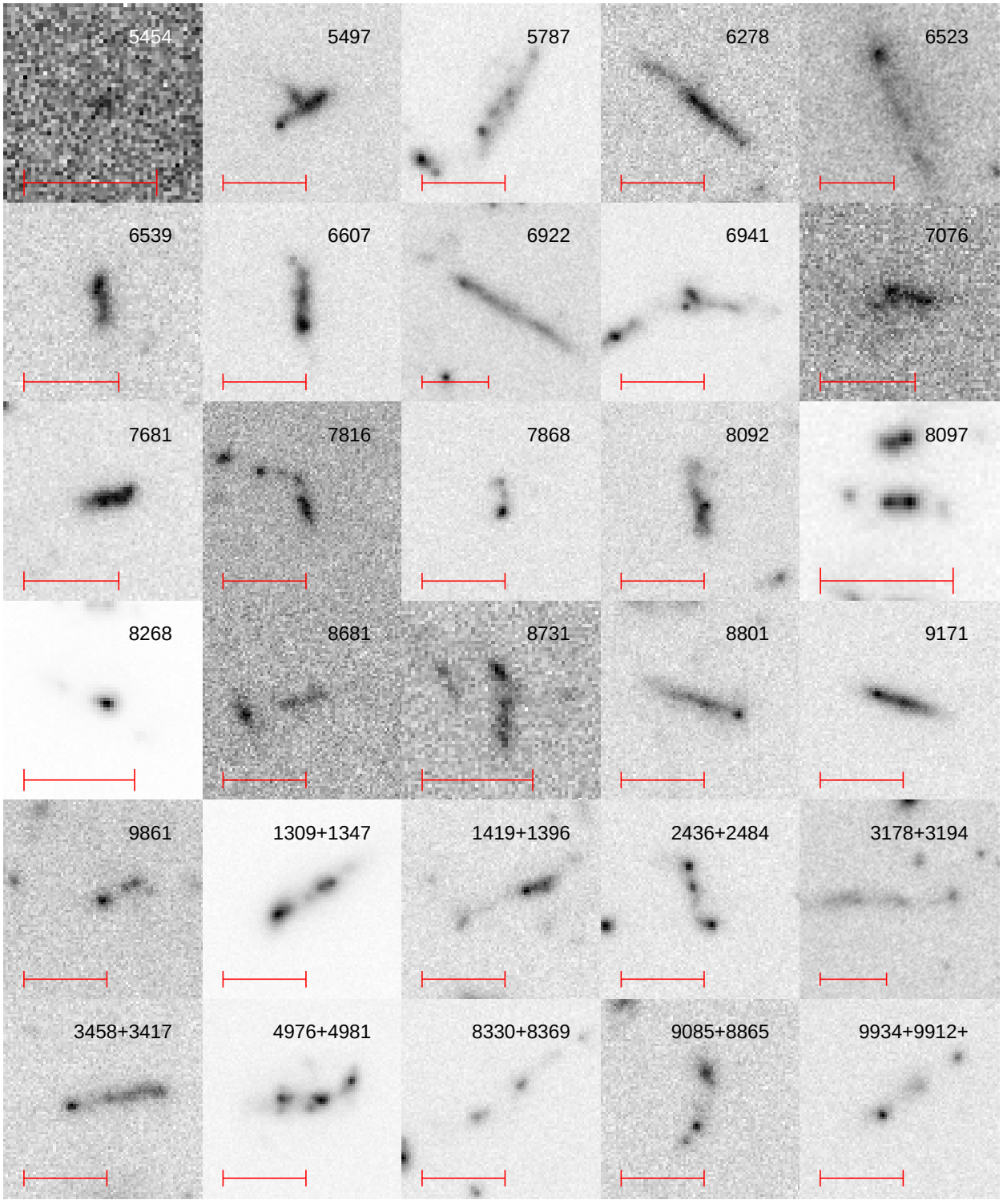

Fig. 13.— (Continued.)

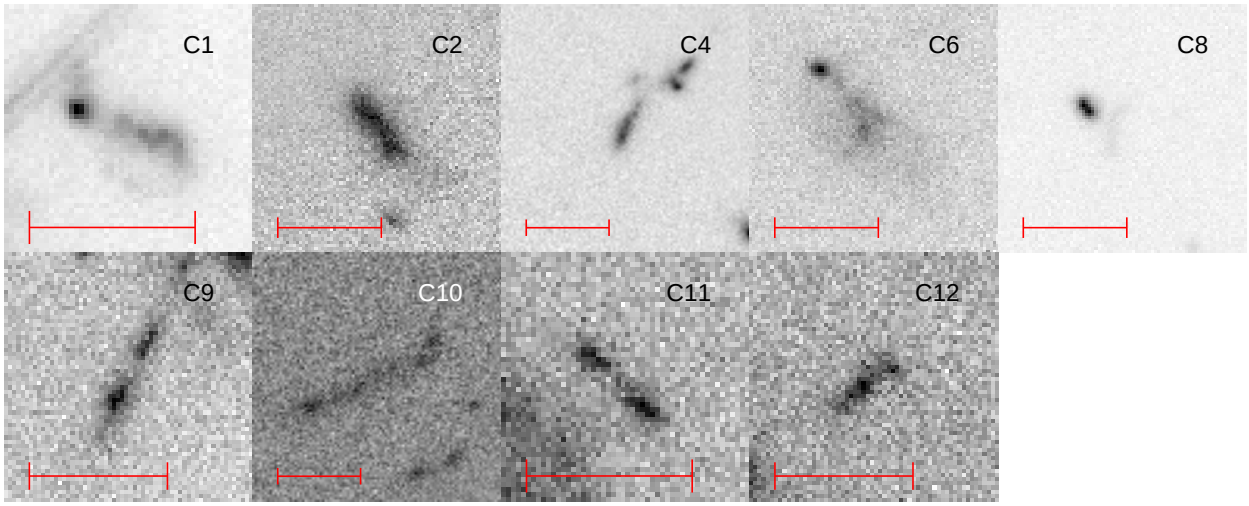

Fig. 13.— (Continued.)

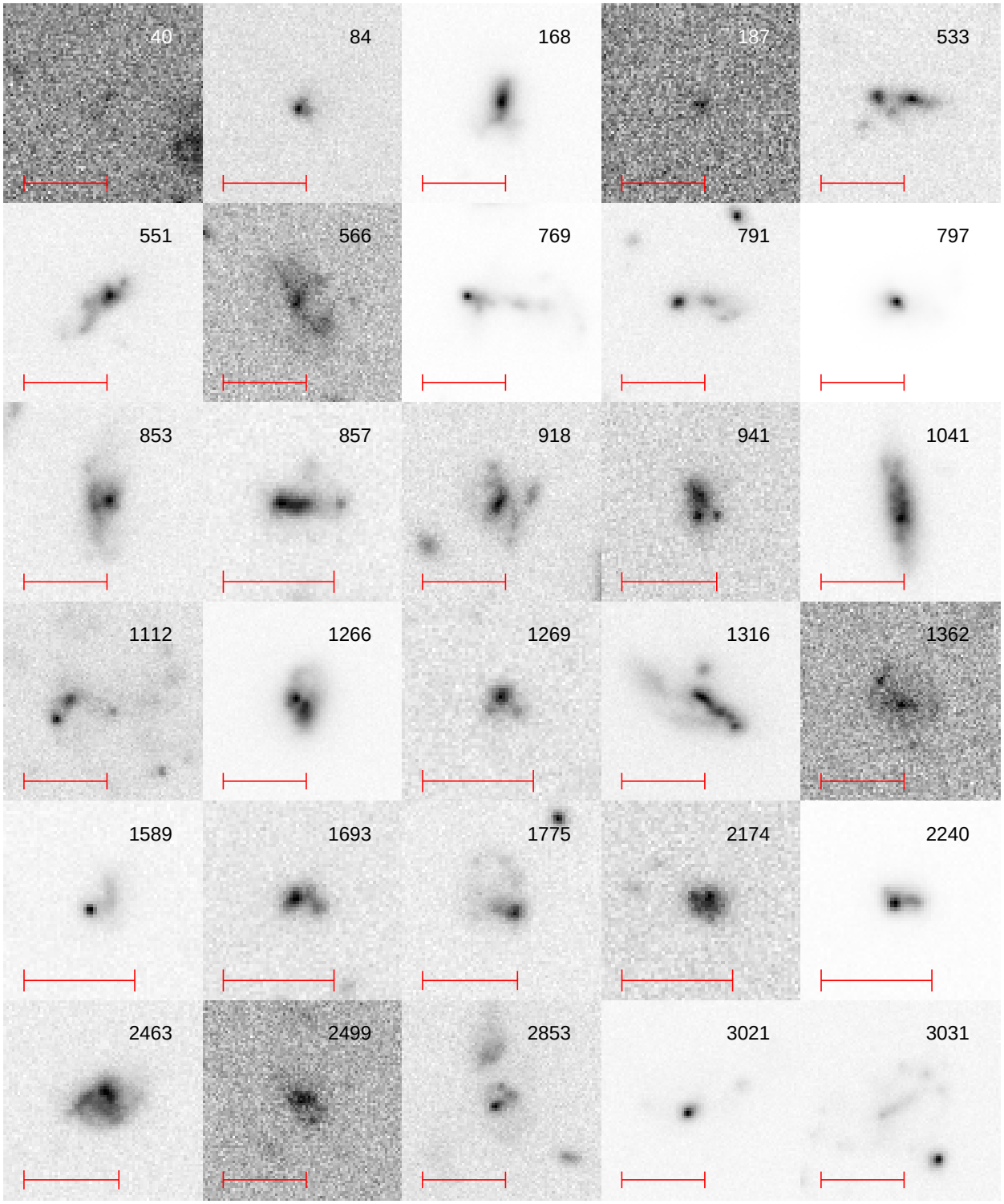

Fig. 14.— HST/ACS i_{775}-band images of clump-cluster galaxies in E05 but possible interacting and/or merging galaxies in our classification.

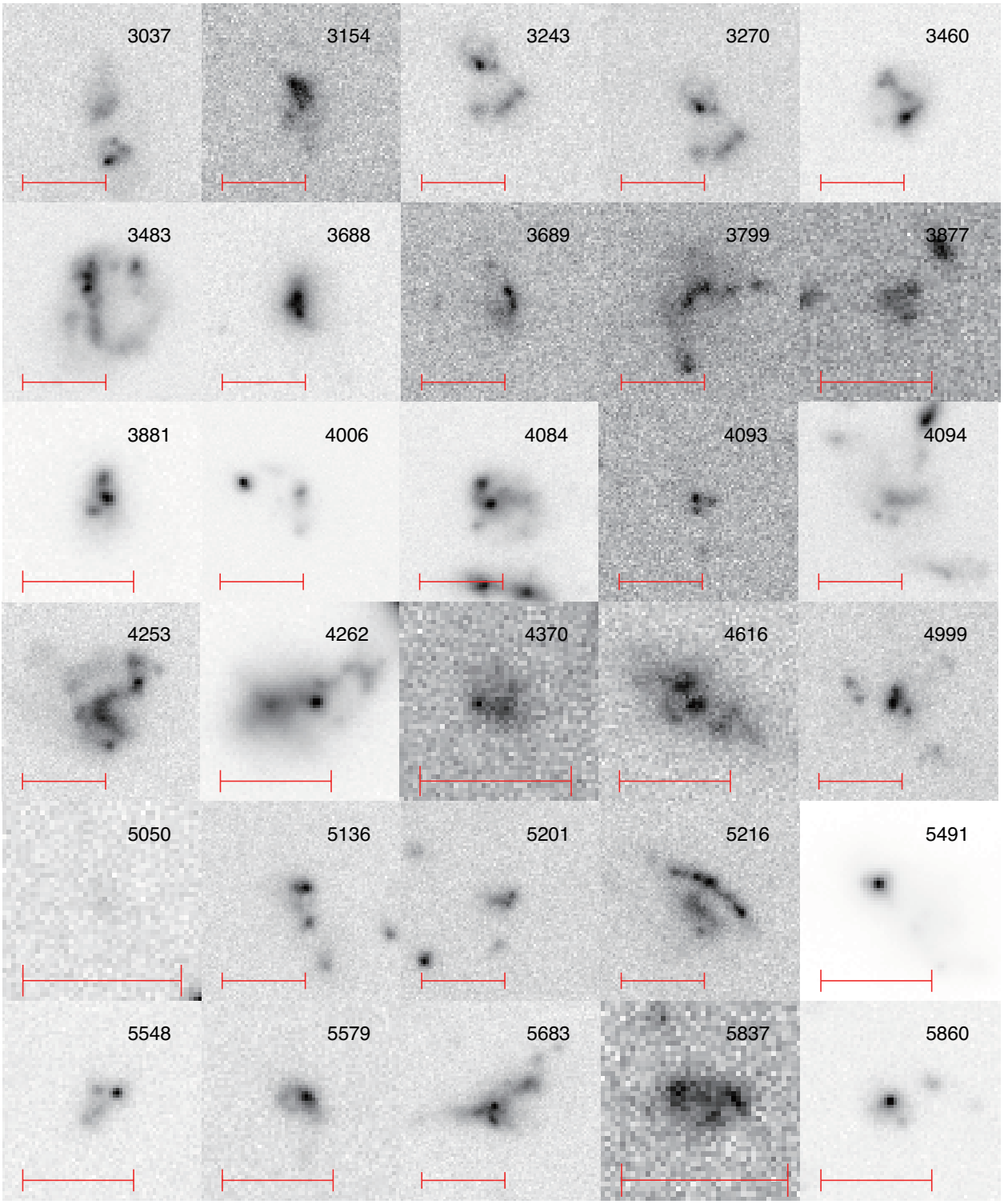

Fig. 14.— (Continued.)

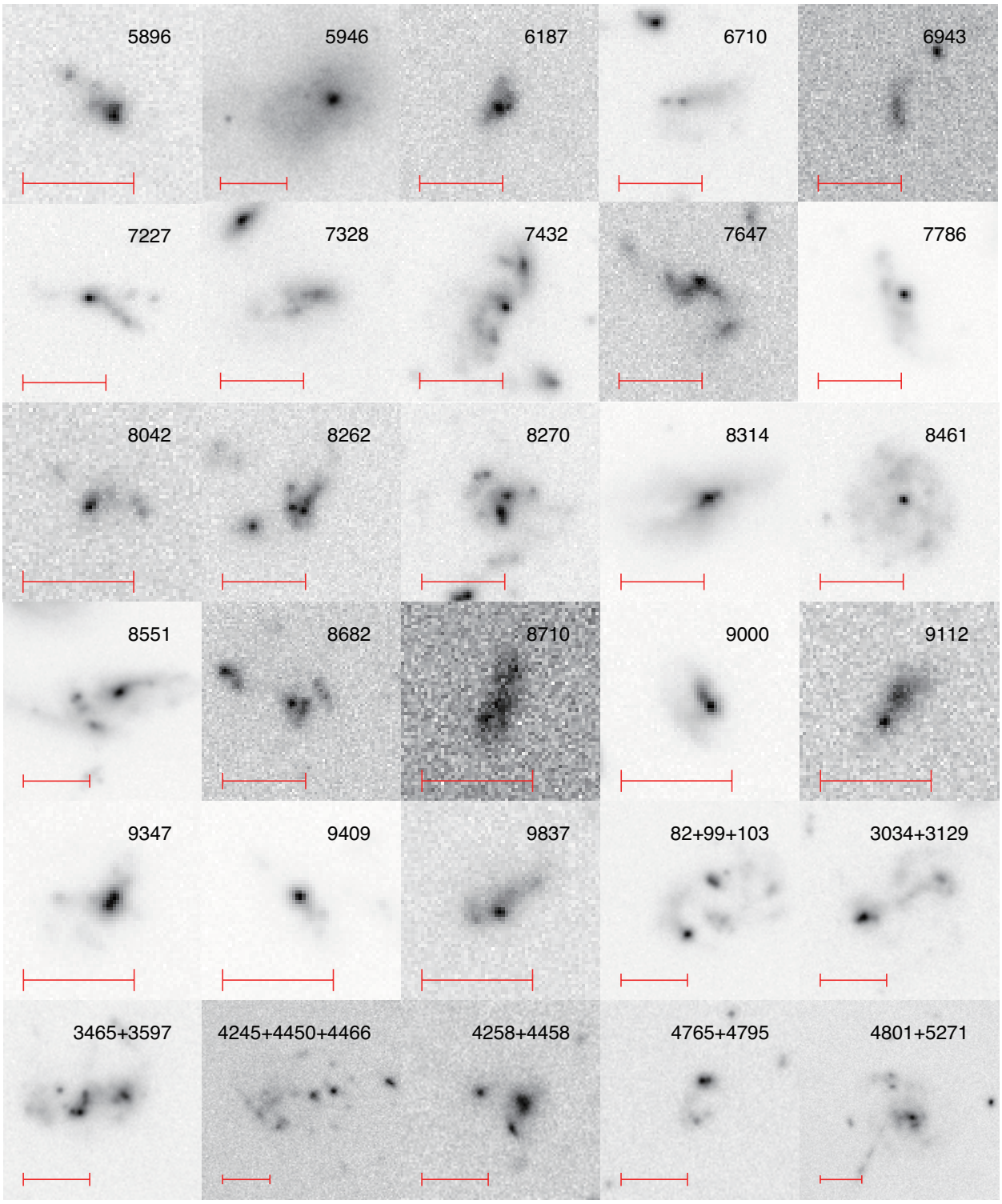

Fig. 14.— (Continued.)

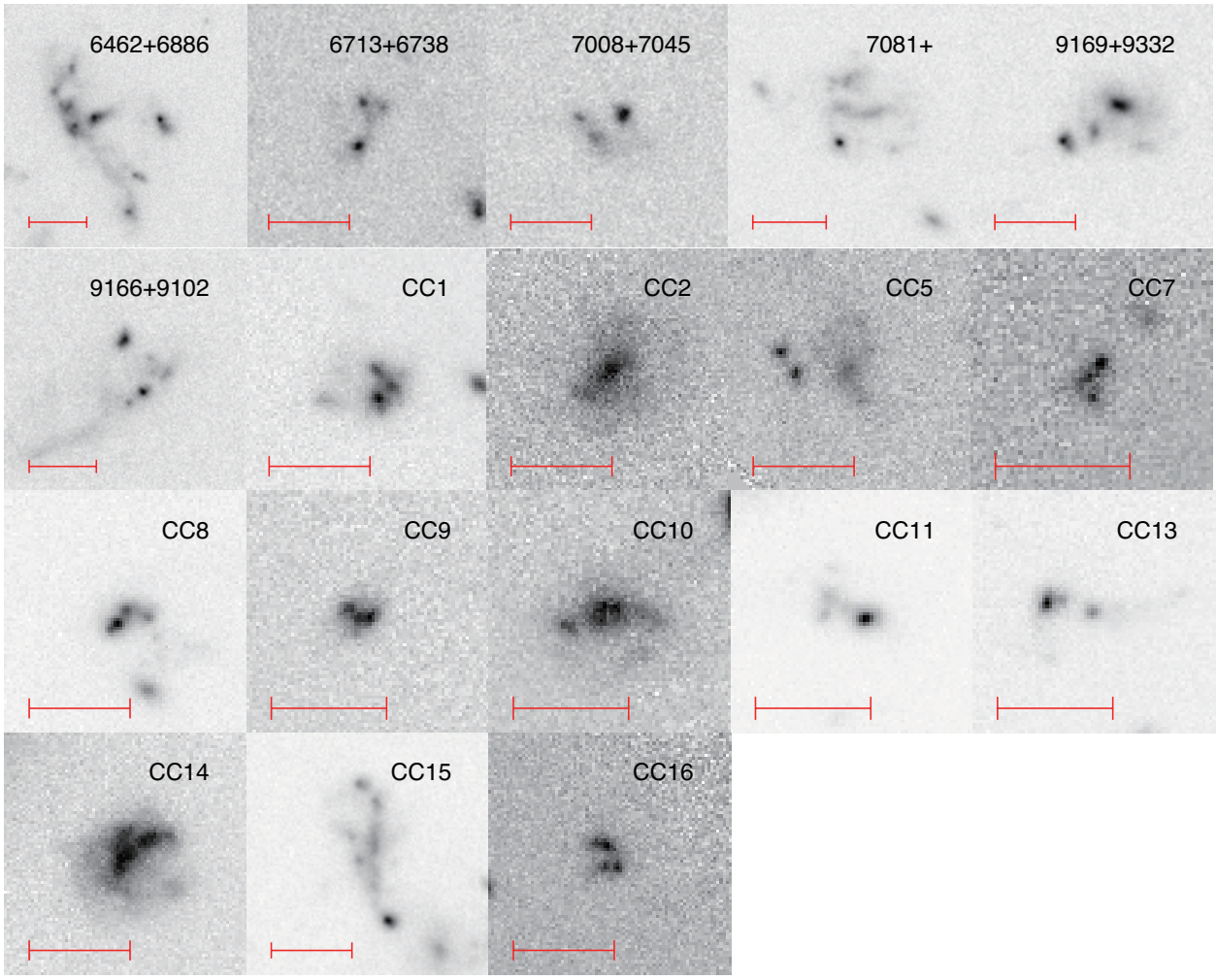

Fig. 14.— (Continued.)

A2. Our sample galaxies with $i_{775} > 26.5$ and no CANDELS data

As we described in §2.1, we remove 15 chain galaxies, 4 bent-chain galaxies, and 8 clump-cluster galaxies from our final samples, since they are fainter than $i_{775} = 26.5$ or there is no counterpart in the CANDELS photometric catalog. Although they are not in the final samples and not used in our analysis, we show their i_{775}-band images in Figures 15 – 19. The chain galaxies are shown in Figures 15 and 16, the bent-chain galaxies are shown in Figure 15, and the clump-cluster galaxies are shown in Figures 18 and 19.

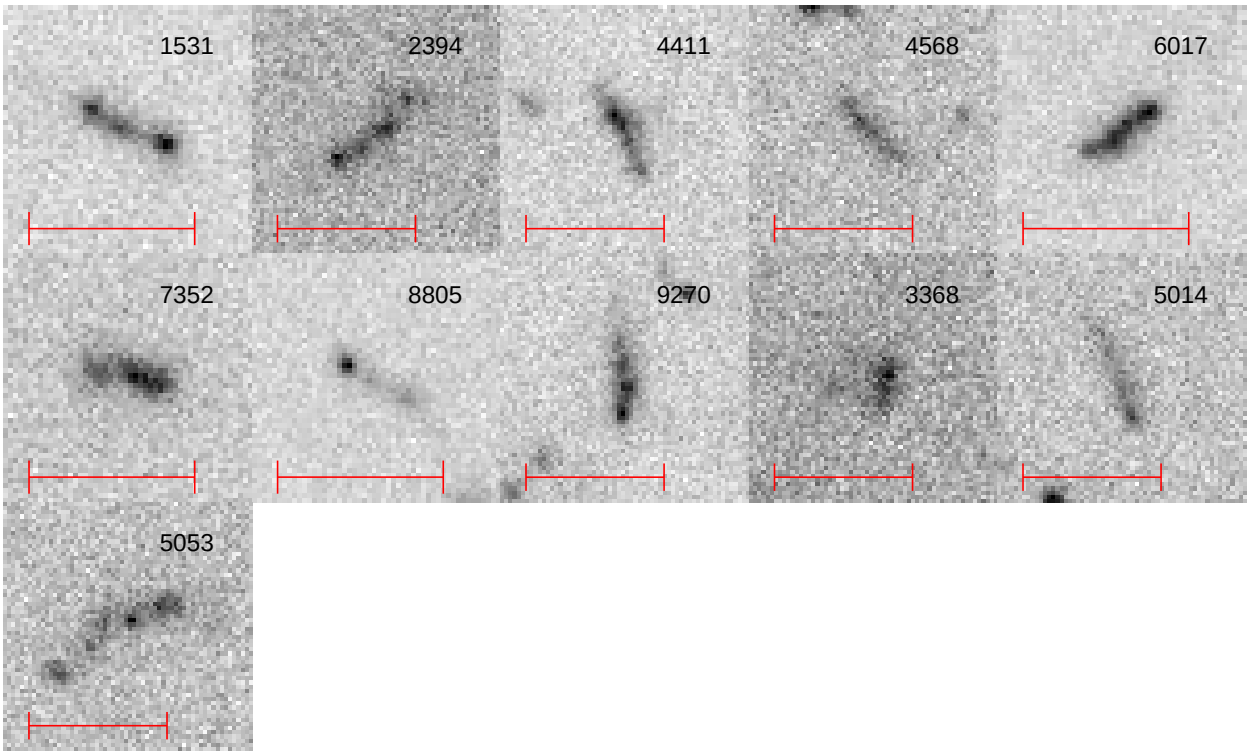

Fig. 15.— Same as Figure 3 but for the chain galaxies with $i_{775} > 26.5$.

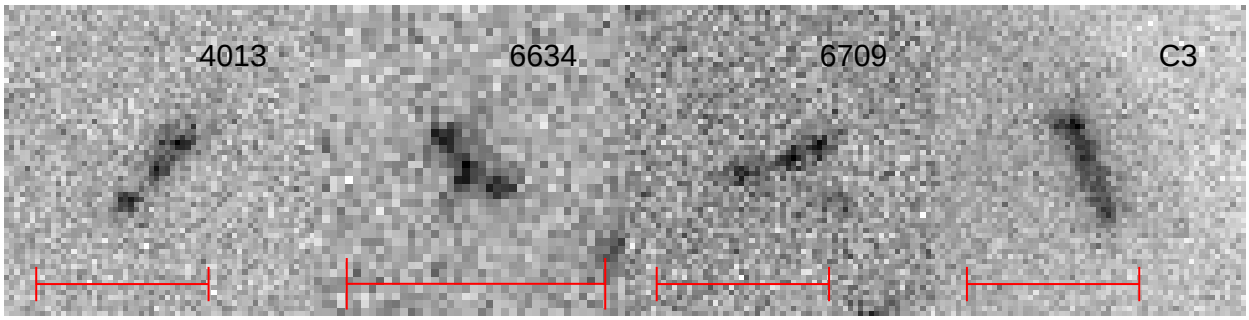

Fig. 16.— Same as Figure 3 but for the chain galaxies that are not in the CANDELS photometric catalog.

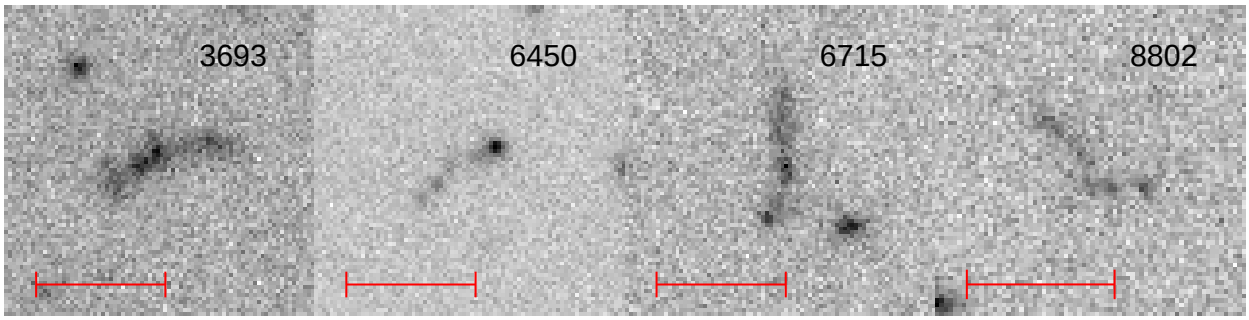

Fig. 17.— Same as Figure 4 but for the bent-chain galaxies with $i_{775} > 26.5$.

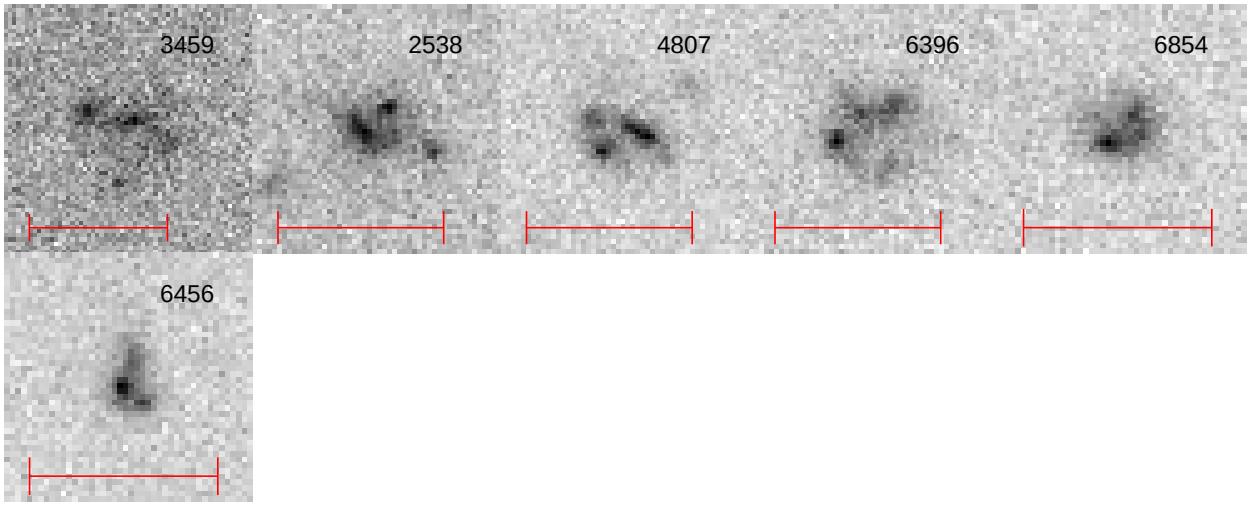

Fig. 18.— Same as Figure 5 but for the clump-cluster galaxies with $i_{775} > 26.5$.

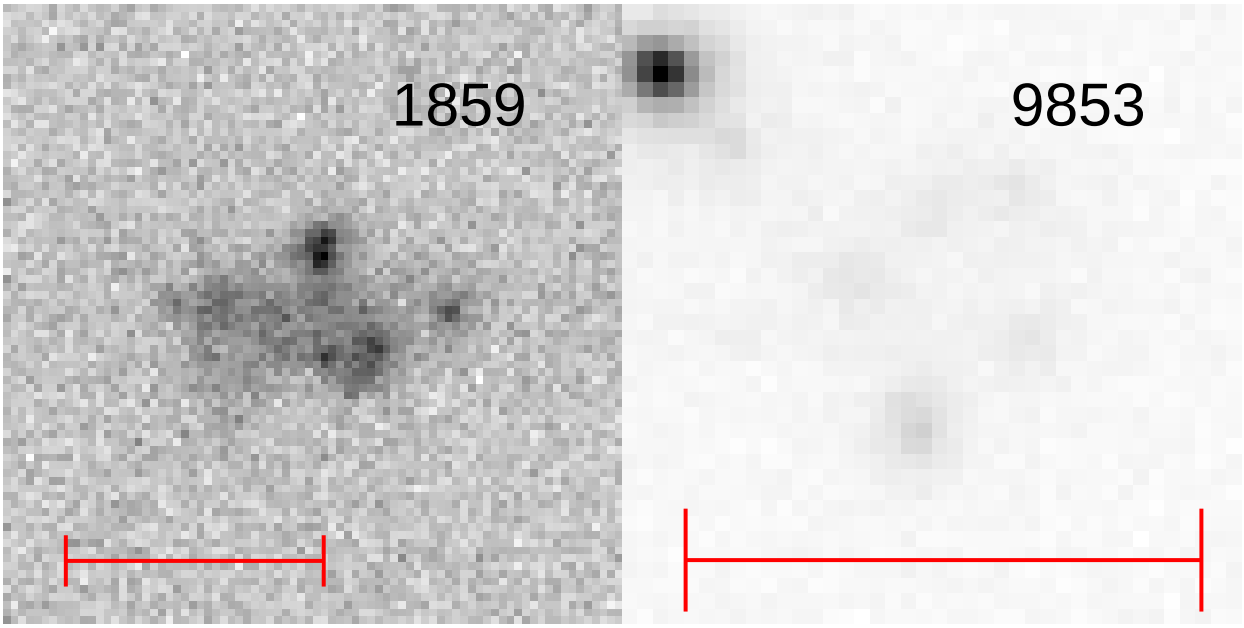

Fig. 19.— Same as Figure 5 but for the clump-cluster galaxies that are not in the CANDELS photometric catalog.

Chapter 5

SUMMARY

In this thesis, we have investigated high-redshift galaxies. In Chapter 2, we have studied the evolution of the fraction of clumpy galaxies in the COSMOS Field which is main study of this thesis. Also, we have studied tadpole galaxies with a bright knot at one end together with a long tail structure in stellar continuum emission (Chapter 3), and chain galaxies with linearly-distributed more than two clumps (Chapter 4).

1. Evolution of Clumpy Galaxies in the COSMOS Field

In Chapter 2, we have constructed a large sample of clumpy galaxies at $0.2 < z < 1.0$ in the COSMOS 2 deg^2 field using the HST/ACS data and investigated the fraction of these galaxies and its evolution as a function of stellar mass, SFR, and SSFR. This is the first systematic search for clumpy galaxies at $z < 1$. Our conclusion are summarized below.

(1) The fraction of clumpy galaxies in star-forming galaxies decreases with time from ~ 0.3 at $0.8 < z < 1.0$ to ~ 0.05 at $0.2 < z < 0.4$ irrespective of stellar mass.

(2) The fraction of clumpy galaxies increases with increasing both SFR and SSFR in all the redshift ranges we investigated. In particular, the SSFR dependences of the fractions are similar among galaxies with different stellar masses. Moreover the fraction at a given SSFR does not depend on stellar mass in each redshift bin.

(3) The fraction of clumpy galaxies at a given SSFR decreases with time at $SSFR > 0.1$

Gyr^{-1}. This can be explained by the effect of the morphological K-correction.

(4) The above results are understood by the gravitational fragmentation model for the formation of giant clumps in disks galaxies, where the gas mass fraction is a crucial parameter.

2. Genuine Tadpole Galaxies in High Redshift Universe

In Chapter 3, we have studied high-redshift tadpole galaxies in the Hubble Ultra Deep Field. Our conclusions are summarized below.

(1) In high-redshift universe, genuine tadpole galaxies (GTGs) which are tadpole galaxies without any signatures for galaxy interaction and/or merger exist. The GTG is a unique population in high-redshift universe.

(2) We have examined the possibility that the GTGs could be made by the ram-pressure stripping in dense IGM environments and/or cosmic-web stripping as large-scale structure forms. Our analysis suggest that such ram-pressure and/or cosmic-web stripping can occur at high redshift.

(3) However, physical conditions of cold gas clouds in galaxies and the IGM at high redshift have not yet been investigated accurately. Future new observations will prove whether or not the ram-pressure driven formation of tadpole galaxies occurs. If this mechanism works efficiently at high redshift, a new insight will be obtained for the understanding early evolution of galaxies.

(4) It is finally mentioned that a half of the tadpole sample galaxies in E05 are not classified as tadpole galaxies in our new classification. On one hand, some well-defined tadpole galaxies are found in the catalog of chain galaxies in Elmegreen et al. (2005). This means that eye-ball classification is generally difficult, in particular for distant small galaxies. Computer-aided automatic classifiers will be necessary to classify such galaxies in future.

3. Genuine Chain Galaxies in High Redshift Universe

In Chapter 3, in order to investigate the origin of chain galaxies at high redshift, we have investigated the observational properties of chain, bent-chain, and the clump-cluster galaxies in the Hubble Ultra Deep Field, catalogued by Elmegreen et al. (2005). Our conclusions are summarized below.

(1) Since it appears that interacting/merging galaxies are also classified as the above three types of galaxies in previous studies, we have re-classified all the sample galaxies by ourselves and then obtained unambiguous samples of 36 chain, 11 bent-chain, and 68 clump-cluster galaxies. In order to secure the accuracy of photometric redshift, we use 21 chain, 7 bent-chain, and 60 clump-cluster galaxies that are brighter than $i_{775} = 26.5$ AB magnitude. Using the photometric data of CANDELS, we evaluate their photometric redshifts, V-band absolute magnitudes (M_V), and rest-frame $B - V$ colors.

(2) It is found that the distributions of M_V and rest-frame $B - V$ color between chain and clump-cluster galaxies cannot be distinguished from K-S statistical tests. If all chain galaxies were the edge-on counterpart of clump-cluster galaxies, chain galaxies would tend to be fainter and redder because of larger extinction. It is thus suggested that a part of chain galaxies are genuine chain galaxies that have a linear structure.

(3) Another line of evidence for such genuine chain galaxies is the presence of bent-chain galaxies that are chain galaxies with a curved morphology. If these bent-chain galaxies are the edge-on counterpart of clump-cluster galaxies, they would have either "U"-shaped or "C"-shaped warping in their putative disk although we cannot rule out a possibility of the bending (or fire-hose) instability.

(4) Accordingly, we suggest that there present genuine chain galaxies with a linear or curved morphology at high redshift although they are considered to be rare because of their dynamically unstable property.

Appendix A

THE COSMOS PHOTOMETRIC REDSHIFT CATALOG

In Chapter 2, we used the COSMOS photometric redshift catalog by Ilbert et al. (2009, 2010, hereafter I09 and I10) from which the redshift and physical quantities like stellar mass and star formation rate (SFR) of galaxies are extracted. These values are computed by comparing the observed spectral energy distribution (SED) with SED templates, so-called SED fitting. The connection between observed SED and the physical quantities is based on the framework of the stellar population synthesis (SPS). Here, we introduce the basic concept of SPS in Section 1 and summarize the COSMOS photometric redshift catalog in Section 2.

1. Stellar Population Synthesis

Stellar population synthesis model produces a SED of a galaxy by following the evolution of main sequence (MS) stars and post-MS stars without taking into account the dynamics of a galaxy. It also includes the total effective extinction, the absorption and re-emission of hydrogen gas. Once star formation history (SFH), initial mass function (IMF), metallicity and extinction law are assumed, some physical quantities (stellar mass, turn-off mass of HR-diagram, supernova rate and number of black holes, neutron stars and white dwarfs, etc.) are given at any time. Here, we briefly summarize quantities predicted by SPS

model.

Let us begin with considering the relation between a luminosity and an SFH. Let $L_\lambda(t)$ be a specific luminosity at a galaxy age t, and $\psi(t-t')$ be a star formation rate (SFR), which is defined as the total stellar mass formed in unit time in a galaxy, at age $t-t'$ and $\phi(m)$ be an initial mass function defined in such a way that $\phi(m)\,\mathrm{d}m$ means the number of initially formed stars with their stellar mass in a mass range $[m,\ m+\mathrm{d}m]$ in a galaxy. Then

$$L_\lambda(t) = \exp\left[-\hat{\tau}_\lambda\right]\ L^0_\lambda(t), \tag{A.1}$$

$$L^0_\lambda(t) = \int_0^t \psi(t-t')\ S_\lambda(t')\,\mathrm{d}t', \tag{A.2}$$

$$S_\lambda(t') = \frac{\displaystyle\int_{m_{\min}}^{m(t')} \phi(m)\ l_\lambda(m,t')\,\mathrm{d}m}{\displaystyle\int_{m_{\min}}^{m(t')} \phi(m)\ m\,\mathrm{d}m}, \tag{A.3}$$

where $\hat{\tau}_\lambda$ is the total effective extinction, $L^0_\lambda(t)$ is the intrinsic specific luminosity at age t, $S_\lambda(t')$ is the specific luminosity per unit stellar mass at age t', m means the stellar mass, $l_\lambda(m,t')$ is the specific luminosity of a star with mass m at age t', $m(t')$ is the mass of the main sequence star of life duration t', and $m_{\min}$ is the minimum mass of the initially formed stars. In the above equations, we assume that the total effective extinction, the IMF and the metallicity are independent of time.

The stellar mass of a galaxy at time t is expressed as

$$M_*(t) = \int_0^t \psi(t-t')\ \ [1-R(t')]\ \mathrm{d}t', \tag{A.4}$$

$$R(t') = \frac{\displaystyle\int_{m(t')}^{m_{\max}} \phi(m)\ m\,\mathrm{d}m}{\displaystyle\int_{m_{\min}}^{m_{\max}} \phi(m)\ m\,\mathrm{d}m}, \tag{A.5}$$

where $R(t')$ is the recycled gas fraction at age t' and $m_{\max}$ is the maximum mass of the initially formed stars. In the case of the Chabrier IMF, almost a half of stellar mass of formed stars is recycled to the interstellar gas in the galaxy.

The star formation rate is traditionally estimated by the flux at UV wavelengths, which is produced by short-lived OB stars.

In the case of UV (1500 Å $\lesssim \lambda \lesssim$ 2500 Å), eq. (A.3) is approximated by

$$S_\lambda(t') \sim \frac{\int_{m_{\rm OB}}^{m(t')} \phi(m)\, l_\lambda(m,t')\,{\rm d}m}{\int_{m_{\rm min}}^{m(t')} \phi(m)\, m\,{\rm d}m}, \tag{A.6}$$

where $m_{\rm OB}$ is the minimum mass among OB stars which dominantly radiate at the UV.

$$L^0_\lambda(t) \sim \int_0^{t_{\rm OB}} \psi(t-t')\, S_\lambda(t')\,{\rm d}t' \tag{A.7}$$

$$= \int_0^{t_{\rm OB}} [\psi(t) - \frac{d\psi(t)}{dt}t' + \ldots]\, S_\lambda(t')\,{\rm d}t' \tag{A.8}$$

$$= \psi(t)\int_0^{t_{\rm OB}} S_\lambda(t')\,{\rm d}t' - \frac{d\psi(t)}{dt}\int_0^{t_{\rm OB}} t'\, S_\lambda(t'){\rm d}t' + \ldots, \tag{A.9}$$

where $t_{\rm OB}$ is the lifetime of the stars with a mass $m_{\rm OB}$. Further, assuming the timescale of the variation of SFR is much longer than $t_{\rm OB}$, eq. (A.9) is approximated by

$$\psi(t) \sim \frac{L^0_\lambda(t)}{\int_0^{t_{\rm OB}} S_\lambda(t')\,{\rm d}t'}. \tag{A.10}$$

This means that SFR is estimated by UV light.

The galaxy with a specific luminosity L_λ at redshift z is observed with a specific flux $F_{\lambda_{\rm obs}}$

$$F_{\lambda_{\rm obs}} = \frac{1}{1+z}\,\frac{L_\lambda}{4\pi d^2_{\rm L}(z)}, \tag{A.11}$$

$$\lambda_{\rm obs} = (1+z)\lambda, \tag{A.12}$$

where $\lambda_{\rm obs}$ is the wavelength at the rest-frame of an observer, and $d_{\rm L}(z)$ is the luminosity distance corresponding to the redshift z. Here, we assume the SFR to be exponentially declining

$$\psi(t) = \psi_0\, \exp\left[-\frac{t}{\tau}\right], \tag{A.13}$$

where ψ_0 is the initial SFR and τ is the e-folding time scale. Assuming IMF, observed specific flux at redshift z with specific SPS model is written as

$$F_{\lambda_{\rm obs}}(z) = F_{\lambda_{\rm obs}}(z \mid t, \psi_0, \tau, Z, \hat{\tau}_\lambda). \tag{A.14}$$

2. The COSMOS Photometric Redshift Catalog

2.1. Redshift

The redshift of a galaxy is evaluated through a comparison between its observed SED and SED templates. This procedure is called the SED fitting and such redshift is called photometric redshift (photo-z). The SED fitting of I09 is carried out using 30 bands including broad and intermediate bands, which enables accurate photo-z estimation.

The photo-z is determined as minimizing the following merit function $\chi^2(z, T, A)$:

$$\chi^2(z, T, A) = \sum_{f=1}^{N_f} \left(\frac{F^f_{\rm obs} - A \times F^f_{\rm tmp}(z, T)\ 10^{-0.4 s_f}}{\sigma^f_{\rm obs}} \right)^2 , \qquad \text{(A.15)}$$

where $F^f_{\rm tmp}(T, z)$ is the flux predicted for an SED template T at redshift z, $F^f_{\rm obs}$ is the observed flux, and $\sigma^f_{\rm obs}$ is the associated error. The index f refers to each specific filter and $N_{\rm f}$ is the number of filters. A is the normalization factor and s_f is the zero-point offset.

The SED templates are generated as the following steps:

- The 20 model SED templates are obtained by the SPS model of Bruzual & Charlot (2003, hereafter BC03) and empirical SEDs determined by the observed galaxies at high redshift. The SED templates consist of 2 elliptical (non-starforming), 6 spiral (star-forming), and 12 starburst SEDs shown in Figure 1 taken from Figure 5 of I09. These SED templates include various types of star formation history which enables to reproduce observed SEDs well. The elliptical and spiral SEDs are based on the observed SEDs of high-redshift galaxies. The starburst SEDs are derived by the BC03 SPS model.
- The [OII], [OIII], Lyα, Hα, and Hβ emissions from ionized gas are added to the SED templates. The fluxes of these emission lines are evaluated with the UV flux of model SED by an empirical relation between UV and emission line.
- The extinction by interstellar dust is applied to the above SED templates. The

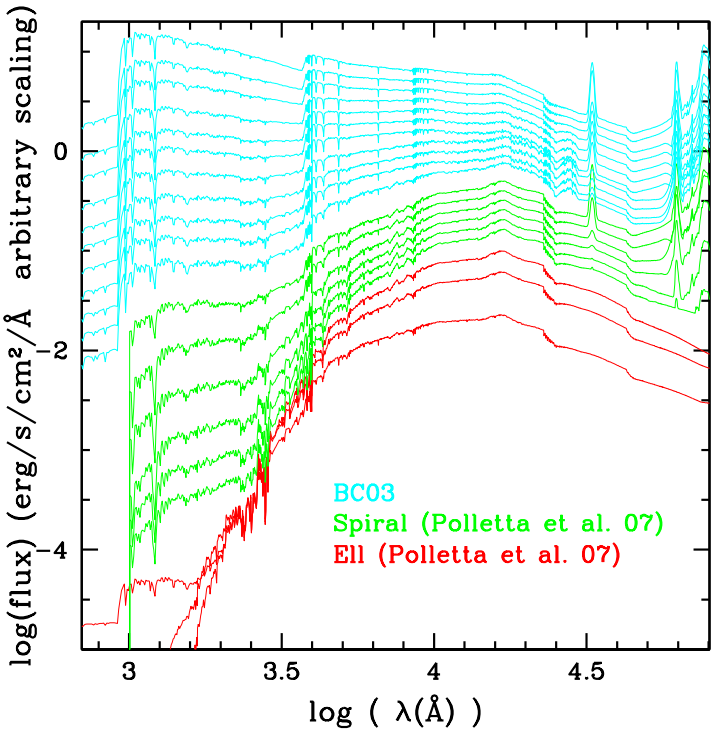

Fig. 1.— The SED templates used in the SED fitting taken from Figure 1 of I09. The SEDs are E0-E2 (red), S0-Sdm (green) and SB0-SB11 (blue) from bottom to top.

dust-extinction law is assumed suitable for the SED templates. For the templates bluer than SB3, Calzetti et al. (2000) extinction law with extinction 2175 Å bump is applied. For the templates redder than SB3 and bluer than Sc, the Prevot et al. extinction law (Prevot et al. 1984) is assumed. For the templates redder than Sb, no dust extinction is assumed.

- The extinction of intergalactic medium is taken into account following Madau et al. (1996). The light from galaxies at high redshift are absorbed due to cosmologically distributed HI gas in intergalactic medium on the line-of-sight from Earth to the galaxy.

2.2. Physical quantities

The physical quantities like stellar mass and SFR are estimated by comparison between the observed SED and theoretical model SEDs. They are determined as minimizing the

Table 1: Parameters used to generate the SED templates with the BC03 package taken from Table 1 of I10

τ (Gyr)	E(B-V)	Z
0.1	0	0.02 ($Z_\odot$)
0.3	0.1	0.008
1	0.2	
2	0.3	
3	0.4	
5	0.5	
10		
15		
30		

following metric function $\chi^2(T, A)$:

$$\chi^2(T, A) = \sum_{f=1}^{N_f} \left(\frac{F^f_{\rm obs} - A \times F^f_{\rm tmp}(z = z_{\rm ph}, T)\ 10^{-0.4 s_f}}{\sigma^f_{\rm obs}} \right)^2 . \tag{A.16}$$

Here, the redshift is fixed to the photometric redshift $z_{\rm ph}$ which have already been evaluated in Section 2.1.

The model SEDs are generated by the BC03 SPS model with the following setup:

- exponentially decaying SFH with the ages of galaxies between 0.1 and 14.5 Gyrs and the decaying time τ between 0.1 and 30 Gyrs
- Chabrier IMF (Chabrier 2003)
- Calzetti dust-extinction law (Calzetti et al. 2000) with $E(B-V)$ between 0 and 0.5
- metallicities with $Z = 0.02$ ($Z_\odot$) and $Z = 0.008$

The parameters to generate SED templates are summarized in Table 1 taken from Table 1 of I10.

2.3. Uncertainty of redshift, stellar mass, and SFR

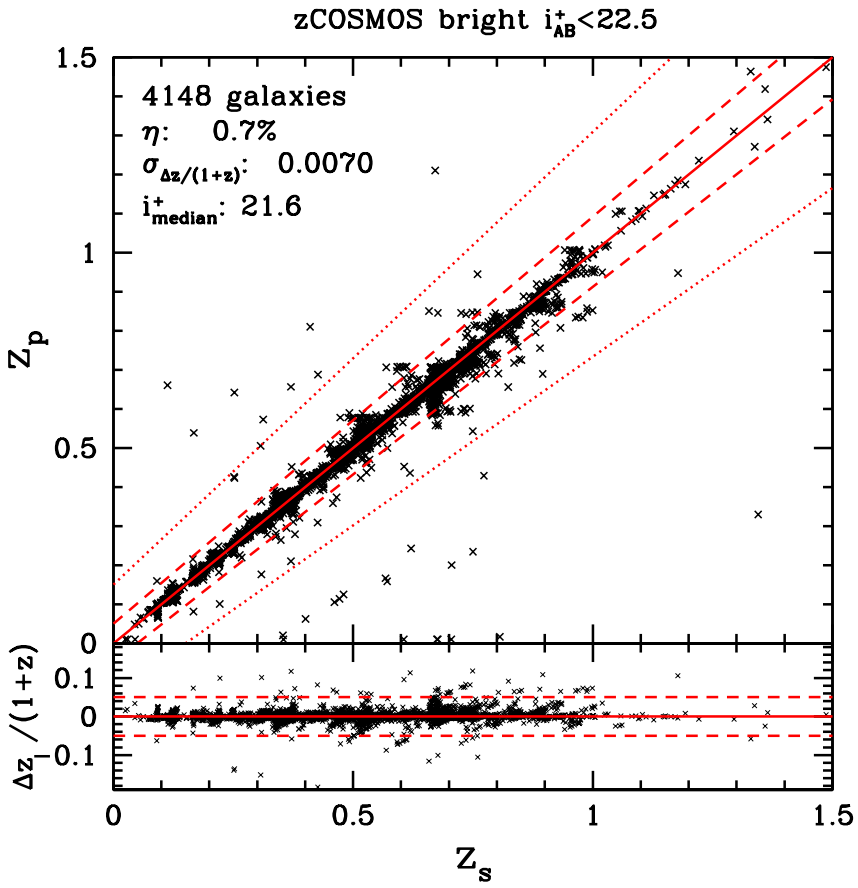

Fig. 2.— Top: Comparison of the photo-z ($z_{\rm p}$) with the spectroscopic redshift ($z_{\rm s}$) for the zCOSMOS-bright spectroscopic sample. The figure is taken from Figure 6 of I09. The solid, dashed, and dotted lines are for $z_{\rm p} = z_{\rm s}$, $z_{\rm p} \pm 0.05(1+z_{\rm s})$, and $z_{\rm p} = z_{\rm s} \pm 0.15(1+z_{\rm s})$, respectively. The number of sample, percentage of catastrophic error η, 1σ dispersion, and the median magnitude of i^+ band are denoted in the figure. Bottom: $\Delta z/(1+z_{\rm s})$ as a function of $z_{\rm s}$.

In Figure 2 taken from Figure 6 of Ilbert et al. (2009), the accuracy of the photo-z is assessed by comparison with the spectroscopic redshift for the zCOSMOS-bright spectroscopic sample (Lilly et al. 2009). The photo-z is quite accurate for the sample thanks to the 30 observed bands. The accuracy is $\sigma_{\Delta z/(1+z)} = 0.007$ at $i^+ < 22.5$ and redshift $z < 1$ which is negligible compared to the redshift interval ($\Delta z = 0.2$) used in this study.

The systematic uncertainty of stellar mass is also quantified by I10. The median difference between stellar mass computed with redshift as photo-z and spectroscopic redshift in (A.16) is smaller than 0.002 dex and the dispersion is smaller than 0.03 dex.

The median difference between stellar mass computed with the Calzetti dust-extinction law (Calzetti et al. 2000) and the Charlot & Fall law (Charlot & Fall 2000) is smaller than 0.27 dex and the dispersion is typically 0.1 dex. The median difference between stellar mass computed with BC03 SPS model and the Charlot & Bruzual 2007 (S. Charlot & A. G. Bruzual 2007, private communication) SPS model is smaller than 0.15 dex with dispersion 0.09 dex. The SFRs calculated by the SED fitting with UV to MIR is proportional with those with 24 μm continuum which is more sophisticated method to estimate SFRs. The systematic uncertainty of stellar mass and SFR are small enough and does not affect the results of Chapter 2.

Bibliography

Abraham, R. G., Tanvir, N. R., Santiago, B. X., et al. 1996, MNRAS, 279, L47

Abraham, R. G., & van den Bergh, S. 2001, Science, 293, 1273

Agertz, O., Teyssier, R., & Moore, B. 2009, MNRAS, 397, L64

Arp, H. 1966, Atlas ofPeculiar Galaxies (Pasadena, CA: California Institute of Technology)

Bekki, K. 2001, ApJ, 546, 189

Benítez-Llambay, A., Navarro, J. F., Abadi, M. G., et al. 2013, ApJ, 763, L41

Bertin, E., & Arnouts, S. 1996, A&AS, 117, 393

Binney, J., & Tremaine, S. 2008, Galactic Dynamics (2nd ed.; Princeton, NJ: Princeton Univ. Press)

Blanton, M. R., Hogg, D. W., Bahcall, N. A., et al. 2003, ApJ, 592, 819

Bournaud, F., Elmegreen, B. G., & Elmegreen, D. M. 2007, ApJ, 670, 237

Bournaud, F., Daddi, E., Elmegreen, B. G., et al. 2008, A&A, 486, 741

Bournaud, F., Elmegreen, B. G., Teyssier, R., Block, D. L., & Puerari, I. 2010, MNRAS, 409, 1088

Bournaud, F., Juneau, S., Le Floc'h, E., et al. 2012, ApJ, 757, 81

Briggs, F. H., Möller, O., Higdon, J. L., Trentham, N., & Ramirez-Ruiz, E. 2001, A&A, 380, 418

Brinchmann, J., Charlot, S., White, S. D. M., et al. 2004, MNRAS, 351, 1151

Bruzual, G., & Charlot, S. 2003, MNRAS, 344, 1000

Buat, V., Boissier, D., Burgarella, D. et al. 2008, A&A, 483, 107

Bunker, A., Spinrad, H., Stern, D., et al. 2000, arXiv:astro-ph/0004348

Cacciato, M., Dekel, A., & Genel, S. 2012, MNRAS, 421, 818

Calzetti, D., Armus, L., Bohlin, R. C., et al. 2000, ApJ, 533, 682

Cameron, E., Carollo, C. M., Oesch, P. A., et al. 2011, ApJ, 743, 146

Carilli, C. L.,& Walter, F. 2013, ARA&A, 51, 105

Carozzi, N., Chamaraux, P., & Duflot-Augarde, R. 1974, A&A, 30, 21

Ceverino, D., Dekel, A., & Bournaud, F. 2010, MNRAS, 404, 2151

Chabrier, G. 2003, PASP, 115, 763

Charlot, S., & Fall, S. M. 2000, ApJ, 539, 718

Coleman, G. D., Wu, C.-C., & Weedman, D. W. 1980, ApJS, 43, 393

Conselice, C. J., Blackburne, J. A., & Papovich, C. 2005, ApJ, 620, 564

Chung, A., vanGorkom, J. H., Kenney, J. D. P., Crowl, H., & Vollmer, B. 2009, AJ, 138, 1741

Cole, G. H. J., Pedlar, A., Holloway, A. J., & Mundell, C. G. 1999, MNRAS, 310, 1033

Cowie, L. L., Hu, E. M., & Songaila, A. 1995, AJ, 110, 1576

Cowie, L. L., Hu, E. M., & Songaila, A. 1995, AJ, 110, 1576

Cresci, G., Hicks, E. K. S., Genzel, R., et al. 2009, ApJ, 697, 115

Daddi, E., Bournaud, F., Walter, F., et al. 2010, ApJ, 713, 686

Dalcanton, J. J., & Shectman, S. A. 1996, ApJ, 465, L9

Damen, M., Labbé, I., Franx, M., et al. 2009, ApJ, 690, 937

de Grijs, R. & Robertson, R. I. 2006, A&A, 460, 493

Dekel, A., Sari, R., & Ceverino, D. 2009, ApJ, 703, 785

Dekel, A., Birnboim, Y., Engel, G., et al. 2009, Nature, 457, 451

Delgado-Serrano, R., Hammer, F., Yang, Y. B., et al. 2010, A&A, 509, A78

Domainko, W., Mair, M., Kapferer, W., et al. 2006, A&A, 452, 795

Elbaz, D., Daddi, E., Le Borgne, D., et al. 2007, A&A, 468, 33

Elmegreen, D. M., & Elmegreen, B. G. 2006, ApJ, 651, 676

Elmegreen, B. G., & Elmegreen, D. M. 2010, ApJ, 722, 1895

Elmegreen, D. M., Elmegreen, B. G., & Hirst, A. C. 2004a, ApJ, 604, L21

Elmegreen, D. M., Elmegreen, B. G., & Sheets, C. M. 2004b, ApJ, 603, 74

Elmegreen, B. G., & Elmegreen, D. M. 2006a, ApJ, 650, 644

Elmegreen, D. M., Elmegreen, B. G., Rubin, D. S. & Schaffer, M. A. 2005, ApJ, 631, 85 (E05)

Elmegreen, D. M., Elmegreen, B. G., Ravindranath, S., & Coe, D. A. 2007, ApJ, 658, 763

Elmegreen, D. M., Elmegreen, B. G., Ferguson, T., & Mullan, B. 2007, ApJ, 663, 734

Elmegreen, D. M., Elmegreen, B. G., Marcus, M. T., et al. 2009, ApJ, 701, 306

Elmegreen, B. G., Elmegreen, D. M., Fernandez, M. X., & Lemonias, J. J. 2009, ApJ,

692, 12 (E09a)

Elmegreen, D. M., Elmegreen, B. G., Marcus, M. T., et al. 2009, ApJ, 701, 306

Elmegreen, D. M., Elmegreen, B. G., Sánchez Almeida, J., et al. 2012, ApJ, 750, 95

Elmegreen, B. G., & Elmegreen, D. M. 2010, ApJ, 722, 1895

Elmegreen, B. G., Bournaud, F., & Elmegreen, D. M. 2008, ApJ, 688, 67

Elmegreen, D. M., & Elmegreen, B. G. 2006b, ApJ, 651, 676 (EE06)

Elmegreen, D. M., Elmegreen, B. G., & Hirst, A. C. 2004a, ApJ, 604, L21 (EEH04)

Elmegreen, D. M., Elmegreen, B. G., & Sheets, C. M. 2004b, ApJ, 603, 74 (EES04)

Elmegreen, D. M., Elmegreen, B. G., Rubin, D. S., & Schaffer, M. A. 2005, ApJ, 631, 85

Elmegreen, D. M., Elmegreen, B. G., Ravindranath, S., & Coe, D. A. 2007, ApJ, 658, 763

Elmegreen, D. M., Elmegreen, B. G., Marcus, M. T., et al. 2009, ApJ, 701, 306 (E09b)

Erb, D. K., Steidel, C. C., Shapley, A. E., Pettini, M., & Adelberger, K. L. 2004, ApJ, 612, 122

Elvis, M., Civano, F., Vignali, C., et al. 2009, ApJS, 184, 158

Escala, A., & Larson, R. B. 2008, ApJ, 685, L31

Escala, A. 2011, ApJ, 735, 56

Förster Schreiber, N. M., Shapley, A. E., Genzel, R., et al. 2011, ApJ, 739, 45

Fukugita, M., Hogan, C. J. & Peebles, P. J. E. 1998, ApJ, 503, 518

Fukugita, M., Nakamura, O., Okamura, S., et al. 2007, AJ, 134, 579

Fumagalli, M., Gavazzi, G., Scaramella, R., & Franzetti, P. 2011, A&A, 528, A46

Förster Schreiber, N. M., Genzel, R., Lehnert, M. D., et al. 2006, ApJ, 645, 1062

Förster Schreiber, N. M., Genzel, R., Bouché, N., et al. 2009, ApJ, 706, 1364

Förster Schreiber, N. M., Shapley, A. E., Genzel, R., et al. 2011, ApJ, 739, 45

Genzel, R., Burkert, A., Bouché, N., et al. 2008, ApJ, 687, 59

Genzel, R., Newman, S., Jones, T., et al. 2011, ApJ, 733, 101

Goad, J. W., & Roberts, M. S. 1981, ApJ, 250, 79

Genzel, R., Burkert, A., Bouché, N., et al. 2008, ApJ, 687, 59

Genzel, R., Tacconi, L. J., Combes, F., et al. 2012, ApJ, 746, 69

Grogin, N. A., Kocevski, D. D., Faber, S. M., et al. 2011, ApJS, 197, 35

Gunn, J. E., & Gott, J. R., III 1972, ApJ, 176, 1

Guo, Q., & White, S. D. M. 2008, MNRAS, 384, 2

Guo, Y., Giavalisco, M., Ferguson, H. C., Cassata, P., & Koekemoer, A. M. 2012, ApJ,

757, 120

Guo, Y., Giavalisco, M., Ferguson, H. C., Cassata, P., & Koekemoer, A. M. 2012, ApJ, 757, 120

Hasinger, G., Cappelluti, N., Brunner, H., et al. 2007, ApJS, 172, 29

Hubble, E. P. 1926, ApJ, 64, 321

Hubble, E. P. 1936, Realm of the Nebulae, by E. P. Hubble. New Haven: Yale University Press, 1936. ISBN 9780300025002

Ibata, R., Irwin, M., Lewis, G., Ferguson, A. M. N., & Tanvir, N. 2001, Nature, 412, 49

Ibata, R. A., Lewis, G. F., Irwin, M. J., & Cambrésy, L. 2002, MNRAS, 332, 921

Ilbert, O., Capak, P., Salvato, M., et al. 2009, ApJ, 690, 1236

Ilbert, O., Salvato, M., Le Floc'h, E., et al. 2010, ApJ, 709, 644

Ilbert, O., McCracken, H. J., Le Fèvre, O., et al. 2013, A&A, 556, A55

Immeli, A., Samland, M., Westera, P., & Gerhard, O. 2004, ApJ, 611, 20

Kajisawa, M., & Yamada, T. 2001, PASJ, 53, 833

Kajisawa, M., Ichikawa, T., Yamada, T., et al. 2010, ApJ, 723, 129

Keel, W. C., & White, R. E. III. 2001, AJ, 122, 1369

Keel, W. C., Manning, A. M., Holwerda, B. W., et al. 2013, PASP, 125, 2

Kereš, D., Katz, N., Weinberg, D. H., & Davé, R. 2005, MNRAS, 363, 2

Koekemoer, A. M., Aussel, H., Calzetti, D., et al. 2007, ApJS, 172, 196

Koekemoer, A. M., Faber, S. M., Ferguson, H. C., et al. 2011, ApJS, 197, 36

Law, D. R., Steidel, C. C., Erb, D. K., et al. 2007, ApJ, 656, 1

Lilly, S. J., Le Brun, V., Maier, C., et al. 2009, ApJS, 184, 218

Livermore, R. C., Jones, T., Richard, J., et al. 2012, MNRAS, 427, 688

Lotz, J. M., Primack, J., & Madau, P. 2004, AJ, 128, 163

Lotz, J. M., Davis, M., Faber, S. M., et al. 2008, ApJ, 672, 177

Madau, P., Ferguson, H. C., Dickinson, M. E., et al. 1996, MNRAS, 283, 1388

Maseda, M. V., van der Wel, A., da Cunha, E., et al. 2013, arXiv:1310.6358

Merritt, D., & Sellwood, J. A. 1994, ApJ, 425, 551

Mandelker, N., Dekel, A., Ceverino, D., et al. 2013, arXiv:1311.0013

Markarian, B. E. 1969, Astrofizika, 5, 581

Miyauchi-Isobe, N., Maehara, H., & Nakajima, K. 2010, Publ. Natl. Astron. Obs. Japan, 13, 9

Morrissey, P., Schiminovich, D., & Barlow, T. A. 2005, ApJ, 619, L7

Nakahiro, Y., Taniguchi, Y., Inoue, A. K., et al. 2013, ApJ, 766, 122

Noeske, K. G., Weiner, B. J., Faber, S. M., et al. 2007, ApJ, 660, L43

Noguchi, M. 1998, Nature, 392, 253

Overzier, R. A., Heckman, T. M., Tremonti, C., et al. 2009, ApJ, 706, 203

Overzier, R. A., Heckman, T. M., Schiminovich, D., et al. 2010, ApJ, 710, 979

Pérez-González, P. G., Rieke, G. H., Villar, V., et al. 2008, ApJ, 675, 234

Petty, S. M., de Mello, D. F., Gallagher, J. S., III, et al. 2009, AJ, 138, 362

Prevot, M. L., Lequeux, J., Prevot, L., Maurice, E., & Rocca-Volmerange, B. 1984, A&A, 132, 389

Raha, N., Sellwood, J. A., James, R. A., & Kahn, F. D. 1991, Nature, 352, 411

Renzini, A. 2009, MNRAS, 398, L58

Revaz, Y., & Pfenniger, D. 2004, A&A, 425, 67

Rodighiero, G., Daddi, E., Baronchelli, I., et al. 2011, ApJ, 739, L40

Salmi, F., Daddi, E., Elbaz, D., et al. 2012, ApJ, 754, L14

Sanders, D. B., Soifer, B. T., Elias, J. H., et al. 1988, ApJ, 325, 74

Santini, P., Fontana, A., Grazian, A., et al. 2009, A&A, 504, 751

Scoville, N., Aussel, H., Brusa, M., et al. 2007, ApJS, 172, 1

Smith, R., Duc, P. A., Candlish, G. N., et al. 2013, MNRAS, 436, 839

Somerville, R. S., Primack, J. R., & Faber, S. M. 2001, MNRAS, 320, 504

Steidel, C. C., Giavalisco, M., Dickinson, M., & Adelberger, K. L. 1996, AJ, 112, 352

Straughn, A. N., Cohen, S. H., Ryan, R. E., et al. 2006, ApJ, 639, 724

Swinbank, A. M., Smail, I., Sobral, D., et al. 2012, ApJ, 760, 130

Tacconi, L. J., Genzel, R., Neri, R., et al. 2010, Nature, 463, 781

Tacconi, L. J., Neri, R., Genzel, R., et al. 2013, ApJ, 768, 74

Tadaki, K.-i., Kodama, T., Tanaka, I., et al. 2013, arXiv:1311.4260

Taniguchi, Y., & Shioya, Y. 2001, ApJ, 547, 146 (TY01)

Toomre, A. 1964, ApJ, 139, 1217

van denBergh, S., Abraham, R. G., Ellis, R. S., et al. 1996, AJ, 112, 359

van den Bergh, S., Abraham, R. G., Ellis, R. S., et al. 1996, AJ, 112, 359

van Dokkum, P. G., Franx, M., Kriek, M., et al. 2008, ApJ, 677, L5

van Dokkum, P. G., Kriek, M., & Franx, M. 2009, Nature, 460, 717

Wakamatsu, K., Sakka, K., Nishida, M., & Jugaku, J. 1979, PASJ, 31, 635

Weiner, B. J., Willmer, C. N. A., Faber, S. M., et al. 2006, ApJ, 653, 1027

Williams, R. E., Blacker, B., Dickinson, M., et al. 1996, AJ, 112, 1335

Wolf, C., Meisenheimer, K., Rix, H.-W., et al. 2003, A&A, 401, 73

Wright, S. A., Larkin, J. E., Barczys, M., et al. 2007, ApJ, 658, 78

Wuyts, S., Förster Schreiber, N. M., Lutz, D., et al. 2011, ApJ, 738, 106

Wuyts, S., Förster Schreiber, N. M., Genzel, R., et al. 2012, ApJ, 753, 114

Wuyts, S., Förster Schreiber, N. M., Genzel, R., et al. 2012, ApJ, 753, 114

Yagi, M., Yoshida, M., Komiyama, Y., et al. 2010, AJ, 140, 1814

Yagi, M., Gu, L., Fujita, Y., et al. 2013, arXiv:1308.6053

Yamagami, T.,& Fujita, Y. 2011, PASJ, 63, 1165

Yoshida, M., Yagi, M., Komiyama, Y., et al. 2008, ApJ, 688, 918

Yoshida, M., Yagi, M., Komiyama, Y., et al. 2012, ApJ, 749, 43